



Master Thesis

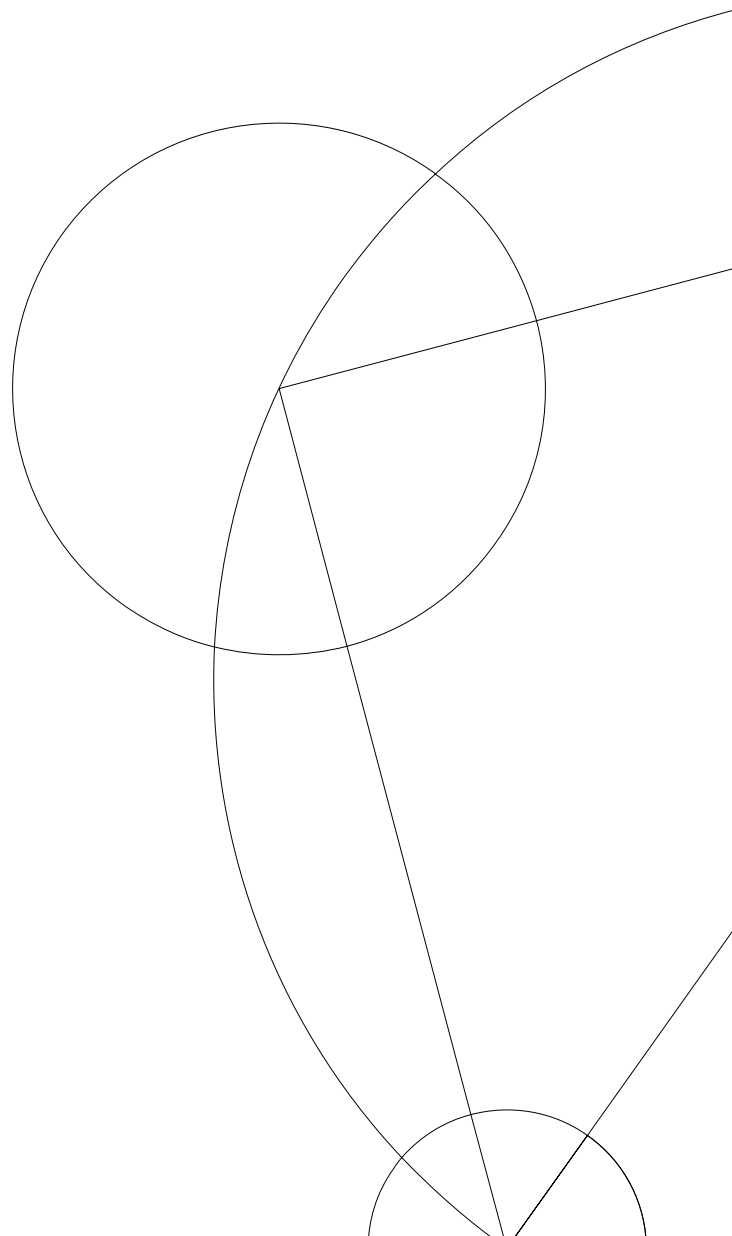
Mathias Kure

Simulation and prototype tests of the MultiFLEXX

A multiplexing back-end for the
FLEXX Triple-Axis Spectrometer

Supervisors: Kim Lefmann and Rasmus Toft-Petersen

Monday 8th December, 2014



Contents

Acknowledgements	iv
Abstract	v
Resumé	vi
1 Introduction	1
2 Neutron basics	2
2.1 The neutron as a probe	2
2.2 Neutron properties	2
2.3 The neutron cross section	4
2.4 Basic elastic scattering	5
2.4.1 Coherent and incoherent scattering	7
2.4.2 Absorption	8
2.4.3 The crystal lattice	9
2.4.4 Bragg's Law	10
2.5 Basic inelastic scattering	13
2.6 The scattering triangle	15
3 Inelastic neutron instruments	17
3.1 Neutron sources	17
3.2 Moderators and guides	18
3.3 The Triple Axis Spectrometer	20
3.3.1 A typical TAS experiment	21
3.4 The FLEXX spectrometer	22
3.4.1 Monochromator resolution	22
3.4.2 Mosaicity	22
3.5 The Time Of Flight Spectrometer	23
3.6 Advantages and drawbacks	26
4 The MultiFLEXX design - combining advantages	27
4.1 The MultiFLEXX design	28
4.1.1 Analyser channels	28
4.1.2 Beryllium filter	30
4.2 Experiments with the MultiFLEXX	31
5 Analyser geometries in neutron scattering	32
5.1 The Rowland geometry	33
5.2 The situation for FLEXX and MultiFLEXX	35
5.2.1 Rowland in the FLEXX monochromator	35
5.2.2 Rowland in the MultiFLEXX	35
5.3 The curved analyser	37
6 Resolution of neutron instruments	39
6.1 The resolution function	39
6.1.1 Focusing measurements	40
6.2 Resolution matching	40

7	Neutron simulation	43
7.1	The Monte Carlo method	43
7.2	The McStas system	43
7.3	Ray-tracing and Monte Carlo in McStas	44
7.4	Building the MultiFLEXX back-end	46
8	Simulation results	48
8.1	Simulating analyser curvature	48
8.1.1	Elastic resolution simulations	50
8.1.2	Inelastic resolution simulations	53
8.1.3	Designing new analysers	55
8.2	Simulating sample size	57
8.3	Lessons from simulations	59
9	Prototype setup	61
9.1	Experimental setup	61
9.1.1	Aligning analyser holders	62
9.1.2	Detector setup	63
9.1.3	Ra-Be source experiments	65
9.1.4	Setting up for PANDA	65
10	Prototype experiments	68
10.1	Threshold tests	68
10.2	Elastic resolution and intensity improvements	69
10.3	Phonon experiments and inelastic widths	74
10.3.1	Bragg peak resolution	75
10.3.2	Incoming energy scan	75
10.3.3	Q scan	79
10.3.4	Phonon mapping	82
10.4	Background measurements	85
10.4.1	Crosstalk and shielding	85
11	Conclusion	89
11.1	Simulations	89
11.2	Experiments	89
11.3	Outlook	90
A	Elastic scans over curvature	96
B	Elastic comparisons between curved and AR	98
C	Inelastic scans over curvature	100
D	Inelastic comparisons between curved and AR	103

Acknowledgements

I would like to thank the people who have made writing this thesis a good experience, and a very instructive one too! First of all, I would like to thank Rasmus Toft-Petersen for all his support in Berlin, where the groundwork of this thesis was made. Having his office just down the aisle was important for me to get the hang of neutron scattering with only a few months of preparation.

I would also like to thank Kim Lefmann for giving me the opportunity of writing this thesis, and for helping me getting started with neutron scattering. The atmosphere in his group is great, and his attitude towards science and the members of the group is certainly an important part of that.

Jonas Okkels Birk also deserve some recognition for a lot of fruitful discussions, and Rasmus Laurberg Hansen for proofreading. Furthermore, I would like to thank the rest of the users of office D311 for always being up for a chat or giving some advice.

Also, I would like to thank the lunch group from HZB for making a poor canteen and boring German rye bread a highlight of the day, and inviting me to all sorts of events. I am missing our discussions, though I never gathered a lot of new Physics knowledge from it!

Finally, I would like to thank my girlfriend, family, and friends for their support!

Abstract

The technique of neutron scattering is highly intensity limited, and much work has gone towards optimising the two competing and complementary techniques, the Triple Axis Spectrometer (TAS) and the Time Of Flight (TOF) spectrometer. Each technique has its advantages and drawbacks, but some types of experiments, especially parametric mapping, are not favourable for either of them.

In this thesis, we describe a multiplexing back-end for the FLEXX TAS that is currently under construction at HZB, to be known as the MultiFLEXX. This design aims to combine the advantages from the TAS and the TOF by measuring five different final energies, 2.5 meV, 3.0 meV, 3.5 meV, 4.0 meV, and 4.5 meV at 31 different angles simultaneously. This is done by vertically scattering the neutrons, such that the horizontal size of the analyser and detector can be minimised, allowing for a close spacing of the 31 angles. To measure several energies simultaneously, we use PG analyser crystals that are practically transparent to neutrons when they are not satisfying the Bragg condition, such that they can be placed one after the other.

We employed McStas simulations to determine the performance of the MultiFLEXX, and found that a design error in the analyser geometry was resulting in the analyser crystals having regions of overlap, effectively reducing the analyser area. It was found that the focusing Rowland geometry could not be used for the analysers due to the proportions of the MultiFLEXX. Instead, a simpler curved geometry was introduced.

The new analyser geometry was optimised for each of the five energies that the MultiFLEXX will detect, both for elastically incoherently scattered neutrons by scanning the incoming energy using the monochromator, and for an inelastic situation where a dispersionless virtual sample removed energy from the neutrons coming at a constant $E_i = 5.0$ meV and scattered them incoherently, to bring their energies within what we can detect using our analysers. McStas simulations showed that the optimal curvature found would give an improvement in peak intensity of between 7% and 15% for the elastic case, and between 8% and 16% for the inelastic case. The improvements in intensity came without significantly worsening the resolution.

As a result of the simulations, it was decided to acquire new analyser holders to take advantage of the predicted increase in intensity.

Using the PANDA TAS front-end, we performed prototype tests on the MultiFLEXX. Two q -channels, one using each type of analyser, were set up for the tests. With an incoherently scattering V sample, we measured the elastic peaks in the same way as for the simulations. Comparing the two geometries, we found an improvement for the three analyser energies that we deemed to be functioning correctly of between 9% and 20%. The resolution from the experiments matched the simulated resolution well for the two lowest energies measured, but showed a significant broadening, between 25% and 56%, for the highest energies measured.

We also attempted to measure the inelastic energy and \mathbf{q} widths, using a phonon in a Pb sample at room temperature. We found the experimental energy widths to be 200% to 350% wider than the simulated ones, showing that there are effects that we cannot model in our simulations with our dispersionless virtual sample.

Resumé

Teknikken neutronspreddning er meget begrænset af intensiteten fra kilden, og meget arbejde er lagt i at udvikle de to konkurrerende og komplementære metoder kendt som Triple Axis Spectrometry (TAS) og Time Of Flight (TOF) spektrometri. Hver metode har sine fordele og ulemper, men der findes eksperimenter, såsom parametriske kortlægning, der ikke kan udføres effektivt af nogen af de to metoder.

I denne opgave beskriver vi en back-end med multi-analysatorer til FLEXX TAS, der i øjeblikket bygges på HZB, og vil gå under navnet MultiFLEXX. Med denne back-end sigtes efter at kombinere fordelene fra TAS og TOF ved at måle ved fem forskellige energier, 2.5 meV, 3.0 meV, 3.5 meV, 4.0 meV og 4.5 meV ved 31 vinkler samtidigt. For at måle flere energier samtidig udnyttedes det, at PG-krystaller er praktisk talt gennemsigtige for neutroner, når de ikke tilfredsstiller Braggs lov, og de kan derfor placeres efter hinanden.

Vi brugte McStas-simuleringer til at bestemme ydeevnen af MultiFLEXX og fandt en fejl i designet af analysator-geometrien, der betød at analysator-krystaller skyggede for hinanden. Dette reducerede det effektive analysator-areal. Ydermere fandt vi, at den fokuserende Rowland-geometri ikke kunne bruges til vores analysatorer på grund af MultiFLEXX proportioner. I stedet introducerede vi en simplere, kurvet geometri.

Vi optimerede den nye analysator-geometri for hver af de fem energier som MultiFLEXX vil detektere. Den elastiske spredning blev simuleret ved at ændre den indkommende energi på en prøve ved hjælp af en monochromator. Den inelastiske spredning blev simuleret ved hjælp af en dispersionsløs virtuel prøve, der fjernede energi fra indkommende neutroner ved $E_i = 5$ meV og spredte dem inkohærent, så deres energi kom inden for det vindue, vi kan detektere med vores analysatorer. McStas-simulationerne viste, at den optimale kurvatur, vi fandt, ville give en forbedring i intensitets-maksimum på mellem 7 % og 15 % for elastisk spredning, og 8 % and 16 % for inelastisk spredning. Forbedringerne i intensitet havde ingen betydelig indflydelse på instrumentets opløsning.

På baggrund af simuleringernes resultat blev det besluttet at anskaffe nye analysator-holdere for at opnå den forudsagte forøgelse af intensitet.

Ved hjælp af PANDA front-end'en foretog vi prototypemålinger med MultiFLEXX. To q -kanaler, en med hver type analysator, blev forberedt til testen. Med en inkohærent spredende V-prøve målte vi elastisk spredning ved at ændre monochromator-energien. Vi vurederede, at data fra tre ud af de fem energier gav mulighed for at sammenligne de to geometrier. For de tre energier fandt vi forbedringer i intensitet på mellem 9 % og 20 %. Opløsningen fra eksperimentet lå tæt på den forudsagte værdi for de to lavest målte energier, mens de højere energier havde en signifikant forbredding på mellem 25 % og 56 %.

Vi forsøgte også at måle den inelastiske energi- og q -bredde ved hjælp af en fonon i Pb ved stuetemperatur. De eksperimentelle energi-bredder fandt vi til at være 200 % til 350 % bredere end de simulerede bredder, hvilket viser at der effekter som vores dispersionsløse virtuelle prøve ikke kan modellere.

1 Introduction

The technique of neutron scattering is highly important in solid state physics, due to the special properties of the neutron, such as the fact that a neutron with the wavelength of the inter-atomic spacing has an energy range similar to that of elementary excitations in solid systems.

However, neutron scattering has long been limited by the amount of neutrons that the sources providing them can output, and the current record holder for continuous neutron output is the high-flux reactor at Institut Laue-Langevin (ILL) which began operation in 1971[1]. The reactor here sits at the upper envelope of neutron production, and the newer neutron production technique of spallation will only surpass the ILL in amount of neutrons produced when the European Spallation Source (ESS) comes online in 2019.

Since increasing neutron output is not a viable option, emphasis has been on improving the efficiency of the neutron scattering instruments used, thus getting more out of each neutron. There are many ways in which the classic Triple Axis Spectrometer (TAS) can be improved, including transporting a greater amount of neutrons from the moderators to the instrument itself using better guides, focusing the neutrons onto a sample to increase the number of interactions between the neutron and the sample, and focusing the neutrons scattered from the sample onto the detector.

Yet another method of using more of the available neutrons is to increase the amount of points where we measure scattered neutrons. This can be done by using the Time Of Flight (TOF) technique which, for other reasons, suffers from a low amount of neutrons delivered unto the sample.

Instead of using TOF, instruments can be made that are multiplexing. The concept has been known for some 25 years and is used for a select few instruments, but the concept has gained a large following as of lately, spurred by the ambitious Continuous Angle Multi Energy Analyser (CAMEA) project proposed for the ESS. This has led to several neutron facilities investigating similar concepts.

One such concept is the MultiFLEXX presented in section 4, a new back-end for the FLEXX TAS situated at Helmholtz-Zentrum Berlin. Measuring at 31 different angles rather than one single angle, and performing simultaneous measurements at five different neutron energies, it will enable neutron experiments to be performed in a more effective way for certain types of measurements.

Before neutron instruments are constructed, their performance are tested in simulations using Monte Carlo ray tracing methods, such as those the programme McStas provides. Simulations allows for optimisation of various parts of the instrument, and due to the sparsity of neutrons coming from the sources, even small improvements are welcome.

In this thesis I present my work on the MultiFLEXX design and prototype, where I have been working on McStas simulations in order to optimise the design and participated in the first prototype tests, where it was tested whether the optimisation was also reproducible in an experimental situation.

2 Neutron basics

In this section, we will first list the properties of neutrons that make them highly useful as probes in solid state physics, before we present the most important equations governing scattering physics.

2.1 The neutron as a probe

There is a saying amongst scientists who are working in scattering physics: “If an experiment can be done with X-rays, use X-rays”. But some experiments are just not fit for X-ray experiments and the properties of neutrons complement many of the shortcomings that X-rays have[2], as described below:

1. Since the neutron has a magnetic moment, it will scatter from **magnetic field gradients and structures**, providing an important tool for deriving the periodicity and magnitude of magnetic order.
2. The neutrons whose **wavelength** is of the same size as inter-atomic distances in solids are also, due to the high mass of the neutron, those with an **energy** that matches the elementary excitations in solids. This means that experiments can be performed where the structure and dynamics are probed simultaneously, and it is possible to measure dispersion relations in solids.
3. The way that neutrons interact with matter gives us the possibility to **distinguish isotopes** from each other. This means that, by exchanging hydrogen (^1H) for deuterium (^2D), one can obtain a high contrast between for example a sample and a solution in which it is kept. It is also the case that the interaction strength can be **large for smaller atoms**, meaning that atoms that would otherwise be invisible to X-rays (where the interaction strength goes as Z^4) can give a very large signal when investigated with neutrons.
4. The neutron has very weak interactions with the (most) materials, which means that the **bulk of a solid** can be probed, instead of just the surface. Furthermore, the weak interactions means that **second order effects are negligible** which makes comparisons between theoretical models and experimental data viable.
5. There is also the possibility that a normally dense material can be almost invisible to neutrons. This gives the possibility to create **sample environments**, such as pressure cells, magnets, and cryostats from these materials, while enabling measurement on a sample contained within.

In short, if any of the above properties are of interest to us for a given material, we will have to resort to neutron scattering techniques.

2.2 Neutron properties

The neutron itself is a sub-atomic particle that consists of one *up*-quark and two *down*-quarks, with a mass of

$$m_n = 1.675 \times 10^{-27} \text{ kg} \quad (1)$$

and a spin of $s = 1/2$. It was theoretized in 1920 by Ernest Rutherford due to the disparity between the mass of the proton itself and the mass of elements known to consist of specific number of protons. In 1932, it was experimentally shown to exist by James Chadwick, giving him the Nobel Prize in 1935[3]. As the name implies, the neutron has no charge which means that it is not repelled by the positive protons, but, through the strong (but short-range) nuclear force, acts to keep the protons from repelling each other inside the nucleus of an atom. Outside of the nucleus, the free neutron will β -decay with a mean lifetime of $\tau = 887.7(22)$ s[4], with decay products a proton, an electron and an anti-neutrino. The neutrons substructure of quarks described above give rise to a magnetic moment, which is of the size

$$\mu = \gamma\mu_N \quad (2)$$

with $\mu_N = e\hbar/(2m_n) = 5.051 \times 10^{-27}$ J/T the nuclear magneton and $\gamma = -1.913$ the neutron gyromagnetic ratio.

Since the neutron is a quantum mechanical particle, it can be described both as a particle and as a wave. This particle-wave-duality is something that confounds physicists and philosophers alike, so we will not go further into details about it; instead, we simply state that under certain conditions it is possible to describe the neutron as a wave, in which case it will have a wavelength λ , as de Broglie suggested, of

$$\lambda = \frac{2\pi\hbar}{m_nv} \quad (3)$$

with v the speed of the neutron.

This wave-nature of the neutron means that, in cases where the neutrons scatter, it can be described by a plane wave when the neutron wavelength is much smaller than the scatterer.

$$\psi_i(\mathbf{r}) = \frac{1}{\sqrt{Y}} e^{i\mathbf{k}_i \cdot \mathbf{r}} \quad (4)$$

where \mathbf{k} is the *wave vector* and \mathbf{r} the point at which we measure the wave. A normalisation factor Y comes from box normalisation, a quantum mechanical trick where we choose an arbitrary box in which the wave resides. The size of the box is completely arbitrary, as it will cancel out later and therefore it is dropped from the calculations from here on. The wave vector in (4) is defined as

$$\mathbf{k} = \frac{m_n\mathbf{v}}{\hbar} \quad k = \frac{2\pi}{\lambda} \quad (5)$$

with \mathbf{k} obviously pointing in the same direction as \mathbf{v} , the speed of the neutron.

We have already come across the velocity, the wavelength, and the wave vector of the neutron. These are linked to the energy of the free neutron as

$$E = \frac{\hbar^2 |\mathbf{k}|^2}{2m_n} = \frac{h^2}{2m_n\lambda^2} = \frac{m_nv^2}{2} = k_B T \quad (6)$$

and we find that all neutrons can also be described as having an equivalent temperature T . We are left with a whole lot of different ways of expressing the

neutron characteristics, but most commonly used are energy in meV, and wavelengths and wavenumbers in \AA and \AA^{-1} , respectively. \AA is short for Angstrom, a non-SI unit corresponding to 10^{-10} m that is used in spectroscopy on grounds of tradition. Informally, ranges of neutron energies are also referred to as being "cold", "thermal", or "hot", each representing a certain range of neutron energies as created by different moderators (which will be described closer in section 3.2). Table 1 summarizes the neutron energies most often used for experiments and the corresponding wavelengths and temperature ranges[2].

Energy interval	Wavelength interval	Temperature range
less than 0.05 meV	$> 40 \text{\AA}$	Ultra cold ≈ 4 K
0.05 meV - 14 meV	$2.4 \text{\AA} - 40 \text{\AA}$	Cold ≈ 25 K
14 meV - 200 meV	$0.6 \text{\AA} - 2.4 \text{\AA}$	Thermal ≈ 300 K
200 meV - 1 eV	$0.3 \text{\AA} - 0.6 \text{\AA}$	Hot ≈ 2000 K
1 eV - 10 keV	$< 0.3 \text{\AA}$	Epithermal (Background)

Table 1: Neutron energies and their corresponding wavelengths and temperature ranges.

2.3 The neutron cross section

When performing neutron experiments on a material, we shine a beam of neutrons onto it and monitor where these neutrons are scattered to. We express this actual quantity measured as the *cross section*. The cross section represents the number of neutrons scattered per second, normalised by the incoming *flux* Ψ_i of neutrons. The flux is defined as the number of neutrons impinging perpendicular on a surface divided by the area of that surface. In terms of the plane wave in equation (4), it can be written as

$$\Psi_i = |\psi_i|^2 v_i = \frac{1}{Y} \frac{\hbar k_i}{m_n} \quad (7)$$

where the i denotes incoming neutrons, and from this we define the cross section as

$$\sigma_{tot} = \frac{(\text{Neutrons scattered per second})}{\Psi_i} \quad (8)$$

Since the dimensions of flux are $[\text{n cm}^{-2} \text{s}^{-1}]$, we have that the cross section have dimension $[\text{m}^2]$ as the name itself hints at. Traditionally, cross sections are measured in barns, where $1 \text{ barn} = 10^{-28} \text{ m}^2$.

In an experiment, the distribution of scattered neutrons is equally important to the amount of neutrons scattered. Thus, we define the *differential cross section*

$$\frac{d\sigma}{d\Omega} = \frac{1}{\Psi} \frac{(\text{Neutrons scattered per second into solid angle } d\Omega)}{d\Omega} \quad (9)$$

where the amount of neutrons scattered into a specific solid angle $d\Omega$ is measured. This cross section is used in *elastic neutron scattering* where the neutrons

lose no energy in their interaction with the sample, but are scattered into a direction different from their incoming path.

Another cross section is used in *inelastic neutron scattering* where the energies of the outgoing neutrons are different from that of the incoming neutrons. This gives another property of the scattered neutrons, their final energies E_f . This is taken into account by the *partial differential cross section*

$$\frac{d\sigma^2}{d\Omega dE} = \frac{1}{\Psi} \left(\frac{\text{Neutrons scattered per second into solid angle } d\Omega}{\text{with energies } [E_f + dE_f]} \right) \frac{d\Omega dE_f}{d\Omega dE_f} \quad (10)$$

a measure of the amount of neutrons scattered into a specific solid angle with an energy in the range E_f and $E_f + dE_f$.

The energy difference between the incoming and the outgoing neutrons are caused by the neutron adding energy to or removing energy from the sample. This changes the length of k , and with the formulae in equation (6) allows us to calculate this energy difference as

$$E_i - E_f = \Delta E = \hbar\omega = \frac{\hbar^2(k_i - k_f)^2}{2m_n} \quad (11)$$

Some neutron instruments can resolve these energy differences (the methods used are presented in detail in section 3); this provides a lot of extra information that would otherwise be lost if only the directions (i.e. the differential cross section) of the scattered neutrons were recorded.

It is of course possible to link equations (8), (9), and (10) through integrations. First, we can integrate the partial differential cross section (10) over all energies, yielding

$$\int_0^\infty \left(\frac{d\sigma^2}{d\Omega dE_f} \right) dE = \frac{d\sigma}{d\Omega} \quad (12)$$

which in turn can be integrated over all solid angles (i.e. a unit sphere) to give

$$\int_{\text{all directions}} \left(\frac{d\sigma}{d\Omega} \right) d\Omega = \sigma_{tot}, \quad (13)$$

the total cross section.

2.4 Basic elastic scattering

We will here show some basic results from a quantum mechanical treatment of a neutron scattering off of nuclei that are fixed in space. Some results are taken from [2], which also features a quick semi-classical treatment that may give a better physical intuition.

An incoming neutron has the quantum mechanical state $|\psi_i\rangle$, the plane wave presented in (4). After the interaction with the sample, the neutron can now be described as a superposition of plane waves of the same form as the incoming wave

$$|\psi_f\rangle = \frac{1}{\sqrt{Y}} \exp(i\mathbf{k}_f \cdot \mathbf{r}), \quad (14)$$

the only change occurring is to the direction of the wave vector \mathbf{k} . The equation that governs scattering is known as *Fermi's Golden Rule*

$$W_{i \rightarrow f} = \frac{2\pi}{\hbar} \frac{dn}{dE_f} \left| \langle \psi_i | \hat{V} | \psi_f \rangle \right|^2 \quad (15)$$

that describes the rate of change (number of transitions per second) between the incoming neutrons and a particular state $|\psi_f\rangle$ within a continuum of outgoing neutrons. The term dn/dE_f is the density of states for neutrons of the energy E_f . The operator \hat{V}_j in the case of neutron scattering is modeled by the *Fermi pseudopotential*, defined as

$$\hat{V}_j = \frac{2\pi\hbar^2}{m_n} b_j \delta(\mathbf{r} - \mathbf{R}_j) \quad (16)$$

where b_j is a constant that defines the strength of the interaction and \mathbf{R}_j is the position of the j 'th nucleus. The δ -function means that we model the interaction as a point-like one, i.e. only effective when the neutron hits exactly a nucleus. Since the interaction between the neutron and the nucleus is mediated by the strong force, the range of which is much smaller than the wavelength of the neutron or the distance between nuclei, the δ -function is a good approximation that also simplifies calculations considerably. The Fermi pseudopotential only describes the scattering from the nucleus j , so for the full picture, a sum over all nuclei in the sample must be performed. The density of neutron states in a box of volume Y is

$$\frac{dn}{dE_f} = \frac{Y k_f m_n}{2\pi^2 \hbar^2} \quad (17)$$

Evaluating the matrix elements of equation (15) with the Fermi pseudopotential gives

$$\langle \psi_f | \hat{V}_j | \psi_i \rangle = \frac{1}{Y} \frac{2\pi\hbar^2}{m_n} b_j \int \exp(-i\mathbf{k}_f \cdot \mathbf{r}) \delta(\mathbf{r} - \mathbf{R}_j) \exp(i\mathbf{k}_i \cdot \mathbf{r}) d^3\mathbf{r} \quad (18)$$

$$= \frac{1}{Y} \frac{2\pi\hbar^2}{m_n} b_j \exp(i\mathbf{q} \cdot \mathbf{R}_j) \quad (19)$$

where we define the *scattering vector*

$$\mathbf{q} = \mathbf{k}_i - \mathbf{k}_f \quad (20)$$

which, as we shall see, is one of the most important concepts in neutron scattering.

We now have the matrix elements (18) and the density of states (17) to combine into equation (15). Since this represents the number of neutrons scattered per second, dividing by the neutron flux (7) will yield the total scattering cross section as per (8)

$$\sigma_{tot} = \frac{W_{i \rightarrow f}}{\Psi} \quad (21)$$

$$= \left(\frac{1}{Y} \frac{\hbar k_i}{m_n} \right)^{-1} \frac{Y k_f m_n}{2\pi^2 \hbar^2} \left(\frac{1}{Y} \frac{2\pi\hbar^2}{m_n} b_j \right)^2 \quad (22)$$

$$= 4\pi b_j^2, \quad (23)$$

valid for elastic scattering where $k_i = k_f$ such that they cancel each other out. Also note that the normalisation constant Y cancels out as expected.

We find that the total neutron cross section described in section 2.3 is linked to a value we defined to be the strength of the scattering, b_j . This value is known as the *scattering length*; we will elaborate on this shortly. Given equation (13), we find that the differential cross section must be b_j^2 , as integrating the constant b_j^2 over all solid angles is equivalent to multiplying by 4π .

The importance of the scattering vector \mathbf{q} comes about when we consider the scattering from two nuclei given by the sum of two Fermi pseudopotentials $\hat{V} = \hat{V}_j + \hat{V}_{j'}$. This will give two terms when calculating the matrix elements, and we know from (21) that the scattering cross section is proportional to the square of the matrix elements

$$\sigma \propto b_j^2 |\exp(i\mathbf{q} \cdot \mathbf{R}_j) + \exp(i\mathbf{q} \cdot \mathbf{R}_{j'})|^2 \quad (24)$$

$$\propto 2b_j^2 (1 + \cos[\mathbf{q} \cdot (\mathbf{R}_j - \mathbf{R}_{j'})]) \quad (25)$$

The result is that for some values of \mathbf{q} the total cross section will be zero and no neutrons will be scattered, while for other values it will be up to four times higher than for scattering from a single nucleus. This is an effect of interference, a well-known phenomena in the study of waves in physics.

If we can construct our neutron scattering instruments to measure the \mathbf{q} -value, we can potentially find the \mathbf{R}_j and $\mathbf{R}_{j'}$, the positions of the nuclei that are responsible for the scattering.

2.4.1 Coherent and incoherent scattering

The scattering lengths are intrinsic properties of the nuclei. As the name implies, it has the unit of length and is usually of the order fm but with varying signs. The scattering lengths are taken to be experimentally defined values since, as of yet, no theory is present to calculate them. However, it is found that the scattering cross sections for different nuclei are neither proportional to their Z (element) nor their N (isotope) value, but rather varies in an unpredictable manner. This is in contrast to the case of X-ray scattering experiments where the scattering cross section is proportional to Z^4 due to the fact that the X-rays are scattered by the electrons rather than the nucleus.

The variations in scattering lengths and the low absorption coefficient that many materials have with neutrons are the direct reasons for entries 3-5 in the above list of the neutrons advantages as a probe. We are lucky that it is possible to find hard materials, such as aluminium, that still have a low absorption cross section from which we can make furnaces, cryostats, and the like in which the sample can be kept. These will be almost invisible to neutrons. This is known as the sample environment, and enables us to study phase transitions as temperature or pressure is changed. The differences in scattering length between different isotopes allows us to differentiate between them in experiments.

Variations in the scattering length for a single type of nucleus can arise from changing nuclear spin directions with time, or there can be different isotopes with different scattering lengths. These two contributions can be treated on equal footing, as a macroscopic sample is so large that it represents an ensemble average and the times in which it is observed are larger than nuclear fluctuation

times, which again yields an ensemble average. We assume that the scattering length at site j has the stochastic value

$$b_j = \langle b_j \rangle + \delta b_j \quad (26)$$

where $\langle b_j \rangle$ is the average of b_j and δb_j is the local deviation from b_j , with $\langle \delta b_j \rangle = 0$. Furthermore, the deviations are assumed to be independent between sites such that $\langle \delta b_j \delta b_{j'} \rangle = 0$. Using equation (24) with this stochastic value for b_j , we find that cross-terms arise, such that over a time and ensemble average the differential cross section becomes

$$\langle \sigma \rangle = \sigma_{inc,j} + \sigma_{inc,j'} + |\langle b_j \rangle e^{i\mathbf{q}\cdot\mathbf{R}_j} + \langle b_{j'} \rangle e^{i\mathbf{q}\cdot\mathbf{R}_{j'}}|^2 \quad (27)$$

Here, we have bundled the square of the local deviations $\langle (\delta b_j)^2 \rangle$ into the *incoherent* cross section $\sigma_{inc,j}$, while the second term naturally yields the same result as we found in equation (24), i.e. a cross section proportional to $\langle b_j \rangle$.

The difference between the two is that the *coherent* cross section is dependent on the interference terms, which we earlier postulated was the key to the use of neutrons in experiments. On the other hand, the *incoherent* cross section is completely independent of the interference terms, and as such scatters neutrons isotropically, i.e. in all directions, without us having the possibility to calculate back as we could from the interference terms. Thus, incoherent scattering is generally unwanted, since the incoherently scattered neutrons are in most experiments a source of noise.

2.4.2 Absorption

It is not all neutrons interacting with a nuclei that are scattered. There is a probability for the neutron to be absorbed by a nucleus which subsequently releases α , β , or γ radiation. The amount of absorption is measured by the *absorption cross section* σ_a which is normally proportional to the neutron wavelength, $\sigma_a \propto \lambda$. In the case of absorption cross section for isotope i , the tabulated number is for the "standard" thermal wavelength of 1.798 Å $\sigma_{a,i,th}$, which means that the actual absorption cross section is

$$\sigma_{a,i} = \sigma_{a,i,th} \frac{\lambda}{\lambda_{th}} \quad (28)$$

for use in experiments. The absorption gives rise to an exponential attenuation of the flux inside the sample, with an attenuation constant defined by

$$\mu_a = \sum_i \frac{N_i \sigma_{a,i}}{V} = \sum_i n_i \sigma_{a,i} \quad (29)$$

where N_i is the number of nuclei of isotope i and $n_i = N_i/V$. Nuclei with large absorption cross sections are used to shield against neutron radiation that is otherwise highly penetratable. The most commonly used neutron absorbers are gadolinium Gd, cadmium Cd, and boron ^{10}B . Both Gd and Cd emit high-energy γ -radiation which is in turn different to shield against, with Gd furthermore being expensive and Cd toxic. B, on the other hand, has the advantage that it emits lower energy γ and can be embedded in plastic and molded to shape.

Other uses for nuclei with high absorption cross section are as neutron detectors, as described later in section 9.1.2.

Experimenters have compiled lists of scattering cross sections σ_{tot} and scattering lengths b_j for both coherent and incoherent scattering, and the absorption cross sections $\sigma_{a,th}$ that can be found in sources such as the ILL Neutron Data Booklet [5] or the National Institute of Standards and Technology website [6].

2.4.3 The crystal lattice

When we increase our scattering system from two nuclei as above to real crystals, we must resort to *crystallography* to track the positions of the nuclei. In crystallography, we construct a *unit cell* which describes the simplest possible way to place the nuclei that make up the crystal. The unit cell is then repeated, yielding a periodic *crystal lattice* that makes up the crystal. As crystals are three-dimensional structures, so are the unit cells and crystal lattices, but figure 1 shows a two-dimensional example for ease of understanding. To the left, we see a so-called Bravais lattice which has only one atom per unit cell, while to the right we have a basis, used when a unit cell contains more nuclei per cell.

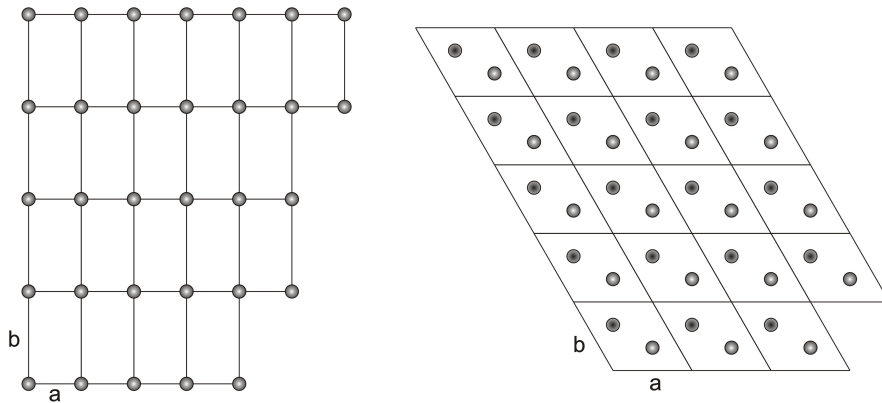


Figure 1: Simple two-dimensional lattices, made by translations of a similarly two-dimensional unit cell. **(Left)** A Bravais lattice, containing one nucleus per cell **(Right)** A basis, containing more nuclei in the same cell.

The labels \mathbf{a} and \mathbf{b} in figure 1 are representing the *lattice vectors* which together with a vector \mathbf{c} linearly independent of \mathbf{a} and \mathbf{b} constitute the natural basis with which to describe the position of a unit cell. This is done through the integers n_a , n_b , and n_c as

$$\mathbf{l} = n_a \mathbf{a} + n_b \mathbf{b} + n_c \mathbf{c} \quad (30)$$

where the \mathbf{c} vector represents the third dimension omitted in the figure. As can also be seen from figure 1, the unit cells need not be cubic or cuboid, but are generally parallelepipeds or hexagonal prisms. The angle between the lattice vectors is α between \mathbf{b} and \mathbf{c} , β between \mathbf{a} and \mathbf{c} , and γ between \mathbf{a} and \mathbf{b} . In a Bravais lattice the nuclei are placed at the lattice points, while for the basis the position of the different nuclei is defined with respect to the lattice points.

The volume of a unit cell is determined by the volume product

$$V_0 = \mathbf{a} \cdot \mathbf{b} \times \mathbf{c} \quad (31)$$

Another useful construct is the *reciprocal lattice*, where the basis vectors are defined by

$$\mathbf{a}^* = \frac{2\pi}{V_0} \mathbf{b} \times \mathbf{c}, \quad \mathbf{b}^* = \frac{2\pi}{V_0} \mathbf{a} \times \mathbf{c}, \quad \mathbf{c}^* = \frac{2\pi}{V_0} \mathbf{a} \times \mathbf{b} \quad (32)$$

From the reciprocal lattice basis we can construct the *reciprocal lattice vectors*. Instead of pointing to a point in real space, these vectors are perpendicular to planes in the real lattice. Again, a set of integers known as the *Miller indices* h , k , and l defines the reciprocal lattice vectors

$$\boldsymbol{\tau}_{hkl} = h\mathbf{a}^* + k\mathbf{b}^* + l\mathbf{c}^* \quad (33)$$

and can be used to calculate the *lattice spacing* d_{hkl} , which describes the distance between lattice planes perpendicular to $\boldsymbol{\tau}_{hkl}$ as

$$d_{hkl} = \frac{2\pi}{\boldsymbol{\tau}_{hkl}} \quad (34)$$

2.4.4 Bragg's Law

From equation (24) we found that, for two nuclei in the scattering system, there were interference effects as $\cos(\mathbf{q} \cdot \mathbf{r})$. Expanding this sum to include all the nuclei in a crystal is done by performing the lattice sum as described in [2]. Here, it is found that

$$\left| \sum_j \exp(i\mathbf{q} \cdot \mathbf{R}_j) \right|^2 \propto N \sum_{\boldsymbol{\tau}} \delta(\mathbf{q} - \boldsymbol{\tau}) \quad (35)$$

such that only when the *Laue condition* $\mathbf{q} = \boldsymbol{\tau}$ is upheld is scattering possible. It is possible to express this condition graphically, using the so-called Ewald sphere. In figure 2 a two-dimensional example is given where the Ewald sphere becomes the Ewald circle. This simplification is justifiable, since many experimental setups are designed to have the scattering vectors spanning the horizontal plane, eliminating the vertical dimension.

The Laue condition can be rewritten into Bragg's Law, one that is widely used in scattering physics. Remembering that $\mathbf{q} = \mathbf{k}_i - \mathbf{k}_f$ we rewrite the Laue condition to $\mathbf{k}_i = \mathbf{k}_f + \boldsymbol{\tau}$ and square each side. Since we have that $k_i = k_f$, this yields

$$\begin{aligned} (\mathbf{k}_f + \boldsymbol{\tau})^2 &= k_i^2 = k_f^2 \\ 2\mathbf{k} \cdot \boldsymbol{\tau} + \tau^2 + k_f^2 &= k_f^2 \\ 2\mathbf{k} \cdot \boldsymbol{\tau} + \tau^2 &= 0 \\ 2\mathbf{k} \cdot \boldsymbol{\tau} &= -\tau^2 \end{aligned} \quad (36)$$

where the last line is possible due to the fact that if $\boldsymbol{\tau}$ is a reciprocal lattice vector, then so is $-\boldsymbol{\tau}$. Equation (36) is known as the diffraction condition. If

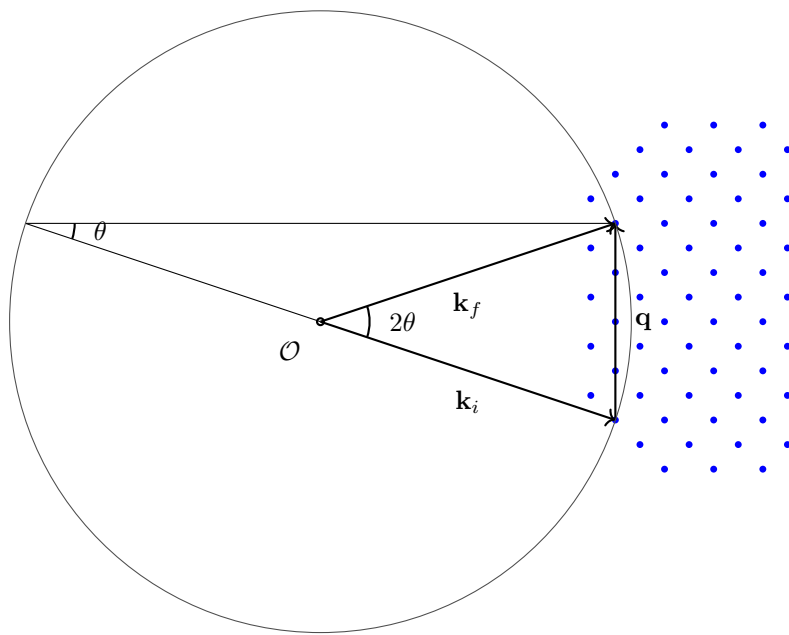


Figure 2: The Ewald circle for an elastic scattering scenario. The blue dots are reciprocal lattice points of the crystal. Whenever the circle (of radius k) intersects a reciprocal lattice point, the Laue condition is upheld and scattering occurs. In this case, \mathbf{q} coincides with a reciprocal vector $\boldsymbol{\tau}$ connecting origo to reciprocal lattice points.

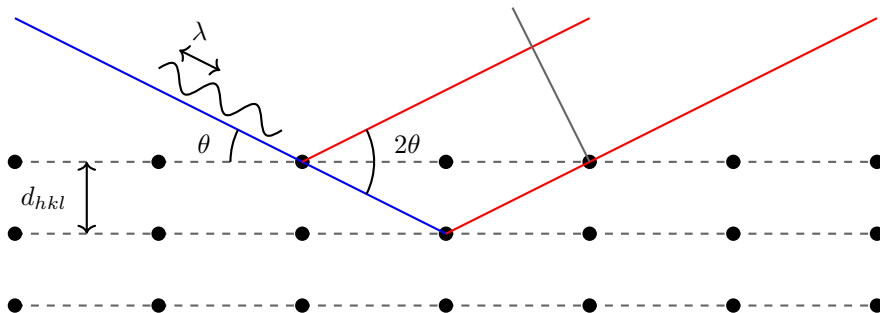


Figure 3: Sketch of a neutron wave of wavelength λ_n impinging on a crystal surface where the crystal has lattice spacing d_{hkl} at an angle θ .

we evaluate the dot product and introduce the lattice spacing instead of the reciprocal lattice vector, we get

$$\begin{aligned}
 2\mathbf{k} \cdot \boldsymbol{\tau} &= \tau^2 \\
 2k\tau \cos(90 - \theta) &= \tau \frac{2\pi}{d_{hkl}} \\
 2\frac{2\pi}{\lambda} \sin(\theta) &= \frac{2\pi}{d_{hkl}} \\
 2d_{hkl} \sin(\theta) &= n\lambda
 \end{aligned} \tag{37}$$

which is known as Bragg's Law. The n is needed, since the reciprocal lattice vector can have a common factor divided out amongst the h, k, l factors.

The physical interpretation of the Bragg equation is the effect of constructive and destructive interference when neutrons are reflected from different crystal planes. The path length difference between neutron waves (as those defined in equation (4)) that are reflected by different crystal planes gives a phase difference. The path length difference changes with the angle of incidence of the neutron upon the crystal planes and the distance between the lattice planes, giving rise to the θ and d_{hkl} dependences. If the path length difference matches a single wavelength, the phase difference is zero and there is constructive interference which gives a λ dependence, and finally there is the possibility that the path length difference matches two or more wavelengths, giving an n dependence. The situation is sketched in figure 3.

The Bragg Law can be used to investigate the lattice spacing of a crystal, as a *rocking scan* where the orientation of the crystal is changed with respect to an incoming, monochromatic beam of neutrons will show a peak of scattered neutrons for lattice spacings that satisfies equation (37). In terms of figure 2, this amounts to rotating the reciprocal points slowly and recording any spikes in scattered intensity. However, the way experimenters find lattice spacings in practice is by grinding the crystal to a powder; this powder then has Bragg scattering surfaces in all directions. A specific lattice spacing will therefore yield a cone of scattered neutrons, called a Debye-Scherrer cone. In the figure, this amounts to overlaying many collections of reciprocal lattice points, rotated in tiny increments, such that different reciprocal lattice points are invariably intersecting the circle.

Expanding upon this technique is Laue diffraction, in which a polychromatic neutron beam is directed at a crystal in a fixed orientation, corresponding to having a range of k -values and hence radii of the circles in the figure, some of which intersect a reciprocal lattice point.

2.5 Basic inelastic scattering

Ordered systems have excitations, and these are quantum mechanical in nature. These excitations can be excited by a neutron, such that the ordered system as a whole is raised in energy. Since we are reluctant to break energy conservation, the energy to excite the system is taken from the neutron. This means that the framework derived in section 2.4 must be revisited, as we here assumed that the interaction between the neutron and the scattering system was elastic, whereas energy exchange between the system and the neutron is per definition inelastic.

One example of an ordered system is a Bravais crystal, where nuclei of the same type are placed at the lattice points. These nuclei can be displaced from their equilibrium points, and as physicists we like to model the movement as that of a harmonic oscillator, such that a nucleus is connected with its nearest neighbour with a spring that obeys Hook's Law and has no influence on the movement of nuclei beyond its nearest neighbours. It is shown in every standard textbook on solid state physics [7] that a disturbance in the lattice (e.i. a displacement of a nuclei away from its lattice point) will propagate as waves with a wave vector \mathbf{Q} and a frequency ω , the relationship between which determines the *dispersion relation*. The wave vectors are quantised, such that *modes* exists with indices $s = \mathbf{Q}, i$, and the Hamiltonian for this simple crystal is just the sum over all modes of Hamiltonians for a harmonic oscillator

$$\hat{H} = \sum_s \hbar\omega_s \left(a_s^\dagger a_s + \frac{1}{2} \right) \quad (38)$$

where the a_s and a_s^\dagger are the annihilation and creation operators for mode s . If we write the instantaneous position of a nucleus \mathbf{R}_l as

$$\mathbf{R}_l = \mathbf{l} + \mathbf{u}_l \quad (39)$$

where \mathbf{l} is some lattice vector and \mathbf{u} is some displacement away from this, then the time dependence of the motion is in the displacement alone, $\mathbf{R}_l(t) = \mathbf{l} + \mathbf{u}_l(t)$. This $\mathbf{u}_l(t)$ we can rewrite in terms of the annihilation and creation operators, which gives

$$\mathbf{u}_l = \sqrt{\frac{\hbar}{2m_n N}} \sum_s \frac{\mathbf{e}_s}{\omega_s} [a_s \exp(i\mathbf{Q} \cdot \mathbf{l}) + a_s^\dagger \exp(-i\mathbf{Q} \cdot \mathbf{l})] \quad (40)$$

With these equations in place, we are ready to tackle the problem of inelastic scattering again, starting over from equation (15). An excitation in the crystal changes the state $|\lambda\rangle$ of the system, and thus it is necessary to take this into account by making the substitution $|\psi_{i,f}\rangle \rightarrow |\lambda_{i,f}\psi_{i,f}\rangle$ such that we are keeping track of both the crystal and neutron state.

$$\frac{d^2\sigma}{d\Omega dE} \Big|_{\lambda_i \rightarrow \lambda_f} = \frac{k_f}{k_i} \left(\frac{m_n}{2\pi\hbar^2} \right)^2 \left| \langle \lambda_i \psi_i | \hat{V} | \lambda_f \psi_f \rangle \right|^2 \delta(E_{\lambda_i} - E_{\lambda_f} + \hbar\omega) \quad (41)$$

As was the case in equation (15), the V is the Fermi potential of equation (16) which models the short-range interaction between the nucleus and the neutron, and we have again defined $\mathbf{q} = \mathbf{k}_i - \mathbf{k}_f$.

We would like to re-cast the above expression into something that resembles the measurements that we perform, since it currently sums a lot of processes where a specific state $|\lambda_i\rangle$ goes into another state, neither of which we have any knowledge about. This can be done by summing over all final crystal states $|\lambda_f\rangle$ and making a thermal average over all initial states $|\lambda_i\rangle$, since we assume the sample is in thermal equilibrium, i.e follows a Boltzmann distribution. The steps taken to reach the observable neutron partial differential cross section are a bit involved, but can be found in both [8] and [2], and the final result is

$$\frac{d^2\sigma}{d\Omega dE} = \frac{k_f}{k_i} \sum_{j,j'} \frac{b_j b_{j'}}{2\pi\hbar} \int_{-\infty}^{\infty} \langle \exp(-i\mathbf{q} \cdot \mathbf{R}_{j'}(0)) \exp(i\mathbf{q} \cdot \mathbf{R}_j(t)) \rangle \exp(-i\omega t) dt \quad (42)$$

The evaluation of the above expression is no simple matter for but the simplest scattering systems.

In the derivation of equation (42), the time-dependent nuclei position operator was defined as

$$\mathbf{R}_j(t) = \exp\left(\frac{iHt}{\hbar}\right) \mathbf{R}_j \exp\left(\frac{-iHt}{\hbar}\right) \quad (43)$$

and we find that we are still at the mercy of the complexity of the Hamiltonian H . This does however also mean that a measurement of the partial differential cross scattering holds information about the dynamics of the crystal through its Hamiltonian.

Inserting the expression for the displacement (39) into equation (42), the time dependence on \mathbf{R} can be moved to the \mathbf{u}_l term alone, since \mathbf{l} is constant and subsequently we can take $\exp(\mathbf{q} \cdot \mathbf{l})$ out of the integral. This factor corresponds to the lattice sum that we calculated earlier.

The time development of \mathbf{u}_l can be easily found, as we have expressed it in terms of the annihilation and creation operators for the harmonic oscillator which has time development

$$a_s(t) = \exp(iHt/\hbar) a_s \exp(-iHt/\hbar) = a_s \exp(-i\omega_s t) \quad (44)$$

$$a_s^\dagger(t) = \exp(iHt/\hbar) a_s^\dagger \exp(-iHt/\hbar) = a_s^\dagger \exp(i\omega_s t) \quad (45)$$

Since \mathbf{u}_l corresponds to vibrations in the lattice, the annihilation and creation operators work on *phonons* which are quantised lattice vibrations.

Equation (42) can be divided into a coherent and an incoherent part, much as we saw in section 2.4.1. Focusing on the coherent part, the expression for the partial differential cross section can be evaluated to

$$\left(\frac{d^2\sigma}{d\Omega dE}\right)_{coh} = \frac{\sigma_{coh}}{4\pi} \frac{k_f}{k_i} \frac{N}{2\pi\hbar} \sum_l \exp\langle U^2 \rangle \exp(i\mathbf{q} \cdot \mathbf{l}) \int_{-\infty}^{\infty} \exp\langle UV \rangle \exp(-i\omega t) dt \quad (46)$$

where $\langle UV \rangle$ means the thermal average of $U = -i\mathbf{q} \cdot \mathbf{u}_0(0)$ and $V = i\mathbf{q} \cdot \mathbf{u}_l(t)$, and the coefficient $\exp\langle U^2 \rangle$ is known as the Debye-Waller factor.

We expand the exponential function into

$$\exp(\langle UV \rangle) = 1 + \langle UV \rangle + \frac{1}{2!} \langle UV \rangle^2 + \dots + \frac{1}{p!} \langle UV \rangle^p + \dots \quad (47)$$

The first term in the expansion corresponds to elastic scattering, and we can reproduce our results from section 2.4 if we integrate over $\exp(-i\omega t)$, yielding $2\pi\hbar\delta(\hbar\omega)$, perform the lattice sum, and integrate over all energies and angles to get the scattering cross section.

If we instead focus on the first $\langle UV \rangle$ term, we can calculate the thermal average of the harmonic modes and see how the partial differential cross section changes. The result is

$$\langle \lambda | UV | \lambda \rangle = \sum_s g_s h_s^* (n_s + 1) + g_s h_s n_s \quad (48)$$

where we see that we have two terms, one of type $\langle n_s + 1 \rangle$, the second of the type $\langle n_s \rangle$. These two terms means that the partial differential cross section consists of two terms. The integration now includes an extra exponential $\exp(-i\omega_s t)$, the combination yielding a δ -function at $(\omega \pm \omega_s)$, valid for the $\langle n_s \rangle$ and $\langle n_s + 1 \rangle$ terms respectively.

Now, the lattice sum that we performed before also contains an extra term of $\exp(\pm i\mathbf{Q} \cdot \mathbf{l})$. This means that we, instead of the Laue condition, get a δ -function at $(\mathbf{q} \pm \mathbf{Q} - \boldsymbol{\tau})$, again for the $\langle n_s \rangle$ and $\langle n_s + 1 \rangle$ terms respectively.

These two δ -functions are equivalent to the two conditions

$$\omega = \pm\omega_s \quad \mathbf{q} = \boldsymbol{\tau} \pm \mathbf{Q} \quad (49)$$

The first set of conditions are linked to the $\langle n_s + 1 \rangle$ and means that the amount of phonons in a particular mode s is increased by 1, at the same time reducing the kinetic energy of the neutron by the amount $E_i - E_f = \hbar\omega_s$, i.e. the energy of a phonon in the same mode s . The neutron creates a phonon in an event known as phonon emission. Furthermore, the creation of a phonon means that a change in momentum is experienced by the crystal, by the amount $\hbar(\mathbf{k}_i - \mathbf{k}_f)$. The phonon wavevector \mathbf{Q} should correct for this, such that $\hbar\boldsymbol{\tau} + \hbar\mathbf{Q}$ combines to ensure conservation of momentum.

The second set of conditions are linked to the $\langle n_s \rangle$ and conversely corresponds to the neutron annihilating a phonon in the mode s , gaining energy $E_f - E_i = \hbar\omega_s$, naturally known as phonon absorption.

Going to higher order in the expansion (47), we will get interactions with more phonon processes, such that the $\langle UV \rangle^2$ corresponds to a two-phonon process, $\langle UV \rangle^3$ is a three-phonon process and so on.

2.6 The scattering triangle

We have encountered the $\mathbf{q} = \mathbf{k}_i - \mathbf{k}_f$ vector in both the expression (24) for elastic scattering and in the expression (41) for inelastic scattering, and we found from the Laue condition (35) that elastic scattering is only possible when $\mathbf{q} = \boldsymbol{\tau}$, and from equation (49) that inelastic scattering will occur only for $\mathbf{q} = \boldsymbol{\tau} \pm \mathbf{Q}$. It seems to be prudent to develop an understanding for these vectors if we are to use them as tools for our scattering experiments. To this end, we construct a triangle from the \mathbf{k}_i , \mathbf{k}_f , and \mathbf{q} vectors in reciprocal space, an example is shown

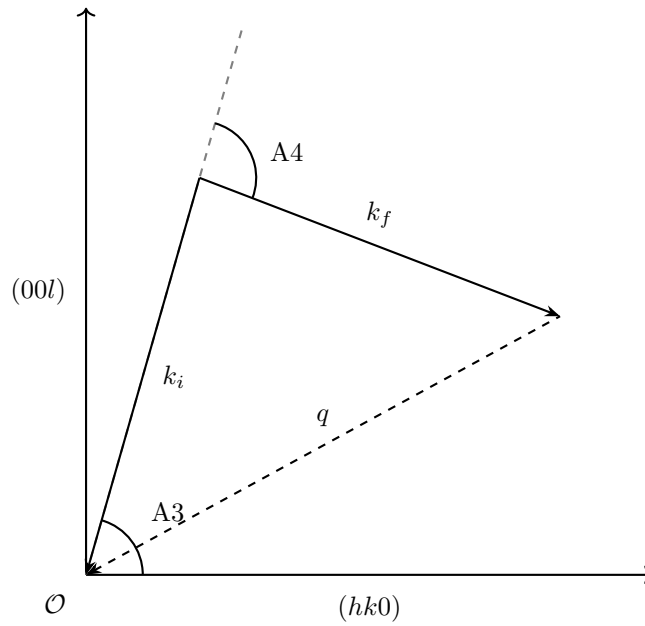


Figure 4: The scattering triangle with \mathbf{k}_i , \mathbf{k}_f and \mathbf{q} .

in figure (4). Two angles are defined in this scattering triangle, one between the sample and \mathbf{k}_i which we shall name A3 and another between the extension of \mathbf{k}_i and \mathbf{k}_f named A4. These angles are important, as we can decide \mathbf{q} by measuring the lengths k_i and k_f and their mutual angles.

Naturally, for elastic scattering we will have $|\mathbf{k}_i| = |\mathbf{k}_f|$ and hence the triangle will be isosceles, having two sides of the same length. For inelastic scattering, $|\mathbf{k}_i| \neq |\mathbf{k}_f|$ and the triangle is not in general isosceles.

Name	Location	Type
ILL	Grenoble, France	R
ORPHEE, LLB	Paris, France	R
BER-II, HZB	Berlin, Germany	R
FRM-2, TUM	München, Germany	R
IBR-2	Dubna, Russia	PR
SINQ, PSI	Villigen, Switzerland	CS
ISIS, RAL	Oxfordshire, UK	S
ESS (from \approx 2019)	Lund, Sweden	S
NCNR, NIST	Gaithersburg, MD, USA	R
HFIR	Oak Ridge, TN, USA	R
NRU	Chalk River, Canada	R
LANSCCE	Los Alamos, NM, USA	S
SNS	Oak Ridge, TN, USA	S
OPAL, ANSTO	Sydney, Australia	R
JRR-3M, JAERI	Tokai, Japan	R
CARR, CIAE	China	R
J-PARC	Tokai, Japan	S

Table 2: A list of the names, institutes, locations and types of the major neutron sources world wide. Here, R represents a reactor while S is a spallation source. The special cases CS is a continuous spallation source and PR is a pulsed reactor.

3 Inelastic neutron instruments

The first use of neutrons as a source for spectroscopy is normally attributed to Bertram Brockhouse at Chalk River Labs in Canada in the period between 1950 and 1962, which led to the invention of the Triple Axis Spectrometer (TAS). This achievement ultimately gave him the 1994 Nobel Prize[9], which was shared with Clifford Shull. In this section, we will focus on the techniques currently employed at neutron scattering facilities to create and move neutrons around, and describe the principles behind the TAS that Brockhouse helped develop and compare this to the competing and complementary technology of the Time Of Flight spectroscopy (TOF), the two methods currently used in inelastic neutron scattering.

3.1 Neutron sources

Neutron experiments are performed at large-scale facilities, since the neutron flux required for experiments in solid state physics is so immense. These large-scale facilities fall into two different categories, based on the method by which they produce neutrons: research reactors and spallation sources. A list of current neutron sources compiled from [10] is shown in table 2.

In research reactors, a fissile material such as a nucleus of the uranium-235 isotope is hit by a neutron, which normally splits the nucleus into two fission products along with 2 to 3 neutrons. These neutrons can then hit another nucleus, splitting it, and giving off more neutrons. This starts a chain reaction that produces more neutrons than it needs to sustain itself; it is these surplus neutrons that can be used for experiments. The nuclear process is given by

$$^{235}\text{U} + n = \text{D}_1 + \text{D}_2 + (2-3)n + Q \quad (50)$$

where the $\text{D}_{1,2}$ is the fission products. Although this is the same nuclear process as in (many) nuclear power reactors, the research reactors are optimised for neutron production and are not used for producing electricity.

A more recent alternative to the research reactors are spallation sources, developed in the mid-seventies with the first prototype, ZING-P, operating at the Argonne National Laboratory in the USA[11]. Spallation sources have a fundamentally different approach in obtaining free neutrons. First, protons which are easily accelerated due to their electric charge is fired into a heavy target at an energy of 1-3 GeV. The target chosen is a neutron-rich element, for example tungsten (W), and the result of the collision is that neutrons are peeled off of the target nuclei. Since the protons hitting the target usually comes in pulses, the neutron beam that the collision creates is also pulsed, and spallation sources are often referred to as pulsed sources. This is in contrast to the research reactors, where the neutrons are coming in a continuous beam.

Currently, the trend for neutron scattering facilities seems to be a move towards spallation sources, as evidenced by the large facilities J-PARC[12] and SNS[13] opened in 2008 and 2007, respectively, and the planned ESS[14]. Reactors face cooling and control problems when the neutron flux is increased beyond current state-of-the-art reactors, most notably the ILL. Comparing ILL with the next major player in neutron science, the ESS, one sees that the time-integrated neutron flux is approximately the same for the two facilities. In the narrow time of a pulse from a spallation source the flux is much higher than for the reactor source, and neutron instruments designed for spallation sources can be optimized to use a larger amount of neutrons in the pulse by time-of-flight techniques. This increases the efficiency of spallation sources.

As a final remark, spallation sources are to a lesser degree the political hot potatoes that reactor sources are.

3.2 Moderators and guides

Since the MultiFLEXX will be used as a part of the FLEXX Triple Axis Spectrometer, the principles of neutron moderators and guides will take as its basis this instrument.

Neutrons produced by neutron sources are way too energetic to be used for probing solid state systems. This means that the neutrons will need to be moderated to have a lower energy, through repeated collisions with some moderator material. Hydrogen atoms are very useful for this, due to their similar size to the neutrons, meaning that they can absorb a large part of the energy from the energetic neutrons. The moderated neutrons will have a Maxwellian energy distribution, with the temperature T that of the moderator temperature. Often, the moderator will be water (H_2O) at 300 K, as this temperature gives neutrons with the desired energies. The neutrons are emitted through the moderator surface, making it an effusion process. Transforming to a wavelength distribution, the neutrons will be distributed according to

$$I(\lambda) = I_0 \lambda^{-5} \exp\left(-\frac{2\pi^2 \hbar^2}{\lambda^2 m_n k_B T}\right) \quad (51)$$

where T is the temperature of the moderator as described in table 1, and I_0 is a constant determined by the neutron source, while λ is the wavelength of the emitted neutron. We will henceforth refer to the neutrons that have passed through the moderator and into the TAS instrument itself as the beam, and say that this beam is white, i.e. has many different wavelengths. The nature of the Maxwellian distribution means that the tail will contain "hot" neutrons, even if the moderator was "cold".

In order to improve the neutron transmission, the moderator will often not be thick enough to moderate all neutrons, which affects the distribution in (51), such that it may be comprised of the sum of several Maxwellians, or have a tail towards higher energies. An example of the wavelength distribution from FLEXX can be seen in figure 5

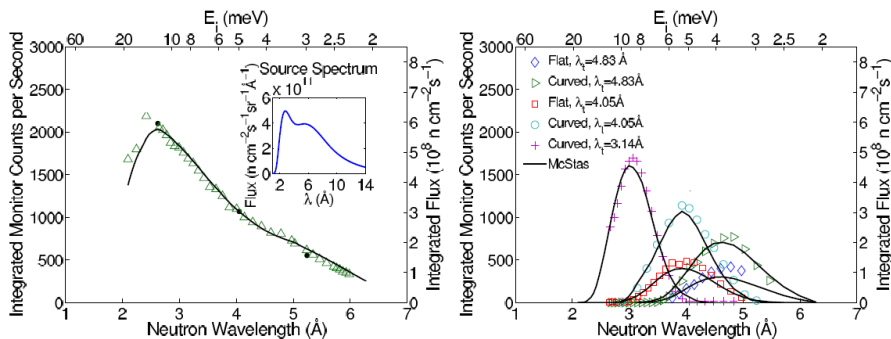


Figure 5: (Left) is the the count rate (green triangles)for neutrons of different wavelengths at the sample position as a function of wavelength. The black line shows a simulation in McStas. The insert shows the same spectrum, but taken immediately after the moderator instead of at the sample position. (Right) we see the transmission of the velocity selector, whose function is described in section 3.4, when it is set to transmit at one particular wavelength. The transmission is shown for three different wavelengths. The maximum transmission of the velocity selector compared to the right spectrum is 70 % at low energies. Figure taken from [15]

To make it possible to have a larger number of instruments at each neutron source and to reduce background counts of high-energy neutrons, a long, curved neutron guide is employed. These guides use the principles also found in optical fibers where neutrons will undergo total reflection if they hit the guide at an angle smaller than the critical angle $\theta_c(\lambda)$. This angle can be found from the critical scattering vector Q_c , and the two are related as

$$Q_c = 2k \sin(\theta_c(\lambda)) \approx 4\pi \frac{\theta_c(\lambda)}{\lambda} \quad (52)$$

Due to modern advances in layered neutrons guide, a non-zero reflectivity is possible up to a higher critical scattering vector than that for single-layer material. This critical scattering vector is characterised relative to the standard material nickel (Ni), by the number m , such that $Q_c = mQ_{c,Ni}$. The majority of FLEXX's guides have $m = 3$, making their effective Q_c three times larger than for an all-Ni guide.

The reason for the curvature is to reduce background from the energetic tail of neutrons that has not been wholly moderated by removing line-of-sight through the guide[16]. The overall shape of the guide can also be modified to focus the neutrons, such that a tapered, parabolic, or elliptical guide will yield a better performance in transporting the neutrons from the source to the instrument[17].

A neutron is said to be having a divergence, which is a measure of how much a single neutrons deviates from the general beam direction. The divergence of the beam is then the largest angle that any neutron in the beam makes with the beam direction, and is measured transversely and horizontally. At different points in the neutron beam path, the beam divergence can be changed by the use of collimators. A collimator can be as simple as two slits of a neutron-absorbing material, where the width (height) of the slits and the distance between them can limit the horizontal (vertical) divergence of the beam by removing neutrons that are not moving parallel to the direction of the collimator. More advanced collimators consisting of a box open in both ends and lamellae of neutron absorbing materials along its length are known as Soller type collimators. For these collimators, the transmission function can be very close to the idealised case of a triangular transmission function.

3.3 The Triple Axis Spectrometer

As the name suggests, the operation of a TAS hinges on the use of three different axis to monochromatise an incoming beam, select an angle, and analyse the scattered neutron energies.

The first and the third of the axes in a TAS are constructions known as monochromators and analysers, respectively. The names cover different uses for the same effect, namely to use Bragg's law to pick a specific energy of neutrons out from the continuum of energies that are created by neutron moderators and the sample, respectively.

From equation (37) it can be seen that it is only when the combination of neutron wavelength, lattice spacing, and angle satisfy Bragg's Law that neutrons can be reflected from a crystal. By using a crystal with a known lattice spacing, any change in the neutrons incident angle upon the crystal will result in a different wavelength being reflected. Thus, simply by rotating a crystal, we can choose a specific wavelength from a continuum of energies. There is a caveat, in the form of the n in equation (37). Any multiple of shorter wavelength neutrons that add up to the wavelength we want to pick out will also be scattered from the crystal, and further measures are needed to ensure that the sample is not hit by these neutrons.

For TAS, there is a naming convention for angles and distances that we will use when describing neutron instruments. Here, distances are denoted LX and angles are denoted AX , with X starting from 1 and increasing in the order with which a neutron beam reaches them.

After having traversed the length of the guide, the neutrons reach a monochromator after $L1$ that will reflect only a specified wavelength λ_i of neutrons due to it being in the Bragg scattering condition, controlled by the experimenter through the angle between the incoming beam and the monochromator, $A1$. The monochromator scatters the neutrons into an angle $A2$. Since we wish to be able to change λ_i , the rest of the experimental setup must therefore be

movable such that the sample can be placed at an arbitrary A_2 when A_1 is changed. In practice, this is done by lifting the instrument slightly from the floor using compressed air and moving it along with electrical motors. It is the angle A_2 between the monochromator and sample that is the first of the three axes in a TAS. This part is also referred to as the primary spectrometer, or the instrument front-end.

The beam next hits the sample after a distance L_2 , which is placed on a sample table that generally moves and rotates in several dimensions for alignment. More often than not, the sample is in some kind of sample environment, e.g. a magnet, a cryostat or something similar. A rotation of the sample, which is denoted A_3 , allows the experimenter to reach different \mathbf{q} -values, as described in section 2.6. Neutrons are scattered according to the \mathbf{q} -value defined by k_i , k_f , A_3 , and A_4 , the angle that the neutrons are scattered in from the sample. Due to this second axis, we now have a whole range of neutrons that leave the sample at a specific scattering angle, but with a host of different neutron energies, since we are doing inelastic neutron scattering and the neutrons gain or lose energy from the sample. This means that we have to determine the amount of neutrons of a specific energy. The angle between sample and analyser is the second angle of the TAS.

To determine the final energy of the neutrons, they are reflected by an analyser at L_3 which functions in exactly the same way as the monochromator, i.e. by having the experimenter change the angle between the incoming neutrons and the analyser to select a specific wavelength λ_f . The angle of the analyser crystal with respect to the beam is denoted A_5 , and correspondingly, the detector that is a distance L_4 away must be placed at an angle A_6 for the neutrons to hit it. The angle between the analyser and the detector is the third axis, and final, axis of a TAS. This is usually referred to as the secondary spectrometer, or the instrument back-end.

3.3.1 A typical TAS experiment

Obtaining $(\mathbf{Q}, \hbar\omega)$ graphs is generally done in two different ways, both of which we can relate to the scattering triangle of figure 4.

In the first of these, the TAS is set to measure at a specific point in \mathbf{Q} space and scans over the energies, i.e. keeping either the initial energy E_i or the final energy E_f constant while varying the other, known as an E -scan or a constant \mathbf{Q} -scan. If $E_i > E_f$ we are *downscattering*, otherwise we will be *upscattering*, depending on whether the sample adds or subtracts energy from the neutron. Changing either k_i or k_f means that the angles in the scattering triangle should be changed as well to keep the position in \mathbf{Q} -space.

In the second method, the TAS scans through reciprocal space at a fixed energy transfer, known as a \mathbf{Q} -scan or a constant E -scan. The direction taken in \mathbf{Q} can be chosen by the experimenter by choosing the angles of the scattering triangle appropriately, although straight lines through \mathbf{Q} in some direction is preferred. For example, a scan where the \mathbf{q} -vector is pointing in the same direction but changes length is known as a \mathbf{Q}_{\parallel} -scan, while measuring perpendicular to the initial \mathbf{q} -vector is a \mathbf{Q}_{\perp} -scan. The latter is achievable by performing a sample rotation for small sample angles.

The method chosen for a particular experiment depends primarily on the type of dispersion that one wish to measure. For example, a very flat dispersion

is best measured by an E -scan for reasons that will be explained in section 6. Both of these methods gives results that are easy to interpret, however.

The first step is normally to determine the orientation of the sample by finding a Bragg peak, after which the surrounding \mathbf{Q} -space can be investigated.

The operation of a TAS focuses on just a few points in (\mathbf{Q}, ω) space like we see in the scattering triangle of figure 4. Changing the settings require several electrical motors to turn large parts of the instrument using compressed air. As a consequence of the focus on a few points, it is important that the experimenter knows where the physical properties of interest in an experiment is found, and going to larger areas of (\mathbf{Q}, ω) space is usually unfeasible. However, the data acquisition for each point is quick due to the relatively high flux of the reactors where TAS are often found.

3.4 The FLEXX spectrometer

The FLEXX TAS is far removed from the simple TAS described above, utilising several improvements to increase neutron flux on the sample and improving resolution and background. In this section, we shall delve into some of the details of a modern TAS.

3.4.1 Monochromator resolution

If we use for our monochromators and analysers a single perfect crystal, we can calculate how large an uncertainty in $\lambda_{i,f}$ we can expect from the scattered beam given the divergence of the incoming beam. If we assume the lattice spacing d to have negligible uncertainty, we can calculate this by differentiating Braggs Law (37) with respect to the angle of the incoming beam, yielding

$$d\lambda = 2d \sin \theta d\theta \quad (53)$$

If we divide this expression with Braggs Law to obtain the relative uncertainty on λ , we get

$$\frac{\delta\lambda}{\lambda} = \cot \theta \delta\theta \quad (54)$$

which, for an angle $\theta = 45^\circ$ and typical divergence $\delta\theta = 0.5^\circ$, yields a relative uncertainty of $\approx 1\%$, and we see that this method gives us a quite well-defined wavelength for the beam. However, we see from the $\cot \theta$ that our relative uncertainty is increasing rapidly as scattering angles are decreasing. This means that a monochromator or analyser that is set to scatter short-wavelength neutrons are reflecting a broader range of neutrons than those that are set to scatter long-wavelength neutrons. This effect is used in the ultra-precise backscattering instruments, where θ is fixed at a value close to 180° .

3.4.2 Mosaicity

If a larger amount of reflected neutrons is needed to sacrifice resolution for higher flux onto the sample, as is often the case in neutron scattering, the width of the reflected beam can also be increased by using analyser and monochromator crystals that have a *mosaic width* or *mosaicity*.

Crystals with a mosaic width do not have their lattice planes completely aligned, rather they are made up of several microscopic crystals that are perfect, but with lattice planes pointing in slightly different directions around some average value[18]. The closer these microscopic crystals are to having all of their lattice planes aligned in the same direction, the lower their mosaic width is. Instead of seeing the sharp peak in reflectivity at the wavelength satisfying Braggs Law, we see a Gaussian peak around it which width is defined as the mosaic width. This broadening is often measured in degrees or Minutes Of Arc (MOA), with $1^\circ = 60$ MOA.

Allowing for this increase in relative uncertainty of wavelength naturally affects the resolution with which the instrument can measure. Therefore, choosing the mosaicity of the analyser crystals is a balancing act between the precision of the instrument and the amount of neutrons that will hit the sample in a given time, and through that the time in which an experiment can be performed.

The mosaic crystals used for the FLEXX monochromator and analyser are made from Highly Oriented Pyrolytic Graphite (PG). This material, that is really a powder in two directions and crystalline in the third, has many properties that make them ideally suited for this use, including a high reflectivity and a behaviour close to that of an idealised mosaic crystal[19].

As described in section 3.3, measures should be taken to prevent neutrons that might undergo second or higher order scattering from reaching the monochromator at all. For FLEXX, a velocity selector is installed along the length of the guide. In the velocity selector, the neutrons pass through a cylinder containing a rotating fan of blades that are tilted with respect to the main beam path. The blades are clad with neutron-absorbing material, and the tilt in combination with the rotational speed of the velocity selector means that only neutrons moving at a specific speed will pass through the velocity selector without hitting a blade and being absorbed. Velocity selectors like this can be used to choose exactly the incoming wavelength, but this comes at a great cost in intensity. For the FLEXX spectrometer, the velocity selector chooses a broad range of neutrons, that is however narrow enough to ensure that there are no neutrons to undergo higher-order scattering from the monochromator, leaving out a source of noise. Furthermore, a lot of neutrons are removed from the beam far away from the detector, leaving them no chance of being accidentally scattered and detected. An example spectrum from the velocity selector can be seen along with the neutron spectrum in figure 5.

For FLEXX, the detector is a so-called 0D-detector, meaning that the detector does not track where the neutron hits, just that a neutron hits the area of the detector. This is in contrast to Position Sensitive Detectors (PSD) that can be obtained in one- or two-dimensional versions that has neutron-sensitive pixels that detects approximately where on a line or a plate, respectively, a neutron hits.

3.5 The Time Of Flight Spectrometer

A very different technique for neutron spectroscopy is the Time Of Flight (TOF) method. This optimises the efficiency of pulsed spallation sources, and as such are often used there.

The major difference is in the measurement of the energy of the neutrons; in a TOF it is done by measuring a delay Δt between some event and the neutron

reaching a detector placed a certain distance L away. The time it takes a neutron to traverse the distance L is dependent on its speed v , which we can convert to the neutron wavelength λ . Rewritten, the delay is given by the equation

$$\Delta t = \frac{L}{v} = \frac{m_N}{2\pi\hbar} L\lambda = \alpha L\lambda \quad (55)$$

where $\alpha = 0.2528^{\text{ms}}/\text{\AA m}$ (the units being milliseconds and Ångström times meters). The relative uncertainty is here determined from

$$\alpha L d\lambda \approx dt = \tau \quad (56)$$

with τ being the length of the pulse leading to

$$\frac{d\lambda}{\lambda} = \frac{\tau}{\alpha L\lambda} \quad (57)$$

and we see that long distances, long wavelengths, and short pulses led to better relative uncertainty[20].

The event that starts the timing is dependent on the type of experiment and source, but is usually the impact of the pulse that creates the neutrons. For the long-pulsed ESS, the event will be one or more Pulse Shaping (PS) choppers that define the pulse time τ which we saw in (57) to determine the relative uncertainty and, through that, the resolution. Another chopper that is set to barely hit the beam after the PS chopper is the Frame Overlap (FO) chopper that removes the so-called frame overlap where fast neutrons from one pulse overtakes the slow neutrons from another, making it impossible to distinguish which pulse to measure delays from and making wavelength determination impossible. At continuous sources, choppers can also be utilised to give a pulsed signal at the cost of losing many neutrons.

With the TOF method, it is only possible to determine either E_i , known as direct TOF or E_f , known as indirect TOF. This means that for inelastic scattering, we need to monochromatise the incoming beam (direct) or analyse the outgoing beam (indirect) to calculate the energy change. Monochromatisation can be done by Bragg scattering as for a TAS, but normally long guides are employed, such that different neutron wavelengths arrive at a monochromatisation chopper at different times. The synchronisation between pulse start and chopper then selects the incoming energy.

Since the TOF measures delays Δt and converts them to energies, this means that a TOF can measure a large (limited by the pulse details only) range of neutron energies more or less smoothly, without changing any settings. No settings are required to change for measurements of different q 's either, as the measurement of the individual neutrons are performed by a detector bank, placed in a semicircle with its centre at the sample, such that a large range of q -values can be measured at the same time. When comparing to the scattering triangle of figure 4 that the TAS can measure, the ToF measures as shown in figure 6.

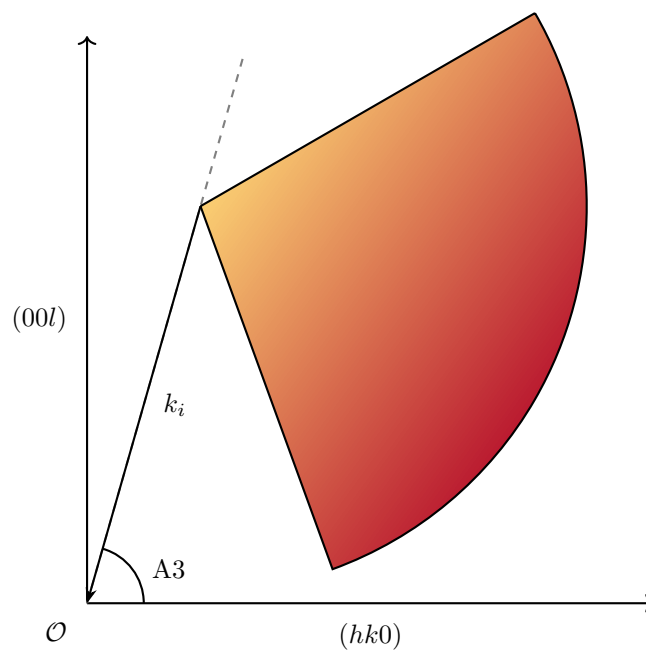


Figure 6: The part of \mathbf{Q} that a TOF can measure at a time. The colour is proportional to the neutron energy we measure at a point. Note that the range in k_f length (the radius of the circular slice) is determined by the time between pulses, and that the angular coverage is usually much larger than the 100° shown in this sketch.

3.6 Advantages and drawbacks

With the TAS and the TOF methods, we have two quite different types of instruments, each with their own advantages and drawbacks that mostly complement each other.

The first comparison to be made is one of measurement area in (\mathbf{Q}, ω) space. Here, the TAS measures just one point after which the instrument will need to change settings to prepare for the next point to measure, while the TOF can measure a large range of both energies and q -values simultaneously. The TOF can thus be used for *mapping*, where the overall structure of the sample is visible. Although this would seem to favor the TOF instruments, comparison number two largely negates this advantage.

While the pulsed neutron sources can be very intense, a lot of that intensity is removed first at the PS chopper, and later at the monochromatisation chopper. This is especially so for a monochromatisation chopper, where the pulse window has to be very small to have good resolution. This is because the distance L to the detectors can not be increased while maintaining the same solid angle covered for the same amount of (expensive) detector area. The result is that the integrated intensity hitting the sample is much lower than in a comparable experiment using a TAS, thus making a TOF measurement a time-consuming ordeal.

The slow data acquisition also means that parametric measurements where the temperature, pressure or other sample environment parameters are changed often are not feasible. This is a major drawback, as experiments showing how the sample behaves in or near phase transitions are one of the staples of neutron scattering. With a TAS, it is possible to focus on the interesting region around the phase transition, yielding higher statistics in the area of interest.

For both methods, the resolution primarily depends on the wavelength as equations (54) and (57) show, with both instruments performing better at long wavelengths, corresponding to a low k . For the TOF, a low k_i gives a good resolution in the entire energy range, which on the other hand is limited exactly by the low k_i , while as we shall see in section 6, the TAS resolution suffers equally if the energy range is large.

Upon comparison of the strengths of both types of spectrometers, we find that there are experiments that are not immediately feasible using either a TAS or a TOF; namely mappings with parametrisation.

4 The MultiFLEXX design - combining advantages

With neither the TAS method nor the TOF method perfect, the prospect of combining the advantages and ignoring the disadvantages of the two have led to new developments in neutron spectroscopy, such as the emergence of multiplexing neutron instruments. There is no fixed definition of multiplexing, but in this thesis we will define it as using several analysers to measure multiple energies and/or angles at the same time.

One of the first instruments to utilize multiplexing was the two so-called Re-Invented Triple Axis spectrometers (RITA and RITA-II) [21] which was developed at Risø in Denmark. RITA-II, which later moved to PSI in Switzerland, has an analyser that consists of nine individual blades that can be rotated independently, such that each blade can scatter a distinct energy. The nine blades share one common position sensitive detector; determining which analyser scattered the neutron is done by recording the position of the detection. RITA-II can also use the blades as a normally focusing analyser in an ordinary TAS setup, or position the blades such that RITA-II can be used for neutron imaging [22].

Many of the multiplexing setups in operation today has vertically scattering analysers, a necessity if several scattering angles are to be measured simultaneously due to the spatial requirements of an analyser-detector pair. This technique was first utilized in inelastic scattering for a rebuild flatcone instrument at HZB [23], measuring at several points in \mathbf{Q} -space but at a single energy at a time.

Also using vertical scattering, the FlatCone [24] at ILL utilizes banks of identical analyser setups, each containing two distinct analysers that are fixed in energy, with both analysers scattering to the same detector. This gives access to a wide range of scattering angles simultaneously, but to determine the incoming energy, one of the two analysers has to be shuttered. The FlatCone is designed to be rotated out of the scattering plane to measure out-of-plane scattering.

The multiplexing trend is also spreading to the ESS, still in the construction phase[14], where the Continuous Angle Multi-Energy Analyser (CAMEA) will employ the multiple analyser setup of the FlatCone, while using a PSD detector to detect differences in scattering angle from the sample and variations of energy, all from a single analyser[25, 26]. The real breakthrough is in the fact that all analysers can be used simultaneously. This is made possible by using PG crystals that are very nearly transparent to neutrons at low energies [27] except of course for energies satisfying Braggs Law. This means that it is possible to place successive analyser crystals in the scattered beam direction, with each analyser scattering the neutrons almost vertically to a dedicated detector. Neutrons of other energies than the one specified for the analyser will instead continue towards the next analyser in the beam direction. These novel features, coupled with the very bright neutron beam of the ESS should yield an increase in gain over a TAS of between 400 and 3700[28] in conservative estimates.

A somewhat different approach is taken at NIST, where the MACS[29] spectrometer is placed. Here, vertical scattering and 20 scattering angles is paired with a double crystal analyser for each scattering angle. The double crystal analysers are arranged to move in coordination with each other, such that neutrons are Bragg scattered to a single detector at a fixed position, with possible

energies between 2.1 meV and 20 meV. This allows for smooth measurement of E_f 's in this range.

Not to be outperformed, the neutron research facilities PSI, MLZ, and HZB are currently planning new multiplexing instruments, taking in design ideas from the extremely ambitious CAMEA. The HZB design, which is to be known as the MultiFLEXX[30], is at the most advanced stage of the three, currently undergoing the final assembly.

4.1 The MultiFLEXX design

The MultiFLEXX will be an optional multiplexing back-end for the FLEXX TAS, to be used at user request. It is a vertically scattering instrument using the CAMEA-type multiple analysers of PG that can be placed in succession of each other, each scattering a single fixed energy. The vertical scattering allows us to have multiple sets of analysers, covering a broad range in scattering angles.

4.1.1 Analyser channels

For the MultiFLEXX, we have opted for 5 analysers in the scattered beam, with an energy range of 2 meV at the fixed energies $E_f = 2.5, 3.0, 3.5, 4.0,$ and 4.5 meV, with the lowest energy analyser closest to the sample. Each analyser-detector pair constitutes an *energy channel*, and the combination of the 5 above-mentioned energy channels are built together into a cassette. These cassettes are identical, and the geometry and set-up of one can be seen in figure 7. Notable from this figure is the shielding made from borated polyethylene (shown in light blue) to prevent crosstalk where a strong signal in one channel is leaking into another channel, and also to reduce background from the experimental area. The cassette has side-walls of aluminum lined with Cd for further shielding, such that the areas of free air propagation within each cassette is fully enclosed. On the end of the MultiFLEXX facing the beam, a thin strip of lead is added under the borated plastic. This acts to shield the detectors against γ radiation created when the borated plastic absorbs neutrons.

The energy channel closest to the sample has the centre of its analyser $L_3 = 1.050$ m from the sample, with the following energy channels having $L_3 = 1.220$ m, 1.387 m, 1.552 m, and 1.732 m.

For each energy channel, a focusing (to be explained in section 5), vertically scattering analyser made from 3 HOPG plate-like crystals of size $20 \times 20 \times 2$ mm will scatter neutrons onto a cylindrical He-3 tube detector of radius 25 mm and active length 50 mm. To obtain the correct geometry for the focusing analysers, they are placed in a holder constructed from aluminium. The analyser crystals have their crystal planes aligned with the large surface of the crystal[31], such that the crystal planes are easily aligned from the analyser crystal shape alone.

The analyser crystals were ordered to have a mosaicity of 40 MOA, the actual values were measured at the E2 diffractometer at HZB[32] to ensure that the crystals were within specifications. Those that had mosaicities outside the specified range were sent back for replacement.

The detector is placed a distance of $L_4 = 0.4$ m from the centre of the analysers. There are no movable parts in the analyser-detector setup. Calibrations, alignments and service of the amount of motors needed to move all analysers would be an insurmountable task, as would be the task of making software to

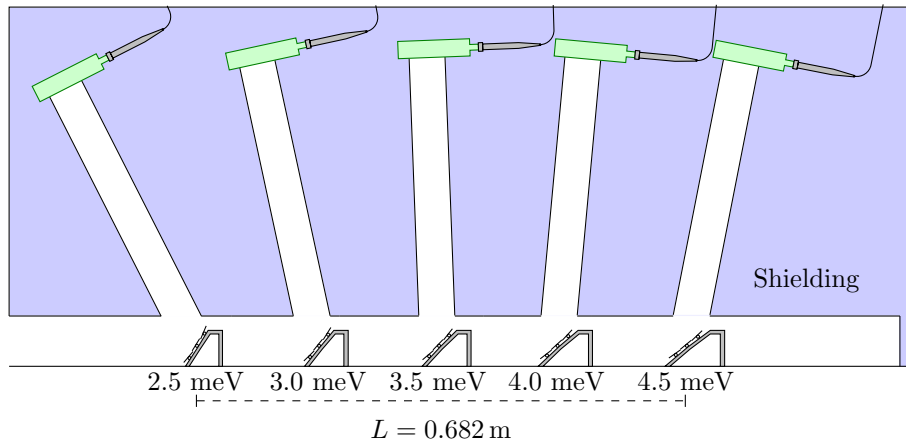


Figure 7: A sketch of the setup showing the 5 energy channels that constitute a single cassette. The analyser crystals are on top of the analyser holders, the triangle structures near the bottom. The detectors are the green rectangles near the top, light blue represents shielding and white is free air propagation. The analysers are curved, the curvature is exaggerated by a factor of 10 for visual clarity.

control it in a sensible manner. Instead, the ability to have a plug-and play alternative set-up and ease of operation for external users have been prioritised. Alignment is done manually and is fixed after the instrument is assembled.

Even though the E_f 's are fixed one can still measure energy transfers relatively smoothly by changing E_i in steps approximately the size of the width of the analyser resolutions, which can be done using the monochromator. An ordinary TAS measuring an energy transfer in steps of e.g 0.15 meV takes 13 steps in E_i to cover energy transfers in a 2 meV range, whereas the MultiFLEXX can cover the same range just as smoothly with 3 steps in E_i .

The setup of a cassette can be made very narrow, which means it is possible to place them just 2.545° apart in a semicircle around the sample. A total of 31 cassettes will cover an angular range of 77° , each measuring a different q -value. In this setup, each cassette represents a q -channel. This is the closest we come to the large semicircle of position sensitive detectors of the TOF described in section 3.5. The MultiFLEXX cannot measure above or below the scattering plane as TOF's can, but will often be used with sample-environment that limits the neutrons scattered out-of-plane.

Compared to the ordinary analyser from FLEXX which uses a much larger focusing analyser, the solid angle coverage is 10 times larger, effectively multiplying the amount of data to be taken by the same amount.

In correspondence to the scattering triangle shown for an ordinary TAS in figure 4 and the continuum of scattering "triangles" for a TOF shown in figure 6, the MultiFLEXX has a host of different scattering triangles, as shown in figure 8 for 2 of the 31 channels, corresponding to the MultiFLEXX prototype that is tested in section 9. It is still possible to change the scattering angle, i.e. the angle between the central MultiFLEXX q -channel and the incoming beam. The

size of the MultiFLEXX back-end might limit this motion compared to the movement that the ordinary FLEXX back-end has.

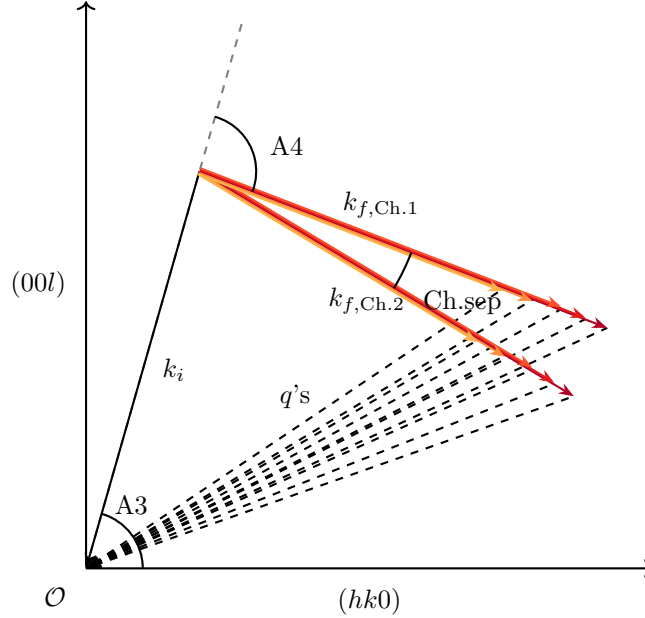


Figure 8: The scattering triangles for an experiment with 2 of the 31 channels of the MultiFLEXX back-end. The colours correspond to the energy of neutrons measured at the \mathbf{Q} -point, with darker colours meaning higher energy.

The MultiFLEXX gives an opportunity for doing neutron experiments where mapping of novel samples can be done quickly, and gives the researchers the possibility to identify regions of interest for further study. For specialised tasks, such as parametric studies of particular regions in (\mathbf{Q}, ω) -space, the standard FLEXX back-end is still a better option, and the instrument user can choose which of the two back-ends to use for the task at hand.

4.1.2 Beryllium filter

The FLEXX spectrometer has a velocity selector to remove second order scattering from the monochromator, but this is not always sufficient. For example, downscattering from $E_i \approx 10$ meV will see the 2.5 meV analyser second order scatter the elastically incoherent signal of the sample and background, and for higher incoming energies this will be a problem for the other energy channels as well. Thus, a filter might be required to discriminate against high-energy incoherently scattered neutrons. In our case, the ideal filter would be opaque to neutrons with an energy higher than around 9 meV to avoid second order scattering from the 2.5 meV analyser, or preferably down to 5 meV to cut off all the neutrons that will never be detected anyways, reducing the amount of background neutrons near the detectors.

Therefore, it has been suggested that the MultiFLEXX should have a filter to be situated immediately in front of the entrance to the q -channels. A filter can

be made that exploits that there is a maximum wavelength at which a neutron can be scattered by Bragg scattering of

$$\lambda_{\text{cutoff}} = 2d_{\text{max}} \quad (58)$$

and a suitable material might be found which is transparent to all wavelengths $\lambda > \lambda_{\text{cutoff}}$, but will scatter shorter wavelengths. This is the concept behind a Bragg-scattering filter. A candidate for our filter is a Beryllium (Be) crystal which has $\lambda_{\text{cutoff}} = 3.9 \text{ \AA}$ such that energies larger than $E_{\text{cutoff}} = 5.2 \text{ meV}$ are filtered.

The filter is made from poly-crystalline Be, since we want as many orientations as possible of the crystal planes to scatter the neutrons to be filtered, while the neutrons that we want to detect are unaffected by the orientation of the scattering planes anyway. The result is that almost all high-energy neutrons are filtered out of the neutron beam, and according to [33] a 15 cm polycrystalline filter has a transmission of just 2.6×10^{-5} at 36 meV.

To suppress inelastic scattering by phonons which decreases the transmission for $E < E_{\text{cutoff}}$, one will typically cool the Be filter with liquid nitrogen. This more than doubles the transmission of neutrons in the desired range[33].

4.2 Experiments with the MultiFLEXX

In a single setting, the MultiFLEXX will cover 31 q -channels \times 5 energy channels, meaning it will measure 155 points in (\mathbf{Q}, ω) simultaneously. This is naturally more than the one point measured by a TAS, but far from the continuous coverage of a TOF.

To access 155 other points in (\mathbf{Q}, ω) the sample can be rotated. This corresponds to rotating the coordinate system in figure 8 without moving the scattering triangle, and is also the way in which a TOF changes where in \mathbf{Q} it measures. This draws out arcs in Q -space, one for each of the 155 channels, and due to the different energies of the analysers, each arc will be measured at one particular energy.

Another possibility for MultiFLEXX operation is the so-called A3-A4-scans. Here, the detector array (A4) moves with the same angle as the sample (A3), changing both the direction and length of q 's and the sample rotation. This will cover an area in \mathbf{Q} such that it is measured thoroughly at different energies as well, making it a mapping scan over a specific area of \mathbf{Q} , giving the instrument a flexibility that a TOF does not possess.

The complex measurements means that an experiment on the MultiFLEXX demands some planning. As a help, software has been created that will show the effect of the different scans.

5 Analyser geometries in neutron scattering

Inelastic neutron scattering as a technique has always been severely limited by the feeble amount of neutrons that our current sources can supply. Therefore, it is in the instrument scientist's interest to make the best use of every neutron that is emitted from the sources, i.e. having them interact with the sample and counted in the detector.

In section 3.4, it was discussed how the use of mosaic crystals could increase the amount of neutrons scattered off monochromators and analysers in a TAS, at the cost of a substantial decrease in energy and \mathbf{Q} resolution.

Another way to increase the flux is to *focus* the neutrons by abandoning flat monochromators and analysers and instead curving them, in the same way that radio telescopes focus their faint signal onto a single point. The curved surface that we employ should ideally *spatially focus* a neutron beam onto a single point, or at least to a small area, increasing the flux in that area all the while maintaining *monochromatisation*. Depending on the situation at hand, focusing can increase the flux and perhaps even improve the energy resolution.

The amount of neutrons delivered to an experiment can be increased by increasing the cross section of the guide. This approach is problematic, as larger guides leads to larger possible divergences at the sample and hence poor resolution. Therefore, the first attempts at utilizing focusing was the use of taller guides and vertically focusing monochromators that would focus the neutrons down in the scattering plane at the sample position[33]. This severely reduces the resolution out of the scattering plane, which is normally not a problem, as the scattering plane is often the symmetry plane of the crystal.

For a further increase in flux, instrument designers next began using horizontal focusing. This situation demands more care, as we use the incident angle on the monochromators in the scattering plane to monochromatise the incoming beam. Simply curving the monochromator in the horizontal direction as we did in the vertical direction will result in loss of E -resolution.

In the following, we shall investigate the two limiting cases of incoming neutrons, the *parallel-to-parallel* case and the *point-to-point* case. In the first case, neutrons are incoming with zero divergence and are exiting again with zero divergence. It is clear that for a flat monochromator, the width of the beam is the same before and after reflection and that the beam (if we neglect mosaicity and variations in lattice spacing) is fully monochromatised. The case is sketched in figure 9.

The second case is more difficult, as the divergence of the neutron beam from a point source does not produce a monochromatic beam on a flat monochromator due to the changing incidence angles. Changing the monochromator angle gradually, such that at each point the monochromator is in the Bragg-condition for the required monochromatisation is possible. The change ϕ in monochromator angle θ_M needed to bring a point on the monochromator back into the Bragg condition is simply

$$\phi = \tan^{-1} \left(\frac{h}{L_0} \right). \quad (59)$$

where L_0 is the horizontal distance from the source to the reflection point, and h is the vertical ditto. If we have a range of smaller monochromator crystals

fulfilled as discussed above. This leads us to the *monochromaticity circle* of radius R_M , where the crystal planes should lie parallel to the circumference. R_M is calculated from

$$R_M = \frac{L_1 + L_2}{2 \sin(\theta)} \quad (62)$$

and the centre, in the same coordinate system as above, at

$$x_M = R_M, \quad y_M = 0 \quad (63)$$

such that the normals to the crystal planes are converging on the point where the Rowland circle crosses the x -axis. The Rowland geometry has been shown [35] to better monochromatise a Bragg-reflected peak while increasing flux compared to a flat monochromator.

The Rowland circle R_G and the monochromatising circle R_M can be seen in figure 10, for distances $L_1 = 2.0$ m and $L_2 = 1.0$ m. Since the lengths are not equal, we say that this is an asymmetric Rowland geometry. The asymmetric Rowland has an angle $\delta\theta$ between the normals to the two circles at the point B . This angle goes to zero as the Rowland geometry approaches the symmetric case, i.e. $L_1 = L_2$.

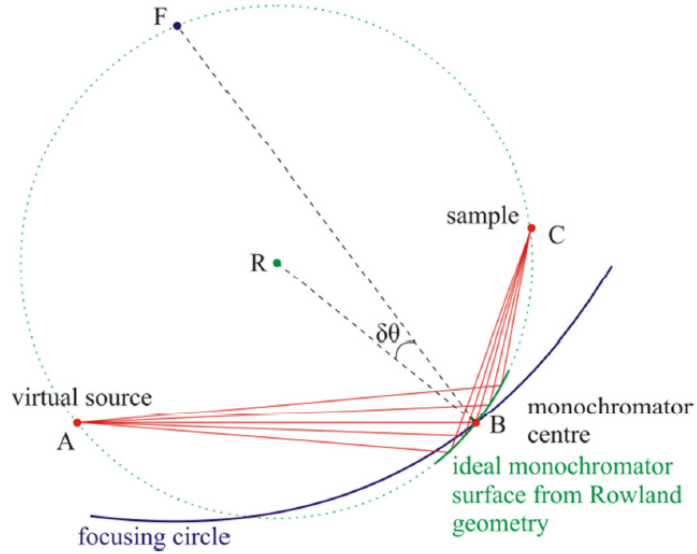


Figure 10: The Rowland geometry drawn for $L_1 = 2.0$ m and $L_2 = 1.0$ m. The **green** dashed circle shows the geometrical circle where A , B , and C should be placed for spatial focusing, while the **blue** circle is the direction that the reflecting lattice plane should follow. **Red** lines are incident and scattered neutrons. Figure taken from [35].

5.2 The situation for FLEXX and MultiFLEXX

5.2.1 Rowland in the FLEXX monochromator

If we examine the situation where $L_1 = L_2$ (symmetric Rowland), we find that $R_M = 2R_G$, while $\delta\theta = 0$. This means that the two circles are each others tangents at origo, and even though their radii are different by a factor of two, they follow each other closely near origo.

This result is an uplifting one, as we see that for the two lengths equal, we get near point-to-point focusing over a range of divergences as a bonus when we curve our monochromators to obtain perfect monochromization. With modern guides, such as the one at FLEXX after its upgrade[15], it is possible to focus the neutrons at the end of the guide into a *virtual source*, which can be made almost point-like by using slits. In many experiments, the sample will also be approximately point-like, due to its small size compared to the distance to the monochromator. Therefore, the distances from the virtual source to the monochromator and from the monochromator to the sample position are chosen to be equal such that the symmetric Rowland geometry can be employed. This makes it possible to focus for a range of different E_i 's by simply turning arrays of monochromator crystals around their own axis, instead of shifting them around in space to follow the Rowland circle.

If the distances are unequal, and hence the monochromating circle and the focusing circle not approximately equal at the monochromator position, maintaining focusing and monochromatisation will become dependent on a lot of motors moving and rotating the individual crystals. This adds complexity, and should be avoided.

5.2.2 Rowland in the MultiFLEXX

For our MultiFLEXX setup, the distances L_1 and L_2 , which are here L_3 and L_4 due to the naming conventions discussed in section 3.3, as well as the angle $\theta_A = A5$ are fixed. This means that the holder for the analyser crystals is fixed and there are no mechanical reasons not to investigate an asymmetrical Rowland geometry. The small width necessary for an analyser to fit in a MultiFLEXX cassette means that only vertical focusing can be used.

However, the analyser height compared to the sample is not very large in the MultiFLEXX, so we can hardly approximate the setup to a point-to-point case. Generally, the complexity of situations like this means that what is optimal for limiting cases might be far from the optimal in a real experimental setup. Therefore, numerical calculations such as McStas simulations are important to verify that the theoretical findings will also work when they are employed in the MultiFLEXX back-end.

Inspecting the analyser geometry for the initial choices of lengths, where $L_3 = 1.05$ m or larger and $L_4 = 0.4$ m, we find that the three analyser crystals should be placed as seen in figure 11(Top left). This will pose a problem, as a neutron hitting the two lower analyser crystals are shaded by the crystal immediately above it. The shading occurs because the difference in angle between the upper and lower analyser crystals with respect to the central Bragg angle is smaller than the mosaicity of the crystals, so we cannot benefit from the transparency of the PG crystals that enables us to put several analysers along the same line. The result is that a neutron scattered by the lower analyser crystals

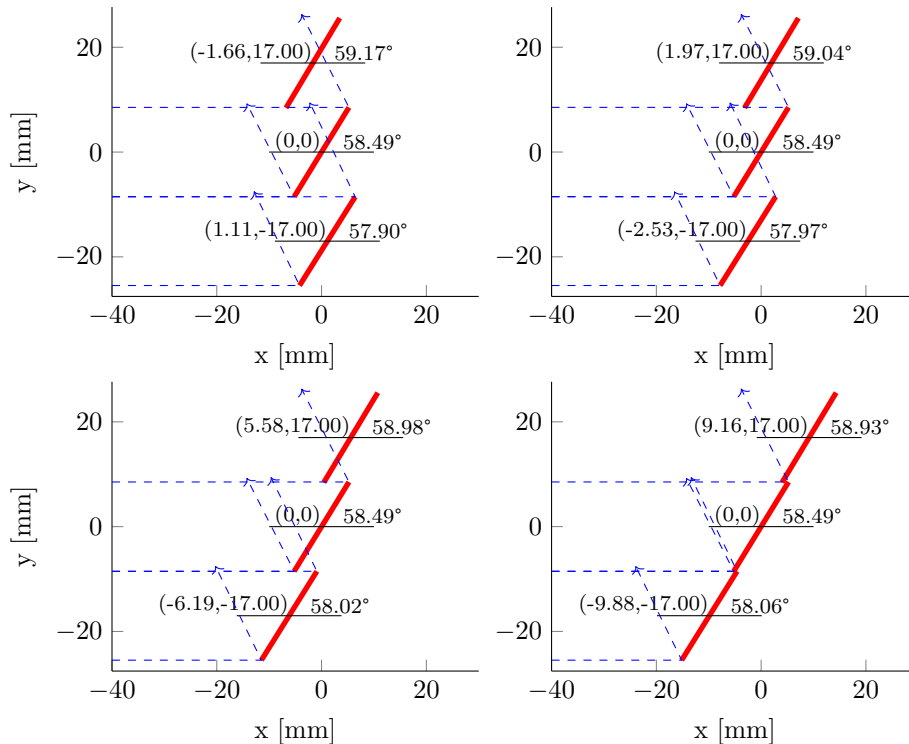


Figure 11: The positions and angles of the three analyser crystals for the Rowland geometry in the 2.5 meV energy channel for different lengths L_4 . (Top left) is the Rowland geometry for $L_4 = 0.4$ m, corresponding to the distance in our setup. (Top right) has $L_4 = 0.6$ m, (Bottom left) has $L_4 = 0.8$ m and (Bottom right) has $L_4 = 1.0$ m. The shading problem disappears gradually as L_4 approaches L_3 .

will still be within the scattering condition for the upper ones and be reflected further back along the q -channel. Since we have chosen the mosaicity to be at approximately 40 MOA for our trade-off between intensity and resolution, we must change the geometry to ensure that the neutrons from the lower analyser crystals are not shaded, or that the angular difference between the individual analyser crystals should be larger than the mosaicity.

The effects of changing the geometry, i.e. the ratio between L_3 and L_4 , can also be seen in figure 11. Here, we see how edging the ratio closer to 1 and hence approaching the symmetrical Rowland geometry will remove the shading problem.

Changing the ratio is, however, not a possibility. The distance L_3 cannot be made smaller, as the wide range of sample-environment possibilities that will be one of MultiFLEXXs virtues needs space, as does a beryllium filter and the motors for turning the MultiFLEXX rack. Also, placing the analyser too close to the sample will harm the \mathbf{Q} resolution. This is, however, yet another balancing act, as large distances between sample and analyser means that the analyser covers a smaller solid angle, making it less effective.

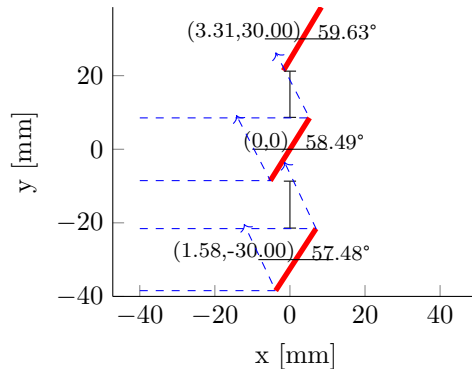


Figure 12: The positions and angles of the three analyser crystals for the Rowland geometry in the 2.5 meV energy channel with the analyser crystals vertically spaced to change their relative angles beyond their mosaicity. This simultaneously solves the problem of the shaded analyser crystals.

Another strategy could be to elongate the distance L_4 to better match L_3 . This, however, poses another problem, namely materials. In its current configuration, the MultiFLEX rack weighs in at about one tonne. By more than doubling the distance to the detector, a lot of shielding has to be added which increases the weight of the system, meaning that the motors that power the ordinary FLEX back-end would also need to be upgraded. This time the detectors will also suffer from the smaller solid angle that the analysers will represent, leading to poor intensity. The initial choice for L_4 was 0.2 m distance for this reason, and the doubling to the current value was due to fears of too high background from neutrons air scattering their way up through the E -channels. Now, the narrow channel in which the neutron can propagate acts essentially as a collimator.

Instead of removing the shading, spacing the analyser crystals further apart vertically will tilt the analyser crystals more with respect to each other. Thus, the upper analyser crystals become transparent to the neutrons scattered from the lower analyser crystals. To tilt the analyser crystals to an angular difference of approximately 1° , we use 3 cm of vertical spacing between the centres of the analysers for the 2.5 meV channel. This is plotted in figure 12, and we see that moving the crystals so far that they become transparent again also removes some of the initial problem of shading. It does, however, create large gaps between the analysers such that the increase in energy resolution is outweighed by the loss in intensity.

In the end, although the Rowland geometry would in principle be the better option for our analysers, the exact parameters for L_3 and L_4 for the MultiFLEX means that we are experiencing shading problems. Therefore, we must find other ways of focusing our analysers.

5.3 The curved analyser

An alternative to the Rowland geometry is a simple curved analyser, i.e an analyser surface that follows a cylinder that has a centre and a radius which we

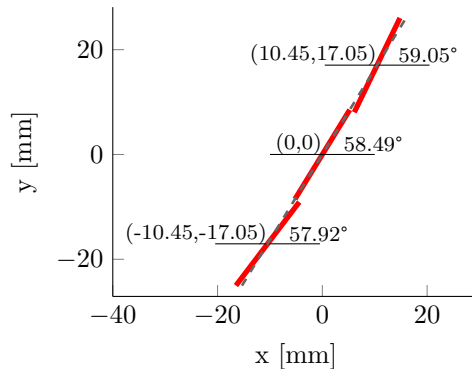


Figure 13: The positions and angles of the three analyser crystals for the cylindrical geometry in the 2.5 meV energy channel. The R_c is the optimal for the situation as calculated in equation (64), with the angular difference between the central and the lower and upper analyser exaggerated by a factor of 10. The grey dashed line shows that the analyser crystals are all in the same plane.

shall name the radius of curvature, R_c . From [35] we have that the theoretical optimal value for the horizontal R_c is

$$\frac{1}{L_1} + \frac{1}{L_2} = \frac{2}{R_c \sin \theta_M} \quad (64)$$

Since the standard is to have adjustable R_c 's to accommodate different analyser energies, we will normally place the analyser crystals such that they lie on the plane of the central analyser, instead of being placed end-to-end. For the same parameters as the analyser in figure 11, i.e. a 2.5 meV channel, figure 13 shows the geometry of an optimally curved cylindrical analyser. Since the R_c 's are usually large compared to the size of an analyser, the angular difference between the middle and upper/lower analyser crystal are exaggerated by a factor of 10.

This curved analyser should theoretically be inferior to the Rowland geometry, but can be made to fit the specifications of our instrument design. The performance of the curved analyser geometry will be evaluated in McStas in section 8.1.

6 Resolution of neutron instruments

As noted in the introduction to this thesis, section 1, due to the limited neutron flux and the small scattering cross section, we are forced to increase the amount of neutrons that are accepted into the experiment, at the cost of the precision with which our samples can be measured. This is done by allowing some neutrons with a non-zero divergence to be scattered off analysers and monochromators. Thereby, the information on the scattering angle is blurred, either through the mosaicity described in 3.4.2 or through curved analysers as described in 5.

Furthermore, we do not control the neutrons perfectly, such that the idealised case we model is never attainable. For example, even perfect crystals that have no mosaicity will still possess an intrinsic linewidth due to other effects.

When the above effects are combined, they will manifest themselves in one of the most important parameters of neutron instrumentation: the *resolution* of the instrument. This describes the size of the features that can be investigated using the instrument; a coarse resolution instrument looking at a narrow feature will likely miss a lot of information, or maybe even the entire feature.

6.1 The resolution function

The actual neutron energy and momentum transfer will be distributed in some small region around the average values (\mathbf{Q}_0, ω_0) , rather than at exactly one point. Their distribution is described by a function peaked at (\mathbf{Q}_0, ω_0) and decreasing for deviations away from this value, known as the *resolution function* $R(\mathbf{Q} - \mathbf{Q}_0, \omega - \omega_0)$.

Instead of measuring the true scattering signal $S(\mathbf{q}, \omega)$ directly, the measured signal is actually a *convolution* between the resolution function and $S(\mathbf{q}, \omega)$, which means that the resolution function is critical to good measurements. A convolution will combine two functions into one that describes the amount of overlap as one function is shifted over the other, and is calculated as

$$(f * g)(x) \stackrel{\text{def}}{=} \int_{-\infty}^{\infty} f(y)g(y - x) dy \quad (65)$$

Covering the resolution function in depth is beyond the scope of this thesis. We shall simply state that it can be approximated analytically to be a 4-D gaussian ellipsoid[36]:

$$R(\mathbf{X}) = R_0 \exp(-1/2\mathbf{X}^T\mathbf{M}\mathbf{X}) \quad (66)$$

where R_0 is the optimum value of the resolution function, i.e. at $R(\mathbf{Q}, \omega)$, $\mathbf{X} = (\mathbf{Q} - \mathbf{Q}_0, \omega - \omega_0)$ and \mathbf{M} is the 4-dimensional covariance matrix that is determined from the collimation and mosaicity values of the instrument. Furthermore, the covariance matrix can be extended[37] to include spatial effects, that is monochromator and analyser curvatures, and vertical scattering as in the case for the MultiFLEXX[23].

Setting $\mathbf{X}^T\mathbf{M}\mathbf{X}$ equal to $p = 1.386$ will yield the 50% (of R_0) probability resolution ellipsoid, a 4-dimensional ellipsoid where each dimension defines the

resolution in $\omega, Q_{\parallel}, Q_{\perp}, Q_z$. In many cases, Q_z is ignored and the resolution ellipsoid is depicted as a flattened cigar.

The convolution between the scattering function and the resolution function means that, for a δ scattering function such as a perfect Bragg crystal, we can directly measure the resolution function at the point $(\mathbf{Q} = 2\pi\boldsymbol{\tau}, \omega = 0)$ by taking the width of the broadened peak that we measure when we scan over the incident angle of the crystal. Furthermore, the convolution between two Gaussian functions is yet another Gaussian, with their widths added in quadrature. The Gaussian is important since we primarily have Gaussian resolutions, and scanning over e.g. a mosaic crystal, we find that the experimentally determined width is comprised by the resolution and the mosaicity combined. Of course, scattering functions can be found in many shapes, and δ and Gaussian functions are just the simplest examples.

6.1.1 Focusing measurements

The resolution ellipsoid has a volume, shape, and orientation that depends on (\mathbf{Q}_0, ω_0) , parameters that can be chosen to some extent by the experimenter by picking the setup of the instrument. As mentioned earlier, this will affect the way measurements are performed.

If we measure dispersions instead of Bragg peaks, we scan our resolution ellipsoids over surfaces instead of points in (\mathbf{Q}, ω) . This means that the shape of the ellipsoid can have an effect on the intensity, as we move the ellipsoid in (\mathbf{Q}, ω) when we perform \mathbf{Q} or E scans. This is why, for flat dispersions, it makes no sense to scan the ellipsoid parallel to the dispersion in a \mathbf{Q} -scan, as we will either have continuous overlap or no overlap, i.e. signal for all scan values or for none. One example of a flat dispersion is for incoherent elastic scattering. This can be used to measure the energy part of the resolution, where an E -scan will reveal the width of the ellipsoid in that direction.

The different orientations of the resolution ellipsoid means that measurements can be optimized for a specific situation. When measuring a dispersion, it will be favorable to have the two long axes of the ellipsoid parallel to the dispersion surface to minimize the overlap (i.e. convolution) outside of the actual point of measurement. The situation is shown graphically in figure 14 in two dimensions, and as it can be seen, the correctly aligned ellipsis will overlap the dispersion surface for a smaller amount of steps at a higher intensity. This usage of the resolution function is known as *focusing*[38], and although one cannot always choose the optimal focusing, there is usually a choice between more focused and less focused setups.

6.2 Resolution matching

When designing a neutron scattering instrument, there is always a trade-off between signal and resolution. It is, however, important that all the elements of an instrument has approximately the same trade-off for optimal performance. For example, if we mindlessly improve resolution only on the front-end or on the back-end, we will be limited by the resolution of the other.

The amount of signal reaching the detector can be modelled as

$$C = A\sigma_1\sigma_2 \tag{67}$$

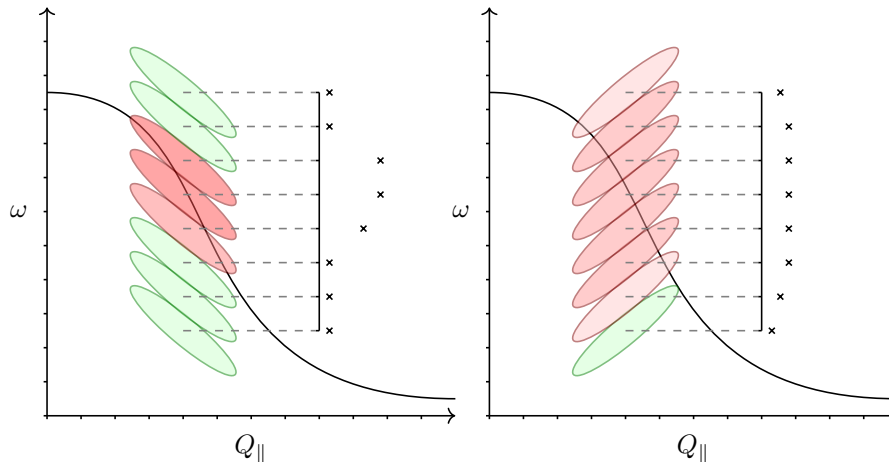


Figure 14: Two examples of an ω -scan over the same dispersion. (Left) A close-to-optimally focused resolution ellipsoid where it can be seen that the overlap region between resolution ellipsoid and the dispersion is minimised. (Right) A non-focused resolution ellipsoid where the overlap region between the resolution ellipsoid and the dispersion is present for many of the measurement points. The inserts approximate the measured data based on the amount of dispersion within the resolution ellipsis area, as does the color of the resolution ellipsoids.

where C is the count rate and A is some constant that links the acceptances σ_1 and σ_2 to the count rate. The acceptances are essentially the "resolutions" of each of the spectrometer parts. Trying to find their combined resolution, assuming they are Gaussian, we find

$$\sigma = \sqrt{\sigma_1^2 + \sigma_2^2} \quad (68)$$

and we can find the best relationship between the two resolutions σ_1 and σ_2 . For a constant count rate C , we can minimise σ in equation (68) by first rearranging equation (67) into $\sigma_2 = C/A\sigma_1$ and inserting this back into equation (68). This yields

$$\sigma = \sqrt{\sigma_1^2 + \left(\frac{C}{A\sigma_1}\right)^2} \quad (69)$$

which we differentiate with respect to σ_1 and set equal to 0

$$\frac{\delta\sigma}{\delta\sigma_1} = 0 = \frac{2\sigma_1 - 2\frac{C^2}{A^2}\sigma^{-3}}{\sqrt{\sigma_1^2 + \left(\frac{C}{A\sigma_1}\right)^2}} \quad (70)$$

$$\sigma_1 = \frac{C^2}{A^2}\sigma^{-3} \quad (71)$$

$$\sigma_1^4 = \frac{C^2}{A^2} \quad (72)$$

$$\sigma_1 = \sqrt{\frac{C}{A}} \quad (73)$$

which, when inserted into equation (67) leads to $\sigma_2 = \sqrt{C/A} = \sigma_1$. This is known as *resolution matching* and shows that, for the same count rate, the most narrow overall resolution is obtained when the front-end and back-end of the instrument have the same resolution. One might have come close to this result by simply reasoning that, due to adding the resolutions in quadrature, the broader resolutions will dominate in the combined resolution.

7 Neutron simulation

Instead of the approximate analytical calculations on neutron instrument design that was mentioned in section 6, simulations of planned neutron instruments are becoming increasingly important. Since the work on analytical calculations were done, neutron instruments have greatly increased in complexity and a series of simulations can be used to test novel ideas before expensive prototypes are built or to give an impression of the performance of a newly designed instrument. The increase in computing power also means that optimisations can be done automatically, with algorithms searching for the optimal instrument parameters as in [39] or finding the best possible guide as with [40].

For the MultiFLEX upgrade, we have constructed the instrument in the Monte Carlo (MC) neutron ray-tracing package McStas (Monte Carlo Simulation of triple axis spectrometers)[41, 42, 43].

McStas is a tool for simulating neutron instruments which has been in ongoing development since its first release in October 1998, where it was first used at the Danish research centre Risø for their neutron source DR3. The Technical University of Denmark, the University of Copenhagen, the Paul Scherrer Institute (PSI), and the Laue-Langevin Institute (ILL) are the driving forces in the development and maintenance of McStas, which had its latest version 2.1 released in September 2014. McStas is one of several such tools, notable others still being developed are VITESS [44] and RESTRAX [45].

7.1 The Monte Carlo method

The MC method of simulation was developed by Stanislaw Ulam, at a time where he was working at the Los Alamos National Laboratory during the nuclear weapon projects in the 1940'ies[46].

The MC method uses repeated random sampling in order to get numerical results. Normally, one defines a domain of possible inputs and generate a lot of random numbers in the same domain drawn from a specified distribution. Afterwards, each random number in the domain is tested against some deterministic algorithm, and the statistics are gathered. A classic example of the use of the MC method is the computation of π from the ratio of the area of a square and the inscribed circle. This experiment can be performed with grains of sand or arrows, but it can also be simulated using computer-generated random numbers.

In principle, the behaviour of scattering neutrons can be calculated if the initial conditions are known. This, however, requires solving complicated integrals over all relevant parameters which cannot necessarily be done analytically, but using MC we can make an estimate for these integrals that converge to the right answer when we use sufficiently many random numbers.

7.2 The McStas system

McStas contains a so-called "meta-language" in which pre-made components are assembled into a virtual neutron instrument by the user. The instrument is then compiled into the programming language C, which in turn performs the simulation using MC calculations and writes data files that can be visualized or further processed.

To simulate an instrument in McStas, one must first list the various components that mirror the effect of experimental equipment on the neutron path. There are components for sources, monochromators, samples, and detectors in different shapes and forms, and furthermore different types of neutron optics that will affect the neutron beam. McStas comes with a large library of components, most of which are coded by the developers. Others are contributed by users, to solve more specialized problems.

The components are given a position and rotation in a right-hand coordinate system where they can be placed at absolute positions with respect to Origo $(x, y, z) = (0, 0, 0)$, a spot usually reserved for the source, or at positions relative to each other. In McStas, it is the convention that the z -direction is the direction of neutron propagation, while the x -direction represents right-left and the y -direction up-down.

Other than the position and rotation, many components require additional parameters. The parameters vary with each component; for example, the simple `monochromator_flat`-component requires a width and a length of the monochromator crystal, a mosaicity in both the horizontal and vertical directions, a peak reflectivity r_0 , and the d -spacing or q -value of the crystal. More advanced components will often require more parameters, and the parameter settings can be changed to mimic the physical instrument. Changing the parameters can also be used for optimization, and McStas allows us to define parameters that can be changed upon the simulation start (setting parameters), thus making it possible to test many settings without changing the virtual instrument file[47].

For moving entire parts of an instrument, a component that does not affect the neutron known as `Arm` is used to define a new coordinate system. This is especially useful when several components need to move together, such as in the case of a TAS.

7.3 Ray-tracing and Monte Carlo in McStas

When performing a McStas simulation, N neutron rays are created one by one and propagated through the component list described above, this is known as ray-tracing. The more rays that are propagating to the final detector of the virtual instrument, the better the statistics. To improve the amount of rays that does that, each neutron ray is created with an unphysical parameter known as the weight factor p , plus nine parameters that corresponds to physical properties: position (x, y, z) , velocity (v_x, v_y, v_z) , and spin (s_x, s_y, s_z) .

For a simple simulated neutron source that emits neutrons uniformly in all directions, an enormous number of neutrons that are created fails to hit the small solid angle that defines the entry to the guide system. If we require a certain amount of neutrons to enter the guide, we must create a large number of additional but useless rays, at the cost of a lot of computational power. Another possibility is to make all the neutrons enter the guide, instead imposing a penalty upon them by decreasing their weight factor. If the entrance to the guide system takes up e.g. one tenth of the total solid angle, then all neutrons will hit this area but only count as one tenth of a neutron when reaching the detector.

This is one example of an *analytical* component, where the neutron parameters can be calculated deterministically and there is a certain probability of the ray continuing towards the detector. The weight factor π_j for such a component

should follow the weight transformation master equation[48]

$$P = f_{MC}\pi_j \quad (74)$$

where P is the probability of a real neutron being transmitted towards the detector in a given component, f_{MC} is a Monte Carlo choice value of how many simulated neutrons we allow to continue, and π_j is the weight factor of the component.

By setting $f_{MC} = 1$, all neutrons are allowed to continue towards the detector, and we multiply the original weight factor with the π_j in accordance with equation (74). This drastically decreases the number of neutron rays that needs to be simulated. This is so because all analytical components in the instrument get to reflect neutron rays that would otherwise have been killed off earlier in the instrument. These analytical components does not mean, however, that a neutron ray cannot be removed. If a neutron ray is propagating in a direction where it will not meet any components, it is killed and the total number of rays decreases, as we assume that it has hit the shielding.

The weight factor is updated for each neutron ray as it propagates through the instrument. For the final value, the weight factor is thus given as

$$p = p_n = p_0 \prod_{j=1}^N \pi_j \quad (75)$$

with p_0 the initial weight factor.

It is however not all components that can work purely in a deterministic fashion, and these are the *Monte Carlo choice* components. An example is a monochromator with a mosaicity. Here, the in-plane reflectivity is given deterministically, while the out-of-plane reflectivity is found by making an MC choice. After this, the neutron ray is propagated forwards with a correspondingly lower weight factor as we saw above.

When reading the results at the final detector one should keep in mind that the value of N has absolutely no physical meaning, but is just the number of neutron rays that the simulation got through the instrument. It is instead the average weight factors that gives us the performance of a real experiment we are trying to simulate as an intensity (neutrons hitting the detector per second). This is calculated as

$$I = \sum_i^N p_i = N\bar{p} \quad (76)$$

Comparing this situation to a real experiment, we would have the weight factor of each neutron hitting the detector of $p = 1$, and we get the correct result at fewer computations. The experimental variance is derived in the McStas manual as

$$\sigma^2(I) = \frac{N}{N-1} \left(\sum_i p_i^2 - \bar{p}^2 \right) \approx \sum_i p_i^2 \quad (77)$$

which for $p_i = 1$ would be N , giving an uncertainty of \sqrt{N} as expected.

A way of improving statistics is by using the SPLIT property in McStas. After an instrument section, such as the guide, where a lot of deterministic choices are

made, we can copy the neutrons and re-use them before they propagate into an MC choice component, since the many random choices within that component completely washes out the re-using of a few rays. This is saving computer power, since we can save ourselves many deterministic calculations. To get the correct result, we must of course demand that sufficiently many neutron rays have reached the SPLIT that they are properly randomized there.

7.4 Building the MultiFLEXX back-end

As a starting point, a McStas instrument describing the entire FLEXX instrument was used as a template. This McStas instrument was made in conjunction with the upgrade of the FLEXX physical instrument and was tested against the physical instrument in [15], where it was found that the McStas simulations were in very good agreement with the results of the actual experiments carried out to characterize the instrument after the upgrade. The McStas instrument was updated to work with McStas 2.0, in which several parameter names were streamlined at the cost of backwards compatibility.

The FLEXX front-end instrument was kept and everything after the monochromator-to-sample arm was removed. For transparency, the code for the MultiFLEXX back-end was written separately and later included at the end of the FLEXX McStas instrument using `%include "back-end"`.

It was decided only to make one set only of analyser and detector for simplicity, and changing the parameters of this setup to match the different energy channels. A sketch of analyser/detector setup can be seen in figure 15, along with the parameters that needs to be changed for the different energy channels. This does introduce an error source, as we don't simulate the 1 to 4 analyser crystals that might absorb neutrons before they hit energy channels 2 to 5. Research does show, however, that the absorption should be very low[27], and we ignore the contribution.

The first component in the back-end is a modified `Incoherent`-sample. This will work as the ordinary component, but with the added possibility of removing a specified amount of energy from every neutron that hits the sample. This is done to facilitate simulations of the inelastic resolution of the instrument, where we want to match a fixed E_i from the monochromator settings to the fixed E_f of the MultiFLEXX back-end. In terms of (\mathbf{Q}, ω) space, this amounts to moving the resolution function through a straight line at the removed energy, essentially making the sample dispersionless.

Next in figure 15, a distance L_3 from the sample, we find the analyser. L_3 varies from energy channel to energy channel as described in section 4, and is therefore a setting parameter that can be changed to represent any of the energy channels. The analysers were written in separate files, as several types were used and this allowed for a clearer picture, and they are rotated by A5 with respect to the incoming beam. Different analyser geometries were considered for each energy channel, one consisting of the `monochromator_curved`-component, others of three `monochromator_simple`-components placed individually. The analyser is moved by an arbitrary angle with respect to the beam impinging on the sample, in order only to measure the scattered neutrons and not the direct beam. In the real experiment, there will be 31 q -channels covering a range of 77° instead of only the one we use for testing here.

To conclude this McStas instrument, at an angle of A6 with respect to the

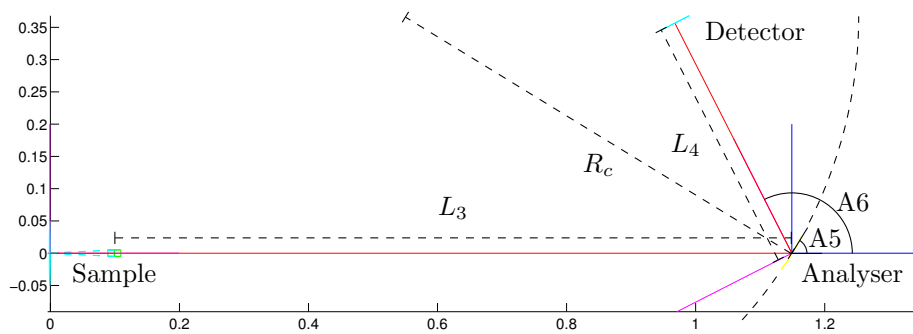


Figure 15: A graphic showing the MultiFLEXX back-end as McStas draws it. The annotations show the setting parameters needed to change from one energy channel into another.

incoming neutron beam a $2.50 \times 5 \text{ cm}^2$ 0D detector was placed, a distance of $L_4 = 40 \text{ cm}$ from the middle analyser crystal. Finally, a PSD monitor was placed immediately behind the analyser for beam shape analysis.

8 Simulation results

The simulations in this section were primarily performed on a 16-core cluster kindly made available by Peter Willendrup at DTU Risø. On this cluster, a single simulation that was to provide the final data with $N = 3 \cdot 10^8$ neutron rays took approximately 2 minutes. Many of the initial simulations were, however, done with a factor of 10 fewer neutrons when testing different setups and for preliminary results.

8.1 Simulating analyser curvature

The initial plan was for the MultiFLEXX was to employ a point-to-point focusing Rowland geometry as described in section 5.1 for the analysers. This should lead to a better resolution for the individual energy channels and a higher flux on the detector. Holders for analyser crystals, as described in section 4.1, had been designed early in the project and were already constructed to specifications given by the instrument designers.

Upon writing the instrument file to perform simulations, one of the first tasks was to model the Rowland geometry in McStas using the theoretical framework from [34] described in section 5.1. An algorithm that automatically calculated offsets and angles for the three analyser COMPONENTs used for each analyser was implemented in McStas, and the resulting output was compared to the specifications for the analyser holders, which were found to be significantly different. This discrepancy meant that old calculations were re-visited, and an unfortunate mis-calculation was found in the initial design plans.

A coordinate system error in the initial design of the analyser holders meant that the overlapping analyser crystals described in section 5.1 were overlapping in the direction of the incoming beam, rather than the scattered beam. This meant that the problem of having the upper analyser crystals shading the detector from the lower analyser crystals were not an issue as for the correctly designed Rowland geometry. Conversely, a large area of analyser crystal was now being shaded from the incoming beam, meaning that the effective area of the analysers were diminished, as can be seen in figure 16.

The decrease in effective area of the analyser was estimated from the effective height of the individual slabs of PG crystal summed versus the effective height of the actual analyser assembly. It was found that the effective analyser area was reduced by between 7% and 28%, a considerable amount.

Since the Rowland design was found to be problematic for the MultiFLEXX setup as explained in 5.2.2, and the design that was thought to be of the Rowland type was found not to be Rowland after all, it was decided to investigate the properties of the already-built analyser holders, the "anti-Rowland" (AR) design. The AR design was simulated by hardcoding the individual analyser crystal positions and tilt angles as found in figure 16 into McStas. To test if the curvature of the analyser was also affected by the calculation error, the AR analyser was modified to have the upper and lower analyser adjustable by adding and subtracting, respectively, small values to their initial angle, thus changing the curvature slightly.

To compare with the AR analyser, simulations were also performed with an ordinarily curved analyser geometry, as described in section 5.3, this being somewhat of a benchmark for neutron analysers. Here, the McStas component

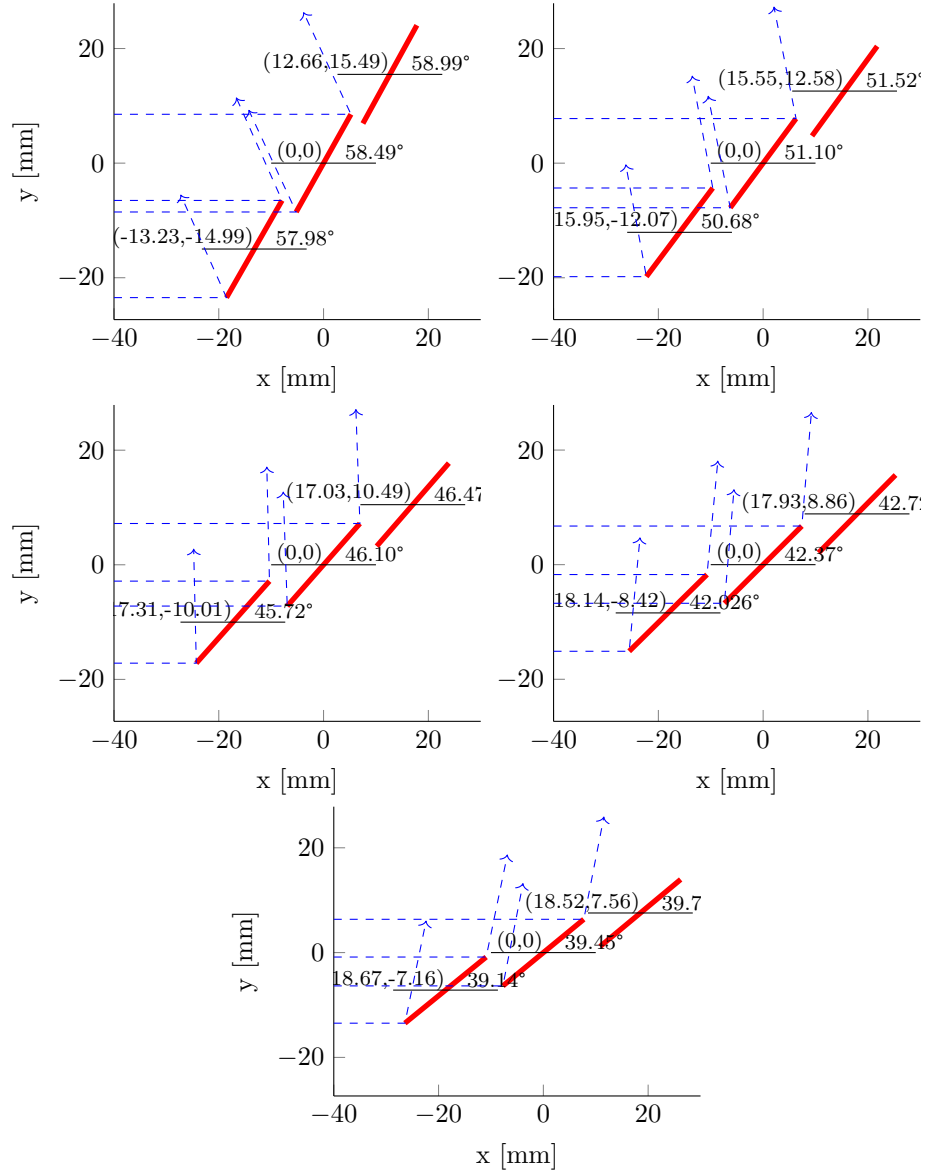


Figure 16: Positioning of the AR analyser crystals: (top left) 2.5 meV, (top right) 3.0 meV, (middle left) 3.5 meV, (middle right) 4.0 meV, and (bottom) 4.5 meV. Each analyser is plotted in its own coordinate system, i.e. the centre of the middle analyser is (0,0) but corresponds to the values for distances to sample given in section 4.1. The beam comes from the $-x$ direction. The shading of the analyser crystals is particularly noticeable for the high-energy analyser.

`monochromator_curved` was used, which has as a parameter the R_c of equation (64). Since we will be working with two types of analyser geometries at five different energies, we shall adopt the following convention for the remainder of this thesis.

- Data from the curved analysers is designated with a filled circle ●, lines relating to the curved analysers are designated by a solid line ———
- Data from the AR analysers is designated with an open circle ○, lines relating to the curved analysers are designated by a dashed line - - - - -
- The energy channel that we measure is coloured corresponding to its energy. ● = 2.5 meV, ● = 3.0 meV, ● = 3.5 meV, ● = 4.0 meV, and ● = 4.5 meV.

8.1.1 Elastic resolution simulations

To evaluate the elastic resolution of the analysers, scans over the monochromator angle, and hence the incoming energy, was performed, with the modified sample component working as an ordinary `incoherent`-sample. The resultant intensity profile on the detector-sized monitor in McStas was recorded, and the width (FWHM) and integrated intensity (sum of intensities) were calculated. The width was found both from the variance and from a Gaussian fit to the data points.

An example for a single elastic scan for the 2.5 meV energy channel is shown in figure 17 where we use the AR geometry of the designed analyser holders, along with a Gaussian fit to the data.

Instead of testing the AR analyser design against a curved analyser with the theoretical value of curvature found from equation (64), we opted to find the optimum curvature from our simulation results alone. It was deemed that the complexity of the problem was not described by the model in section 5.3. The optimisation was done by performing elastic scans like the one shown in figure 17 for the curved analyser design at different curvatures $\rho = \frac{1}{R_c}$. The optimisation was done for a sample in the shape of a rod of dimensions $h = 1 \text{ cm} \times r = 1 \text{ cm}$, and we shall see later that the sample height has an effect on the resolution.

In figure 18, the peak height (maximum detector value), integrated intensity (sum of detector values), and FWHM (from variance) can be seen for curvatures between $\rho = 0.25 \text{ m}^{-1}$ and $\rho = 5 \text{ m}^{-1}$ for the 2.5 meV energy channel. As in figure 17 we have also performed a Gaussian fit for each of these elastic scans, but we have chosen to plot the numerical results due to code robustness, as Gaussian fits to the data give erroneous results at extreme curvatures. Here, the elastic scan no longer has the characteristic bell shape of a Gaussian, but rather turns to three distinct peaks. The non-equal spacing between the different curvatures simulated have two causes: Curvatures further from the expected optimum were sampled coarser, and McStas takes as input $R_c = 1/\rho$ for curvatures, such that the spacing is equi-distant for the x -axis transformed to R_c .

As can be seen from figure 18, the peak in detector intensity coincides with the dip in width, while the integrated intensity has a sharp rise and a subsequent plateau as the width broadens and the peak height diminishes, the two effects cancelling each other out. We see that we lose no integrated intensity in choosing the curvature for which there is a peak in intensity and a dip in width, which

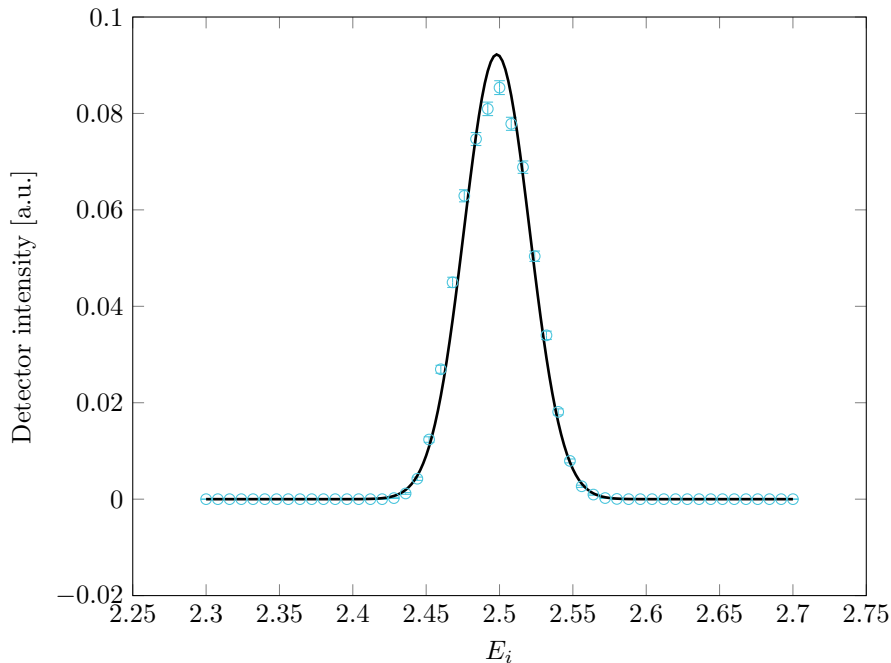


Figure 17: A single elastic scan over incoming energies close to the channel energy for a 2.5 meV energy channel in the anti-Rowland geometry of the designed holders. A Gaussian fit to the data is shown in red.

will however yield the best resolution. Picking the curvature value that gives us the largest peak is important, as a higher peak is easier to spot through the noise, the so-called signal-to-noise ratio. That the largest peak coincides with the smallest width is the optimal situation for us, and we will consequently use this curvature.

Comparing the elastic scan in 17 for the AR geometry analysers to the optimum found from scans over curvatures as in figure 18, we find that the curved analyser has a significant improvement, approximately 12%, over the AR analyser, as shown in figure 19.

By performing the simulations for different curvatures for all five energy channels, it was found that the curved analyser outperformed the AR analyser for them all. In table 3, the increase in peak intensity is listed for both the fit and the max value from the detector, along with the widths for the AR and curved analyser. As can be seen, the fitted peak intensity is higher in the curved analysers by 7.4% to 14.8%, with the increase being more prevalent for the higher energy channels. For the highest energy channels, we also see that the peak width increases, something we expected from the uncertainty on Bragg's Law in equation (54).

The widths are approximately the same for the two analyser types, with the curved analyser being slightly broader for some channels. The maximum increase in width for the curved analyser over the AR analyser is approximately 4%.

Also provided in the table is an estimate on the increase of effective analyser

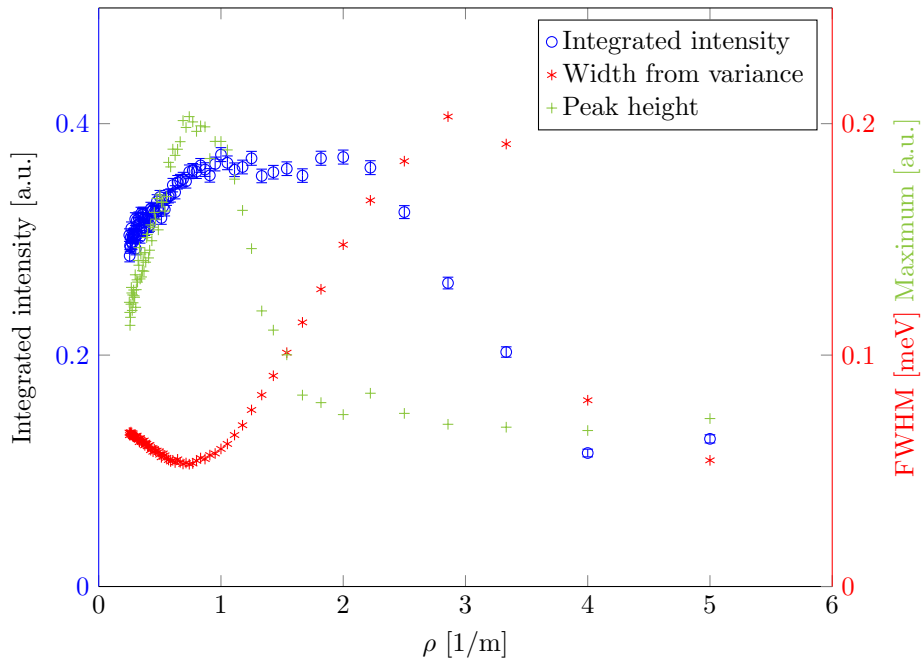


Figure 18: A range of simulations of the type in figure 17 that shows the effect of changing the curvature for the curved 2.5 meV energy channel. The peak intensity (green plus) normalised to the right axis has a peak at approximately $\rho = 0.75 \text{ m}^{-1}$. The width (FWHM) (red asterisks) has a dip at the same, while the integrated intensity (blue circles) rises before flattening out as the peak intensity decreases and the width increases. The similar scans for the remaining four energies can be found in appendix A.

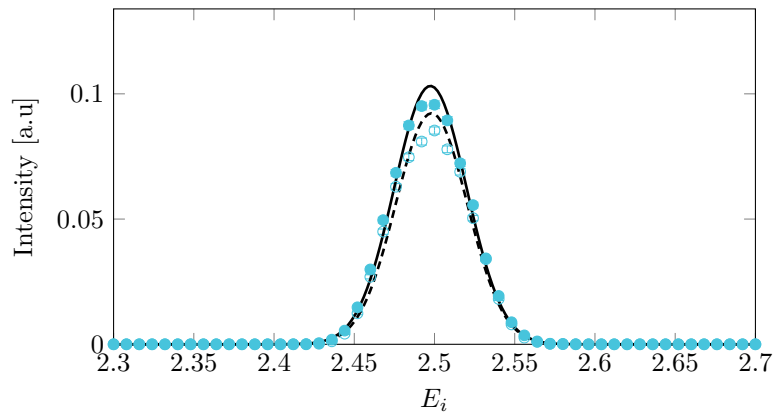


Figure 19: Comparison between elastic scans over a 2.5 meV energy channel with the two different analyser geometries. The curved (filled circles) analyser shows an approximately 12 % increase in peak intensity over the AR (open circles) one, with a peak width of $53.0(2) \mu\text{eV}$ versus $52.6(2) \mu\text{eV}$, i.e. no discernible peak broadening. The similar scans for the remaining four energies can be found in appendix B.

area in going from the AR geometry to the curved geometry, calculated from the effective height of the analyser. It is clear that we do not see an increase in peak intensity proportional to the increase in analyser area. The 2.5 meV analyser sees an increase in intensity by more than the increase in area size. However, the overall trend for increase in peak intensity and increase in analyser area agrees, with the highest energy channels seeing the largest improvement.

Energy channel	2.5 meV	3.0 meV	3.5 meV	4.0 meV	4.5 meV
Increase (fit) [%]	11.8(8)	7.4(6)	7.6(5)	11.9(4)	14.8(4)
Increase (max.) [%]	12.1(18)	11.6(16)	8.6(14)	14.5(14)	16.2(14)
Width (cur.) [μeV]	53.0(2)	78.6(2)	103.1(2)	128.3(3)	158.3(3)
Width (AR) [μeV]	52.6(2)	74.9(2)	99.8(3)	128.4(3)	160.3(3)
Increase (area) [%]	7.6	16.1	23.8	31.5	39.0

Table 3: Intensity improvement from the optimally curved analyser over the AR analyser measured by both fitting a Gaussian peak to the data and by directly comparing the maximum detector value, where it is found that the increase lies in the range 7.4 % to 14.8 % for the fitted peak heights. The widths of the fits to the two types of analyser is also compared. The last column shows the estimated increase in analyser area for the curved over the AR analyser.

8.1.2 Inelastic resolution simulations

In its day-to-day operation, the MultiFLEXX will only be performing inelastic measurements. The broadened resolution from the FLEXX front-end at higher E_i 's will affect the final resolution as described in 6.1, and we have therefore repeated the optimisation from section 8.1.1 in an inelastic setting.

To evaluate the inelastic resolution of the analysers, the monochromator angle was kept fixed at an incoming energy of 5.0 meV. The modified sample component was set to downscatter the neutrons, i.e. remove a fixed amount of energy from each incoming neutron. As an example, the 2.5 meV energy channel was tested at $E_i = 5.0$ meV by changing the downscattering energy from 2.3 meV to 2.7 meV. Since our sample is dispersionless, there are no resolution ellipsoids as described in 6.1.1 that will have better or worse focusing. An example for the 2.5 meV channel is shown in figure 20 where we, as in the previous section, show the result of the AR geometry of the designed analyser holders along with a Gaussian fit to the data. The scans over different curvatures for the different energies can be found in appendix C.

For the curved analyser, it was found that an optimum curvature existed where the peak intensity was at its highest and the width was at its lowest, and that this optimum curvature performed better than the AR analyser. Comparisons between the optimally curved and the AR analyser in the inelastic case can be found in appendix D. We have compiled our results into table 4. Here, we find that the inelastic resolutions show similar improvements as the ones we found from the elastic resolutions with an increase in the range 8.0% to 15.7%, and that there is a broadening in the low-energy channels due to the broader resolution from the FLEXX front-end at this higher energy. The lack of broadening for the high-energy channels can be attributed to the fact that E_i and

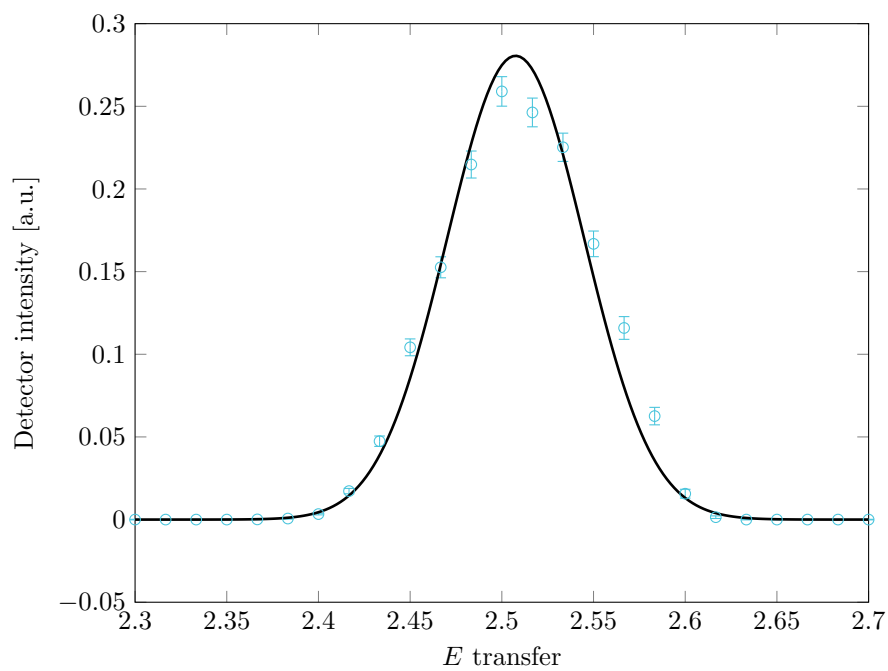


Figure 20: A single inelastic scan where the sample removes between 2.3 meV and 2.7 meV from the incoming neutrons of energy 5.0 meV such that the 2.5 meV energy channel can be investigated. This scan is for an AR analyser, i.e. in the geometry of the designed holders. A Gaussian fit to the data are shown in red.

E_f are almost equal here, such that the analyser and monochromator has similar broadenings from equation (54). For an experiment at $E_i = 10$ meV, the monochromator energy width will again dominate.

Energy channel	2.5 meV	3.0 meV	3.5 meV	4.0 meV	4.5 meV
Increase (fit) [%]	12.7(6)	8.0(5)	8.9(4)	11.4(4)	15.7(4)
Increase (max.) [%]	10.2(19)	8.9(16)	6.4(14)	11.3(14)	15.8(14)
Width (cur.) [μ eV]	89.4(2)	105.3(2)	122.4(3)	141.3(3)	163.8(3)
Width (AR) [μ eV]	88.6(2)	103.0(3)	120.1(3)	141.2(3)	166.1(3)

Table 4: Intensity improvement from the optimally curved analyser over the AR analyser measured by both fitting a Gaussian peak to the data and by directly comparing the maximum detector value, where it is found that the increase lies in the range 8.0% to 15.7% for the fitted peak heights. The widths of the fits to the two types of analyser is also compared.

8.1.3 Designing new analysers

Due to the sub-optimal performance of the analysers it was decided to construct new analyser holders of the curved analyser kind, as an increase in peak intensity of between 7.4% and 15.7% is worth going for in the intensity-limited field of neutron scattering.

In choosing the final curvature for the new analysers, the optimal curvatures for both elastic simulations as performed in section 8.1.1 and inelastic simulations as performed in section 8.1.2 were taken into account, with a slight preference towards the optimal inelastic curvature, seeing as this is the mode in which the MultiFLEXX will be employed. The optimal curvatures found from simulations and the chosen curvatures for the new analysers are listed in table 5. Although the difference between the optima for the elastic and the inelastic resolutions might seem large, there is little difference in peak intensities and FWHM over these values.

Energy channel	2.5 meV	3.0 meV	3.5 meV	4.0 meV	4.5 meV
Elas. optimum [m^{-1}]	0.741	0.667	0.476	0.417	0.303
Inelas. optimum [m^{-1}]	0.769	0.513	0.476	0.408	0.385
Chosen [m^{-1}]	0.755	0.600	0.500	0.410	0.370

Table 5: The optimal curvatures as found from the scans in sections 8.1.1 and 8.1.2, along the curvature chosen for the new analysers.

To create the blueprints for the new curved analysers, the code defining the individual analyser crystal positions and angles from McStas was recreated in MATLAB, allowing for plotting. Sketches of the new curved analysers are seen in figure 21, along with their individual positions and angles. As can be seen, the shading is now gone, increasing the effective analyser area.

To see the combined energies covered by our array of analysers, we have combined five high-statistics simulations, one for each energy channel, with the

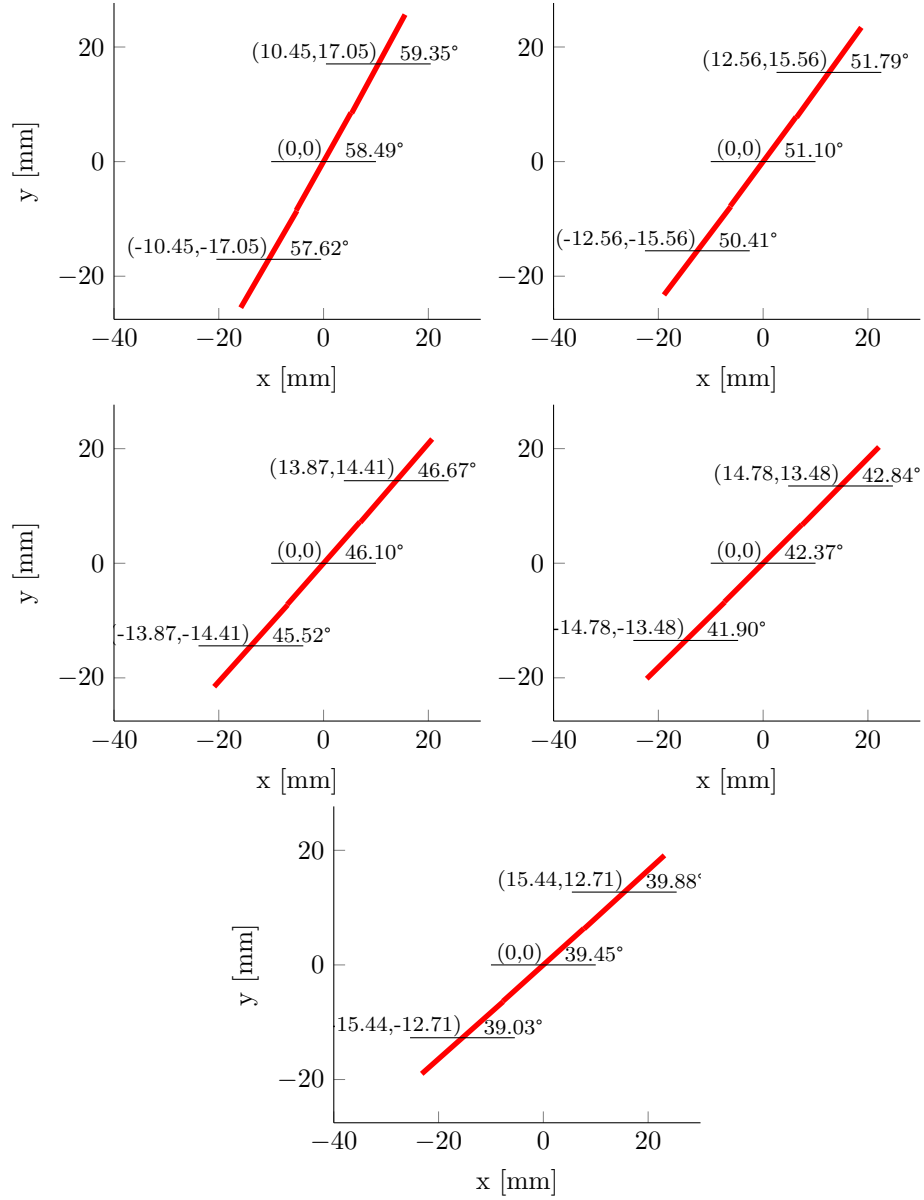


Figure 21: The analyser crystal geometries settled upon after simulations were done: (top left) 2.5 meV, (top right) 3.0 meV, (middle left) 3.5 meV, (middle right) 4.0 meV, and (bottom) 4.5 meV. Each analyser is plotted in its own coordinate system, i.e. the centre of the middle analyser is (0, 0). The shading is now gone.

analyser curvatures as those chosen in table 5. The result can be seen in figure 22, and the simulations are inelastic as described in section 8.1.2 with an incoming energy of $E_i = 5.0$ meV. This means that the peak furthest to the left at an energy transfer of 0.5 meV corresponds to the 4.5 meV channel. A similar plot, but for $E_i = 10$ meV, is shown in figure 23. Here, the broadening from the monochromator becomes so large that we see the spectrums from each individual energy channel can overlap. This is not a large problem in terms of the analysers, as they will still accept approximately the same range of energies as we saw before. We have, however, a large uncertainty on E_i .

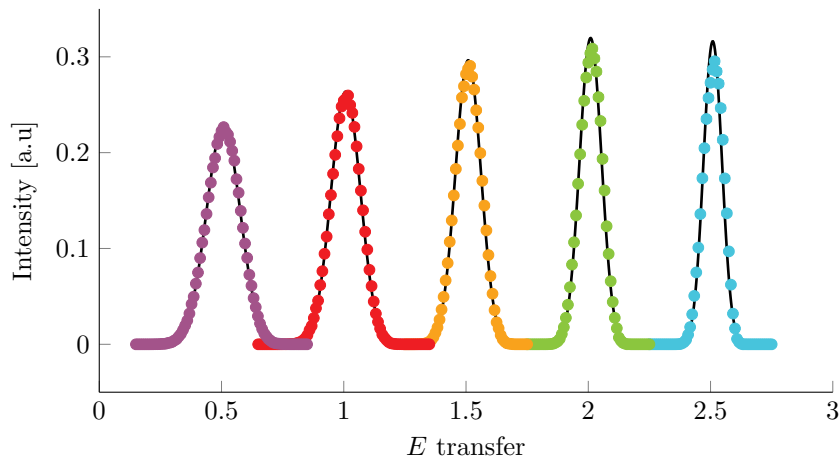


Figure 22: A plot combining the simulated resolutions in the inelastic setting at $E_i = 5.0$ meV. The lowest energy channels have the highest peak intensity and the lowest FWHM, as expected. Data from the curved (AR) analysers are labeled by solid (open) symbols and connected by solid (dashed) lines. The 2.5, 3.0, 3.5, 4.0, 4.5 meV channels are colour coded by $\color{cyan}\bullet$, $\color{green}\bullet$, $\color{orange}\bullet$, $\color{red}\bullet$, and $\color{purple}\bullet$, respectively.

8.2 Simulating sample size

As discussed in section 5, the analytical methods for treating a point source and a parallel source of neutron radiation are different. We have so far approximated the sample, which is the source of neutrons hitting the analyser, to a point source due to its small vertical size (typical samples are approximately 1 cm in height) compared to the distance to the analyser of at least 1.05 m. We are, however, still interested in the effect of the sample height on the resolution. We have therefore simulated this, starting from a rod of radius 0.5 cm and height 0.5 cm, going up to a height of 8 cm. The results in the elastic case can be seen for the 2.5 meV energy channel with the curved analyser in figure 24. They clearly show that while the peak intensity increases with sample height due to the greater amount of sample to be hit by – and hence scatter – neutrons, the increase levels out at a height of 4 cm. This can be explained by the beam profile at the sample position, where the beam is approximately 8 cm tall, with the lower half hitting below the sample which has its bottom fixed in the middle of the beam.

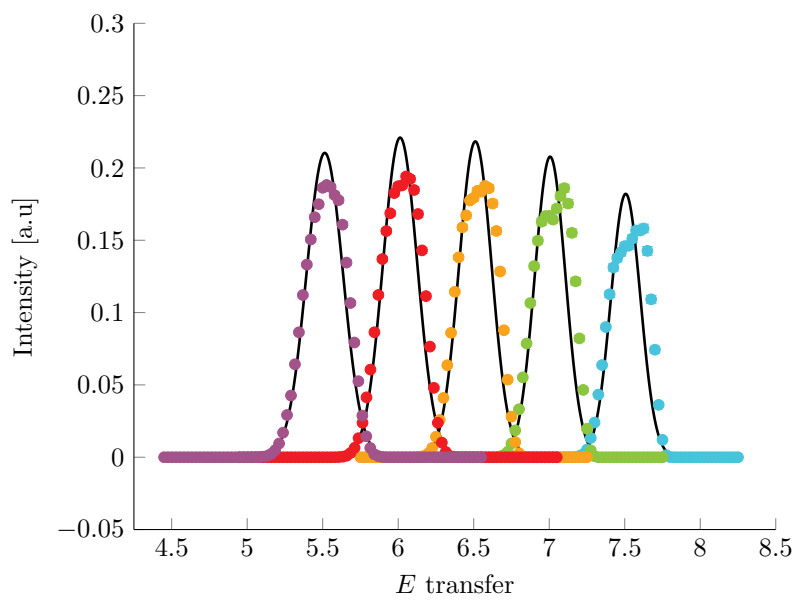


Figure 23: A plot combining the simulated resolutions in the inelastic setting at $E_i = 5.0$ meV. The lowest energy channels have the highest peak intensity and the lowest FWHM, as expected. Data from the curved (AR) analysers are labeled by solid (open) symbols and connected by solid (dashed) lines. The 2.5, 3.0, 3.5, 4.0, 4.5 meV channels are colour coded by ●, ●, ●, ●, and ●, respectively.

From symmetry considerations, the results for this simulation corresponds to the results for a sample of double height, but centered in the beam.

While the peak intensity increases, so does the width of the peak, showing that an increase in sample height leads to poorer energy resolution, with the width approximately doubling as the sample goes from 0.5 cm to 5 cm. Had the typical sample size been larger, the final curvatures for the analysers might have been different to accomodate this effect. The broader peaks can be attributed to the fact that the taller samples increases the divergence of neutrons hitting the analyser. This introduces a larger uncertainty in the determination of $2\theta_A$, the analyser scattering angle.

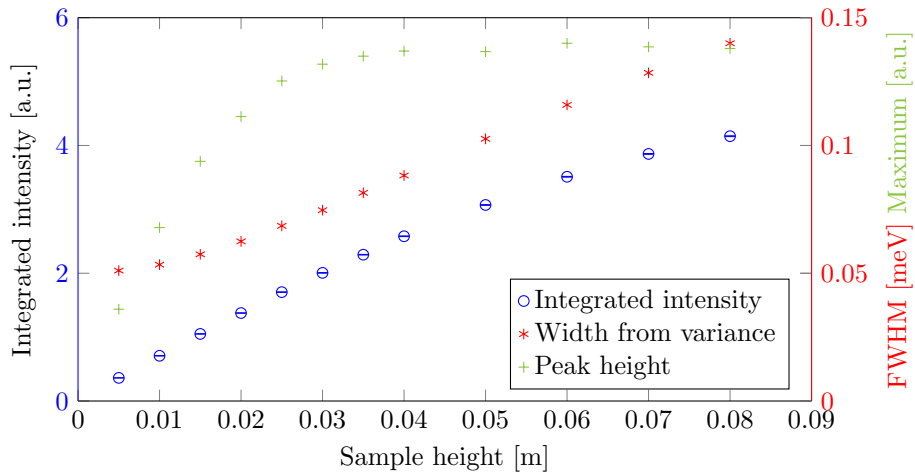


Figure 24: A range of simulations showing the effect of increasing the height of the sample on the resolution for the curved 2.5 meV channel. The peak intensity (green plus) normalised to the right axis increases as a larger volume of sample is hit by neutrons, until the sample height exceeds the beam size at sample position. The width (red asterisks) increases with sample height due to the increased uncertainty in determining $2\theta_A$. The integrated intensity (blue circles) increases continually, as both width and peak intensity increases.

The effect of the sample height is a broadening and for large sample sizes, this will mean an overlap for some energy transfers. In this case, the broadening is due to the sample and analysers in conjunction, and not just monochromator broadening. This means that we should try to avoid it.

In plotting the individual elastic scans next to each other, we see that the overlapping begins at a sample height of approximately 3 cm. Correcting for the centering described above, it is estimated that for elastic scattering, samples with heights up to 6 cm can be measured in the MultiFLEXX without problems.

8.3 Lessons from simulations

By performing our simulations, we learned that the AR analyser geometry was inferior to the simpler curved analyser geometry. Since an improvement in the 8% to 15% range as we saw from simulations can significantly improve the usability of the MultiFLEXX, it was decided to exchange the analyser holders.

The new curved analyser holders will be designed with a curve that has been found through McStas optimisations for elastically and inelastically scattering neutrons.

Furthermore, we simulated a change of sample size, where we found that an increase in sample size would result in poorer resolution.

9 Prototype setup

To evaluate the performance of the MultiFLEXX, a prototype test was performed. Due to the neutron source BER-II at HZB being out of operation the entire year prior to the commissioning of the MultiFLEXX, this prototype test was performed at the Forschungs-Neutronquelle München II (FRM-II) at the Technische Universität München, where the PANDA[49] TAS front-end served as a stand-in for the FLEXX TAS front-end. The test was performed at PANDA since an optional multiplexing back-end that shares the idea behind the MultiFLEXX (named BAMBUS) is in the development phase there. Also PANDA, as FLEXX, features a doubly focusing monochromator.

The aims of the test are to determine what the instrument resolution will be, and to investigate the influence of the front-end and sample parameters on the measured data. Furthermore, the tests may provide a head start to the post-commissioning search for background reduction. Due to the rather late time in the construction that this experiment is being performed at, any larger changes to the design are unlikely to be implemented, as parts for the MultiFLEXX are already delivered and ready for final assembly at HZB. However, lessons learned from the design of the MultiFLEXX may be used for optimisation of the proposed BAMBUS, such that any inherent design flaws or minor inconveniences can be corrected early in the process.

For the test, a frame that emulates the final assembly of the MultiFLEXX with two neighbouring q -channels is used. The frame consists of an aluminium top and bottom and borated plastic sides. The two q -channels are separated by a wedge of borated plastic to create the correct angling between two q -channels and add further shielding. One side wall consists of another such wedge, while the other side wall is just a thick slab of borated plastic. This means that one q -channel is better shielded than the other as the low energy channels are only covered by the thin edge of the wedge.

Using two channels, it will be possible to test if there is any *crosstalk* where a strong signal in one q -channel leaks into the neighbouring q -channels. Furthermore, the two channels allows us to compare the performance of the AR and the curved analysers that has been built for the MultiFLEXX to test if the signal improvements shown in McStas simulations are experimentally reproducible.

We used two standard samples in neutron scattering for our experiments

- A vanadium (V) rod of $d = 0.6$ cm which had its length controlled by a covering piece of Cd, limiting its height to $h = 1$ cm. Vanadium is a strong incoherent elastic scatterer and emits most of the neutrons scattered from it isotropically in 4π , which means that it creates a lot of background, especially on the parts of the instrument facing the sample.
- A lead (Pb) single crystal of size 1 cm \times 1 cm \times 1 cm. Lead is used as a standard sample in neutron scattering, due to its simple cubic crystallographic structure. The heavy atoms of lead means that the phonons have low energies, and can be measured at room temperature.

9.1 Experimental setup

Before the prototype was transported to FRM-II, an initial setup was performed at HZB. Here, the analyser crystal holders were correctly aligned such that

the middle analyser crystal was exactly in the Bragg condition for the energy channel in question. Furthermore, experiments were performed to establish which detector threshold values should be used. In this section, we shall briefly discuss this setup process. Since the MultiFLEXX is designed to be an option for users of the ordinary FLEXX, the process of exchanging an ordinary TAS back-end for the MultiFLEXX is also described here.

9.1.1 Aligning analyser holders

The analyser holders are designed to place the analyser crystals at the positions and relative angles shown in figures 21 and 16 for the curved and AR geometry, respectively, but the absolute angle with respect to the incoming beam is not fixed. To ensure that the central analyser crystal is exactly in the Bragg angle for the relevant energy channel, the entire analyser mount can be rotated around its centre where it is connected to the cassettes. A picture of four analyser holders mounted with analyser crystals are seen in figure 25.

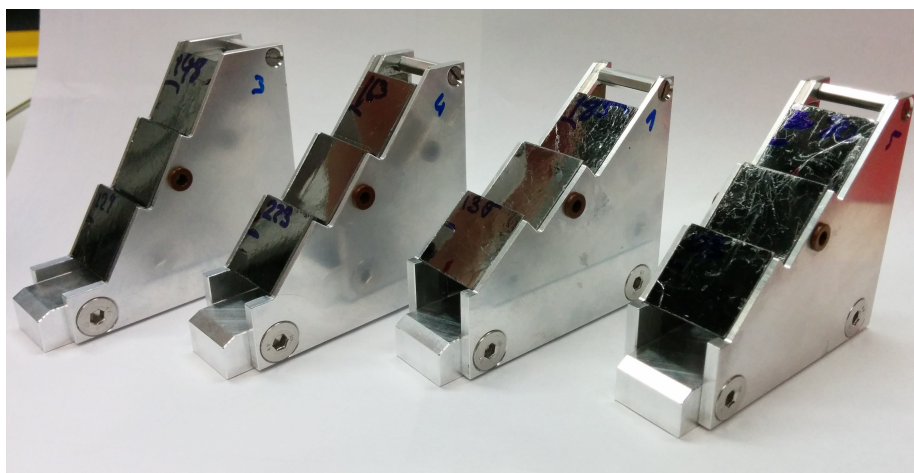


Figure 25: Four analyser holders in the AR geometry, with analyser crystals inserted for testing. The brown bushing in the side is the fastening point and the axis around which we rotate to align.

For the alignment of the analyser holders relative to the neutron beam, a laser beam was used. This was set up to be completely level and in the same height as a divergence-free neutron, such that the laser beam hits exactly in the middle of the central analyser crystal. The PG crystals have a protective reflecting aluminium coating that the laser beam will be reflected by, and since both the laser beam scattering from the coating and the neutron being Bragg scattered inside the crystal have identical incidence and reflective angles, an analyser crystal aligned with a laser beam is also aligned for neutrons.

The correct alignment of the analyser crystal with the laser light was done by removing the detector tubes and top shielding from the cassette, leaving the laser beam to shine through the top of the cassette. An aluminium rail was inserted at the top of the cassette, in which five oblong holes were cut. In the middle of the oblong holes, a groove marked the centrum where a correctly aligned analyser

holder would reflect the laser beam to. Alignment was then a matter of turning adjustment screws to rotate the holder, until the beam was aligned with the groove in the rail. We estimate that this method gave us the possibility to align the central analyser crystal to within 0.1° of the desired angle.

Due to the overlapping analyser crystals on the AR analyser, as described in section 8.1, the laser beam hit the edge of the lower analyser, producing a diffuse beam that made alignment impossible. To compensate for this, the laser was shifted 3 mm upwards to clear the lower analyser. This also meant that the grooves in the rail were not at the correct position. Marks were made on the rail, shifted by the same 3 mm, to which the AR analyser could be aligned to. This alignment problem was only present for the AR analysers, and did not affect the curved analyser holders that will be used for the finished MultiFLEXX.

Since we would like compare the curved and the AR analysers, one cassette was prepared with each of the analyser types.

9.1.2 Detector setup

As described in section 2.4.2, nuclei with a high absorption cross section are used to detect neutrons. The most commonly used detector materials is ^3He , which undergoes the nuclear reaction



i.e. produces tritium ^3H and proton ^1H along with a release of energy Q when hit by a neutron. By mixing ^3He gas with argon (Ar) gas, the ions released upon neutron absorption are accelerated by an applied high voltage along the length of the detector. The accelerated ions produce more ions from collisions with the Ar gas in a cascade, increasing the signal that will be detected by the anode as a current. Background ionisation events may also occur, such that α , β , and γ radiation may be detected as well, but these events will make a different type of cascade, and their signals should be distinguishable. γ radiation is the most likely source of background, as its penetrative power is much higher than for α and β radiation and it is produced in many places around the instrument as a by-product of the neutron absorbing shielding used to reduce background neutrons.

The amount of ^3He in the detector tube determines the efficiency of the detector, but lower energy neutrons are more readily absorbed as evident from equation (28) for the absorption cross section. To even out the efficiencies of the detectors over the 2 meV range that we measure over, the detectors for each detected energy has a different amount of ^3He in them such that there are five types of detectors. Thus, we should be able to save expensive ^3He .

Since both neutrons and γ radiation will be detected by the detector, it is important to discriminate between the two. Therefore, an experiment was performed at HZB to determine the threshold values for detecting a neutron.

A radium-beryllium (Ra-Be) source[2] was used to generate neutrons leaving the source isotropically in 4π , with an activity in the GBq range. Since the ^3He detectors are more effective at detecting thermalized neutrons, the source was placed in the middle of a circular block of plastic to thermally moderate the neutrons, with ten neutron detectors, two of each type, placed in holes along the perimeter of the plastic block. The spectrum for the Ra-Be source was then measured by the ten detectors for a fixed time.

To determine the signal from γ radiation, a metal sheet of neutron-absorbing Cd was wrapped around the Be source. The sheet of Cd produced additional γ radiation due to its absorption of neutrons, and upon comparison between the normalized spectra from the measurement with and without the Cd sheet in place, it was possible to attribute a part of the detector spectrum to the γ radiation. The comparison between the two measurements for a single detector tube can be seen in figure 26.

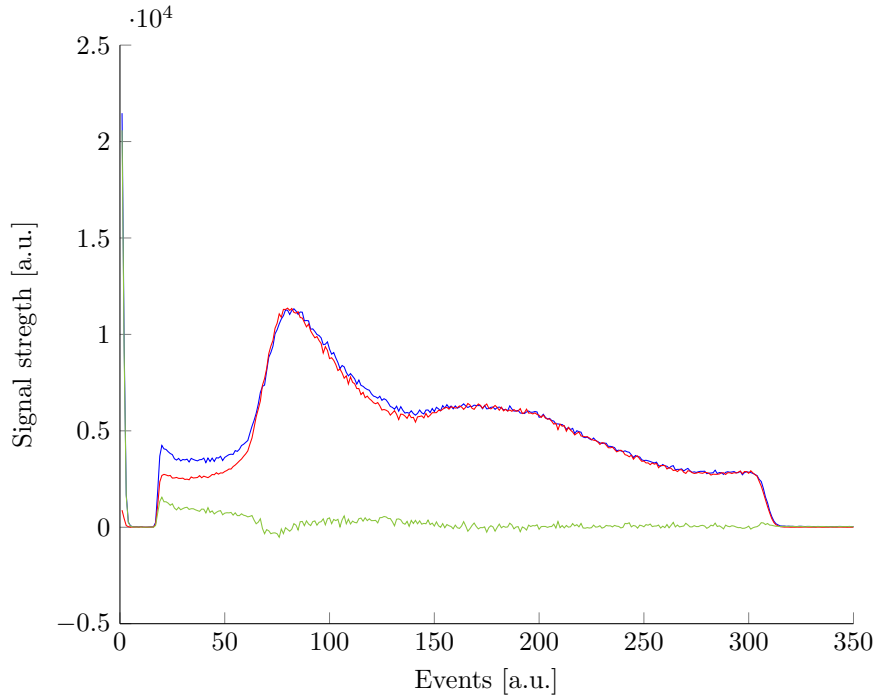


Figure 26: Comparison of spectra coming from a moderated Be source as measured by a single detector. In red the un-shielded source, in blue the Cd shielded source, and in green the difference between the two signals. The difference is primarily seen for events below 75, although the two spectra are not equal until events above 150, which on the other hand will mean that a lot of neutron signal will be lost.

The figure shows that the two contributions from γ radiation and neutrons are very close, and in order to completely discriminate against γ radiation, the threshold needs to be set relatively high. Normally the two spectra should be better separated, but a technical detail in the ways the detectors and their electronics are configured means that the signal is compressed, making it difficult to set a threshold that does not sacrifice too many neutrons in an attempt to keep the γ background counts low. In section 10.1, we will show the effect of changing the threshold in a realistic experimental setup, performed during the PANDA prototype experiments.

9.1.3 Ra-Be source experiments

Preliminary experiments with the thermal Ra-Be neutron source from above placed in front of the prototype, with analysers and detectors fitted, showed a significant amount of counts in the 2.5 meV channel with this number decreasing to approximately a third as the energy for the analysers increased. Since we are trying to detect cold neutrons from the tail of a Maxwellian spectrum moderated at room temperature, there will be very few neutrons at the lowest energies, which goes against what we measured. Therefore, we must assume that the Ra-Be source was undermoderated and much of the signal that we see comes from fast neutrons not being stopped by the shielding facing the source, or are converted to γ radiation which penetrates the borated plastic easily.

There was, compared to its neighbours, a very low count rate for the 3.0 meV AR channel, leaving us to suspect that an analyser crystal may have fallen out of the holder, giving a smaller analyser area and hence fewer counts.

The background count rates in the test described above were quite high, which meant that additional blocks of borated plastic shielding were prepared to increase shielding of the prototype if the experiments at PANDA revealed that the background was high. Furthermore, a Be filter was also requested for.

Since the MultiFLEXX will be operating with cold neutrons, which according to equation 28 are easier absorbed by the borated plastic shielding, this test with thermal neutrons cannot stand alone as a measurement of background from the finished instrument. This is why a prototype experiment in an environment similar to the one under which it will operate, such as we have on PANDA, is important to perform.

9.1.4 Setting up for PANDA

Before dismounting the ordinary PANDA back-end, we aligned the instrument to a Bragg peak of a lead sample at an energy of $E_i = 4.5$ meV. Keeping this sample in place allows us to set the absolute value for the scattering angle after we have exchanged the PANDA back-end for the MultiFLEXX prototype.

Since the finished MultiFLEXX will employ the curved geometry analysers, the q -channel with this type of analyser was placed in the better shielded of the two positions in the frame, while the AR geometry analysers were placed in the poorer shielded position. The complete prototype was then hoisted onto a table made from aluminium profiles. The table could be lifted using air pads, such that the motors controlling the instrument A4 angle had the possibility to move the table across the Tanzboden. The experiment table was slid onto an arm of the PANDA instrument normally holding the analyser and detector and fastened with clamps and wedges, such that the distance from the sample position to the analysers emulated that of the MultiFLEXX when finished. For the finished MultiFLEXX detector, a similar arrangement will move the finished instrument instead of just 2 out of the 31 q -channels.

The necessary electronics for detector control was pre-assembled at HZB and were stowed on a shelf under the experiment table, such that unnecessarily long cables to the detectors could be avoided and only a power cable and ethernet cable for transmission of data were following the table around.

With the MultiFLEXX prototype mounted as seen in figure 27, it became apparent that the ordinary PANDA back-end that had been moved to the side

constricted the movement of the setup, since cables prevented it from being moved further away. This meant that the monochromator angle A_2 for PANDA could not be turned further down than to the value corresponding to 2.5 meV, limiting our possibilities for E_i 's.



Figure 27: The MultiFLEXX prototype (grey rectangle upper right), mounted in the back-end position of the PANDA TAS via an aluminium tube (bottom center). Behind the metal plate (lower right) is the detector electronics. Left, we have the sample position and translation tables/tilt stages for the sample, along with the beam stop. The large green/blue/green cylinder in the background houses the monochromator.

After the mounting of the prototype to the PANDA analyser arm, we did an A_4 scan with the lead sample, in the range where we knew the Bragg peak to be. One peak from each of the 4.5 meV channels were detected, at the expected separation of 2.5° , but with a highly different count rate (2800 to 800) in favor of the AR analysers. A second scan of A_4 , but in the opposite direction, was performed to test for consistency in the A_4 angle. The two scans are seen in figure 28, where we find that the two Bragg peaks have a reproduceable center, indicating that the clamps and wedges were holding the arm tightly.

The large difference between the two channels was found to be an effect of the prototype not being correctly centered on the experiment table, such that the line of sight between the sample and analysers was broken. The prototype was centered on the table, after which both channels yielded approximately similar count rates, as the similar scan in figure 33 shows.

The software controlling PANDA had been modified to accommodate the 10 (instead of 1) detector counts that the prototype produces. The detectors counts

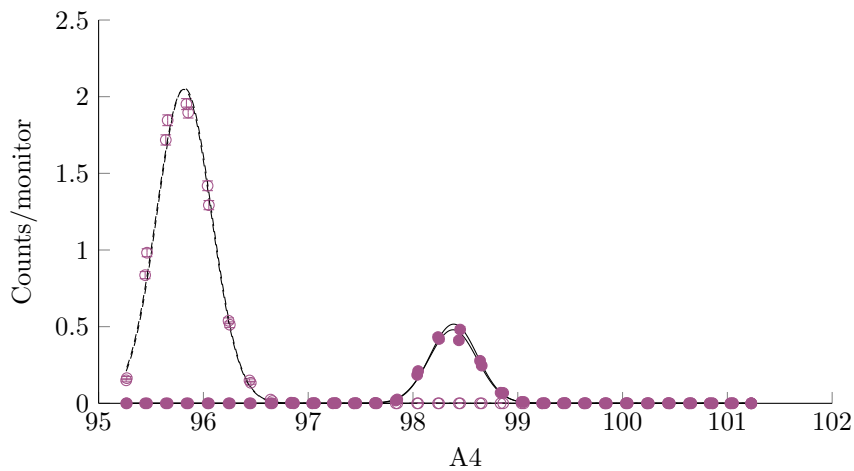


Figure 28: Data from the two 4.5 meV channels during two A4 scans, one in each direction. There are two peaks at 95.8° and two peaks at 98.4° , they are almost indistinguishable, as are the Gaussian fits (black) to the peaks. The large difference in count rate of the peak at 95.8° and the peak at 98.4° suggest that the prototype is misaligned on the table.

were plotted against a scan value as soon as a measuring point was completed, allowing the instrument users to follow the progress of the experiment in real-time. The detectors were numbered 1 to 10, with the even numbers representing the curved type analyser, and the odd numbers representing the AR type analysers. Low numbers have lower energy, such that the detectors 1 and 2 are representing the pair of 2.5 meV energy channels with the AR and curved analysers, respectively. A sketch showing the individual detector numbers is shown in figure 29.

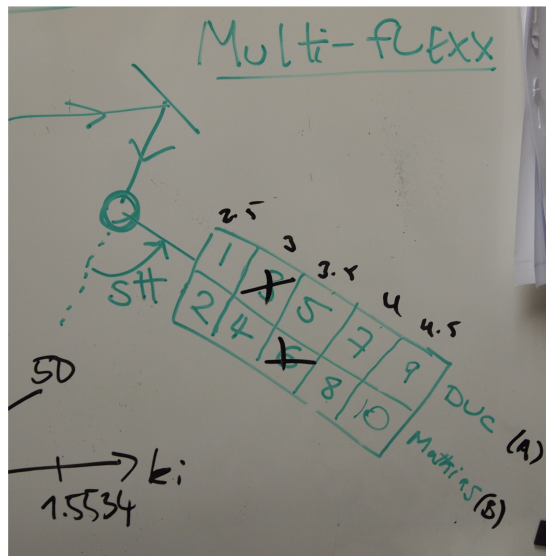


Figure 29: Sketch showing the conversion from detector number to detector energy and analyser type, as photographed from the whiteboard of the experimental hut. Black crosses indicate channels that we suspect are malfunctioning, as described in 9.1.3 and 10.2.

10 Prototype experiments

10.1 Threshold tests

To measure the effect of changing the threshold as described in section 9.1.2, we performed a count of events in the 4.5 meV channel at different threshold settings and compared them to the background. The incoherent scattering of the V sample was counted for 2 min with $E_i = 4.5$ meV at each threshold value in the range 60-120. To compare to background, we changed to $E_i = 3.5$ meV and repeated the count. At $E_i = 3.5$ meV, the primary source of background should be γ radiation that penetrates the borated plastic of the MultiFLEXX. Due to the expected lack of intensity in the 4.5 meV channel at $E_i = 3.5$ meV, we raised the count time to 10 min per threshold setting to obtain adequate data for statistics. The results of this measurement can be seen in table 6.

There are several interesting things to notice from table 6. Firstly, the difference in intensity we expect to find due to the curved analyser performing better than the AR one disappears when increasing the threshold, such that for the threshold set at 90 and above, the two q -channels have approximately the same intensity.

From the numbers presented in the table, we can calculate the Signal-to-Noise Ratio (SNR) at each threshold setting. This is done in figure 30 where one can see how the SNR increases as the threshold increases. This seems to suggest that we get a signal from γ radiation even at the higher threshold settings and since the curve does not seem to break, we might even get a further decrease in background upon further increasing the threshold. We are, however, already losing 80% of the signal between the highest and the lowest tested threshold

Threshold	Signal / 2 min		Background / 10 min	
	anti-Rowland	Curved	anti-Rowland	Curved
60	1350	1510	127	111
75	980	1130	76	73
90	765	785	58	38
105	480	520	41 (34*)	23 (28*)
120	290	300	13*	12*

Table 6: The detector counts per 2 minutes for signal and per 10 minutes for background, with respect to detector threshold. Threshold values can be compared to figure 26. Starred numbers (*) are counted after the addition of more shielding on the poorly shielded side of the prototype.

setting, so any further increases will severely limit the usability of the finished instrument.

A better solution will be to fix the issues with the detector electronics as mentioned in 9.1.2, such that the γ radiation and neutron radiation becomes less overlapping, and the detector responsible personnel at HZB is hard at work in this task.

10.2 Elastic resolution and intensity improvements

After performance analysis of the analyser geometry in McStas, we conducted a range of experiments to see if the simulated improvements in intensity were also experimentally reproducible.

To measure the elastic resolution, we will use the incoherent V sample. The incoherent nature of V means that we can simultaneously measure the resolution of the two q -channels in our prototype. This also means that the A4 setting of the instrument is unimportant as long as we are not measuring the direct beam. For the elastic tests, we set $A4 = 90^\circ$.

To measure the elastic energy resolution, a scan was performed over the incoming energy by changing the monochromator angles A1 and A2, scanning slightly to each side of the energies that our energy channels are constructed for. We used the doubly focusing monochromator of PANDA, since this is the mode in which the MultiFLEXX will be used at FLEXX. Due to the geometrical constraints described in section 9.1.4, the 2.5 meV channels have only been scanned to one side.

The resulting counts per monitor versus E_i plot can be seen in figure 31, where the energies over which we scanned has been laid out end-to-end, although the scans were performed as 10 points to either side of one of the analyser energies.

The resulting energy widths and intensity improvements, as found by performing Gaussian fits to the peaks shown in figure 31, are tabulated in table 7 alongside the simulated energy widths and intensity improvements found in table 3. We cannot compare absolute intensities from McStas and the experiments, but we can still compare the relative improvements from the AR analysers to the curved analysers.

As already noted in 9.1.3, the AR 3.0 meV channel severely underperforms.

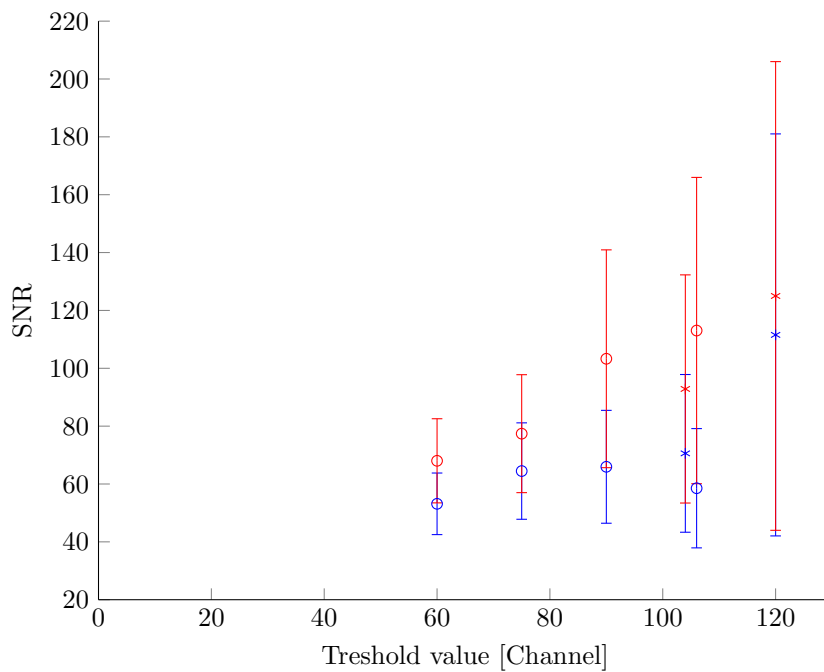


Figure 30: The SNR in the 4.5 meV channels as a function of detector threshold values. Red is the curved analysers and blue the anti-Rowland analysers. The starred numbers in table 6 are represented by stars (*) instead of circles in the figure. At threshold 105 where we have measured both with and without extra shielding, the data points have been moved slightly apart to avoid clutter.

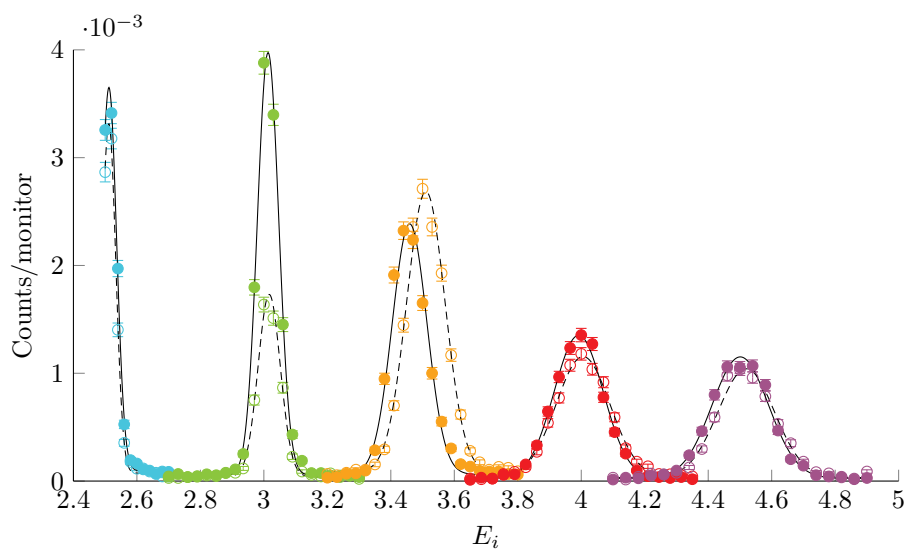


Figure 31: Elastic energy resolutions. Detector counts for the curved and the AR geometry analyser holders as a function of E_i , and Gaussian fits to the data (black). The scans were made separately and are plotted together for comparison, and some scan points between the peaks are hence counted several times. Data from the curved (AR) analysers are labeled by solid (open) symbols and connected by solid (dashed) lines. The 2.5, 3.0, 3.5, 4.0, 4.5 meV channels are colour coded by \bullet , \bullet , \bullet , \bullet , and \bullet , respectively.

We suspect that one of the three analyser crystals in this holder has fallen out, since the intensity in this channel is much lower than in the neighbouring channels, both when considering the curved geometry that was supposed to be a slight improvement and when considering the 2.5 meV and 3.5 meV channels immediately before and after it in the neutron beam. However, missing just one analyser crystal does not explain why the intensity drops by more than half, rather than just a third. When the prototype is eventually disassembled, there might be clues to the poor performance.

We also see that there is slight misalignment for the 3.5 meV curved analyser where the fitted Gaussian has its centre at 3.46 meV rather than at 3.50 meV.

Channel	2.5 meV	3.0 meV	3.5 meV	4.0 meV	4.5 meV
Experimental values					
Increase [%]	9(3)	134(5)	-10(2)	20(3)	14(4)
Cur. width [μeV]	57(2)	79.2(12)	129(2)	182(4)	209(5)
AR width [μeV]	52(2)	82.4(19)	142(2)	200(4)	209(5)
Simulated values					
Increase [%]	11.8(8)	7.4(6)	7.6(5)	11.9(4)	14.8(4)
Cur. width [μeV]	53.0(2)	78.6(2)	103.1(2)	128.3(3)	158.3(3)
AR width [μeV]	52.6(2)	74.9(2)	99.8(3)	128.4(3)	160.3(3)
Comb. error [%]	3.2	5.4	2.3	3.4	3.5
Channel		2.5 meV		5.0 meV	
FLEXX widths [μeV]		70		170	

Table 7: The experimental increase in % using the curved over the AR analyser geometry in the elastic setting, and the experimental and simulated values for the energy widths for each of the five energy channels. The combined error (added in quadrature) of the experimental and simulated improvements. For comparison, the energy widths for the ordinary FLEXX back-end is given at 2.5 meV and 5.0 meV.

The experimental values for peak intensity and width are given in table 7, along with the simulated values from section 8.1.1. Due to the problems with some of the analysers, we only have meaningful measurements of the energy width for both curved and AR for the 4.0 meV 4.5 meV analysers, and measured half the energy width for the 2.5 meV channels. These three channels all see an increase in intensity for the curved analyser over the AR analyser. Calculating the combined error from experiment and simulation, we find that for the 2.5 meV and 4.5 meV, the difference between experiment and simulation is within one standard deviation. For the 4.0 meV channel, the increase from curved over AR in the experiment is beyond two standard deviations from the simulated value. Another scan over E_i in the range around 4.0 meV than the one included in table 7 showed similar improvements beyond what the simulations suggested would be attainable. In [50], it is stated that McStas is valid to within 10 % of experiments due to systematical errors in the instrument code, and predicting a 12 % increase and measuring one of 20 % is well within expectations.

The intensity for the misaligned channel is 10% lower than for the AR channel, as opposed to the expected 8% increase. The decrease in intensity is not surprising, as the analyser scatters the neutrons into a different direction than that of the detector. Instead, some of the neutrons will be hitting the shielding around the detector.

For the energy widths, we find that the the two 2.5 meV channels and the curved 3.0 meV channel match the simulated values reasonably well, i.e. within two standard deviations. The AR 3.0 meV channel that we suspect are missing its middle analyser crystal seems to have a slightly larger energy width than both the simulations and the curved 3.0 meV channel. There are no intuitive explanation for an energy broadening due to a missing analyser crystal, so the measured energy width might be representative of the result had the analyser not been faulty.

For the rest of the channels, the measured energy widths are much larger than the simulated ones, but are still consistent between the curved and AR analysers. Disregarding the misaligned curved 3.5 meV channel, we find energy width broadenings of approximately 40% for the AR 3.5 meV, 64% and 70% for the 4.0 meV curved and AR, respectively, and approximately 75% for both the curved and the AR 4.5 meV channels.

When comparing to the values for the ordinary FLEXX TAS back-end, we find that for the 2.5 meV channel the resolution is slightly lower for the MultiFLEXX. For the similar energies 4.5 meV and 5.0 meV, the MultiFLEXX has slightly higher resolution.

The reason for the broadenings could be sample size, we saw in section 8.2 that there is a significant broadening from sample size increases. However, for the 2.5 meV channel the simulations in figure 24 show that the effect of increasing the sample size from 0.5 cm to 5.0 cm should be a doubling in energy width, and we are by no means close to that sample size here.

It is interesting that there seems to a good correspondence between the experimental results and the simulations for the two lowest energy channels and then a sudden jump to the rather poor correspondence for the three highest energy channels. It should, however, be noted that the experimental results agree amongst themselves, and that we still see an increase in intensity for the three channels we can perform meaningful experiments on, without a significant increase or a small decrease in energy width. These differences might be explained by the differences between the simulated FLEXX front-end and the PANDA front-end that we perform experiments at.

The results do, however, suggest that the estimate for maximum sample height given in 8.2 is not valid. Since, for a sample height of 1 cm, we already see some peaks in figure 31 that have overlapping regions, a further increase in sample height as simulated in figure 24 would only worsen this problem.

To assess the precision of the alignment method described in section 9.1.1, we have tabulated the center of the Gaussian fits from figure 31 in table 8. We have confirmed that the misalignment of the curved 3.5 meV analyser is due to the two sets of marks, one for curved and one for AR alignment, where an experimenter mistakenly used the wrong mark in the laser setup described in section 9.1.1. The alignment of the remaining 9 channels is accepted, and we can conclude that the method of laser alignment and the setup bench we constructed works as expected.

Channel	2.5 meV	3.0 meV	3.5 meV	4.0 meV	4.5 meV
Curved centre [meV]	2.512(1)	3.013(1)	3.459(1)	3.992(2)	4.501(2)
AR centre (fit)[meV]	2.511(1)	3.017(1)	3.510(1)	4.006(2)	4.520(2)

Table 8: The mean analyser value, as found from the fits to the peaks in figure 31. All peaks are very close to their nominal value, with the exception of the curved 3.5 meV channel that is slightly off. For this channel, we also found poorer performance in intensity than expected.

10.3 Phonon experiments and inelastic widths

The MultiFLEXX will, when finished, be used to map phonon and magnon dispersion relations in a wide range of samples. To give an impression of the instrument performance under such an experiment, we exchanged the V sample for a crystal of Pb to attempt to measure a phonon line. Pb is a standard test sample, and its phonon dispersion has been well-known for many years[51, 52]. We measured at room temperature, e.g. 300 K.

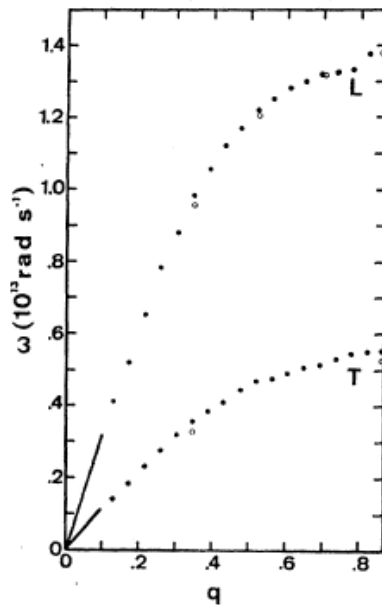


Figure 32: The phonon dispersion in the (111) direction for lead at 300 K (open circles) and at 80 K (filled circles). Figure taken from [52]

We aligned the Pb sample to have the (110) and (001) axes in the scattering plane, allowing us to reach the (111) Bragg peak that has the lowest allowed q , such that we can use low neutron energies for the experiment.

With the Pb sample, we also want to investigate the resolution of the instrument for inelastic scattering, since a sample that is inelastic and dispersionless, as we simulated in 8.1.2, is not readily available. Here, we will find both the energy and the \mathbf{Q}_\perp width, roughly corresponding to the width of the resolution

ellipsoid described in section 6.1 in the energy and in the \mathbf{Q}_\perp direction. In our elastic scans above, there is no way to measure the \mathbf{Q} -resolution, since the incoherent scattering is the same for all values of \mathbf{Q} .

The MultiFLEXX, due to its multiplexing abilities, poses a challenge when paired with an ordinary TAS such as PANDA, since the software can only comprehend a single E_f and A4 angle. Therefore, we decided upon choosing the q -channel containing the curved analysers to be the one we aligned to. For scans in E_i , where the PANDA software required as input a ΔE value, we established that ΔE should be calculated with respect to the $E_f = 4$ meV energy channel.

10.3.1 Bragg peak resolution

With the sample rotated into the Bragg condition for $E_i = 4.5$ meV in a Pb sample, scanning over A4 in the range around 2A3 we should see two peaks in the energy channels corresponding to $E_i = 4.5$ meV, spaced in A4 by the angular spacing between two q -channels. Such a scan is shown in figure 33, where fits to the two peaks show that they have centres that are spaced 2.51° apart, close to the 2.545° of the instrument specifications. Both peaks have a FWHM of 0.64° , while the 2 cm wide analyser crystal for the 4.5 meV analyser placed a distance $L_3 = 173.2$ cm from the sample has an angular width of 1.3° . This corresponds closely to the difference between start and end point of the two peaks.

From Braggs Law (37) for $E_i = 4.5$ meV, we calculate that we should see a Bragg peak at $2\theta_A = 97.8^\circ$. During set-up, we zeroed the rotation of A4 to the curved energy channel, and we now find that the centre for the curved energy channel peak is at $A4 = 97.4^\circ$. This small discrepancy is accepted, due to the quick set-up of the instrument.

For the measurements, we performed both energy and \mathbf{Q} -scans, as described in section 3.3.1.

For both types of measurements, the initial alignment of the sample is important. The A3 value that the instrument outputs has some offset, which we need to calculate in order to construct a correct scattering triangle. This was done by first constructing the scattering triangle for the channel that we aligned to, the curved 4.0 meV channel, in an instrument frame of reference where \mathbf{k}_i is pointing along the x -axis. Since the PANDA instrument control was set to measure at a particular point $\mathbf{q}_{\text{meas.}}$, we can find the angle between $\mathbf{q}_{\text{meas.}}$ and $\mathbf{q}_{\text{lab.}}$. Now, we can construct the \mathbf{q} -vectors for the nine channels we did not align to in the instrument frame of reference and rotate them with the angle found for the alignment channel, which should yield 10 $\mathbf{q}_{\text{meas.}}$ -vectors that are positioned close to the alignment channel in \mathbf{Q} -space. It is these measurement points that are shown in figures 34 and 36.

10.3.2 Incoming energy scan

We performed a single E -scan, where we moved the instrument in position to measure at $Q = (0.90.91.2)$ with the curved 4.0 meV channel, while scanning the incoming energy from $E_i = 4.49$ meV to $E_i = 6.14$ meV. As for normal TAS operation, a combination of changes to A3 and A4 can be calculated that does not change the point chosen in \mathbf{Q} even though k_i changes in length. This is however only the case for the channel that we aligned to initially, such that the changes in scattering geometry affects the remaining 9 measurement points.

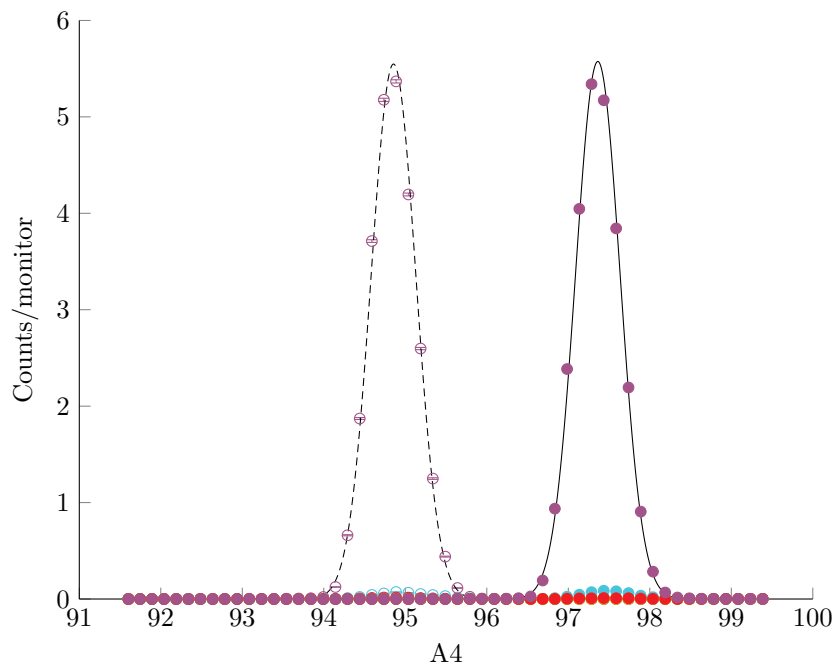


Figure 33: A scan over A4 in a range around 2A3 with the sample in the Bragg condition. Peaks are observed at approximately 97.8° for the curved (filled circles, solid lines) 4.5 meV channel and at 95.3° for the AR (open circles, dashed lines) 4.5 meV channel. A Gaussian is fitted to each peak (black). The two peaks are offset with an angle corresponding to the angular distance between two q -channels, and the width of the peak matches the angular width of an analyser crystal at L_3 .

These channels move in the $(hh0) - (00l)$ plane as we change E_i , with the points in \mathbf{Q} measured by the two 2.5 meV energy channels points moving the most. Mapping the measurement points in \mathbf{Q} will therefore look as shown in figure 34.

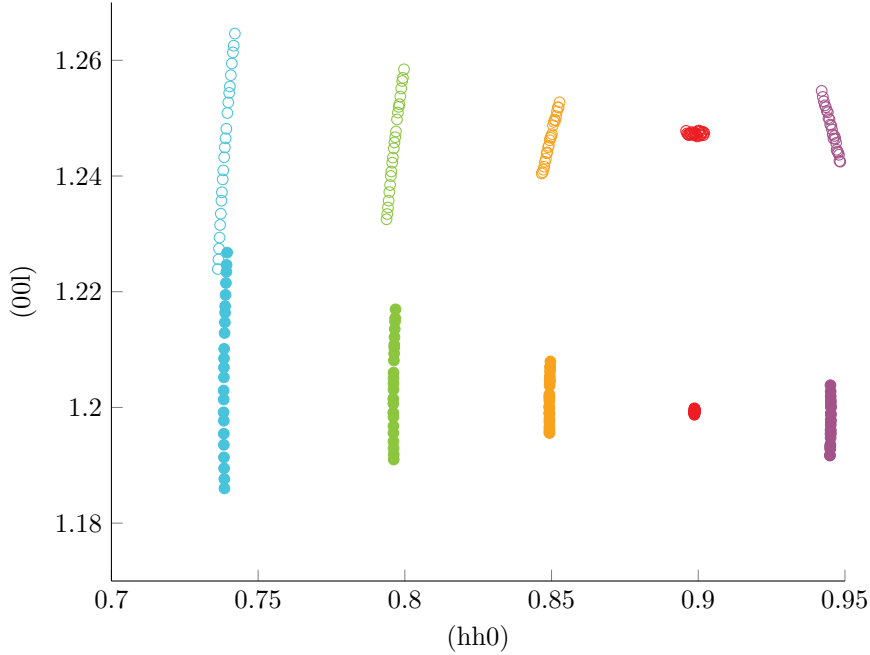


Figure 34: Measurement points in \mathbf{Q} for an E -scan, curved analyser channels are (filled circles) and AR analyser channels are (open circles). The measurements from the curved 4.0 meV energy channel does not move away from $\mathbf{Q} = (0.9\ 0.9\ 1.2)$, while the one for the AR 4.0 meV analyser is smeared around the initial point. Other energy channels describe lines in \mathbf{Q} -space. Data from the curved (AR) analysers are labeled by solid (open) symbols. The 2.5, 3.0, 3.5, 4.0, 4.5 meV channels are colour coded by ●, ●, ●, ●, and ●, respectively.

The E -scan can be used to measure the energy width of the resolution, as described in section 6. When the energy and measurement point in \mathbf{q} coincides with a phonon dispersion in lead, we will see a peak in intensity for that channel. Since we measure at many points close to each other, there will likely be more peaks over a single E -scan. The raw data from the E -scan, with Gaussian fits used to estimate the energy widths, can be seen in figure 35. Since not all energy channels were close to the dispersion in lead, we have not been able to estimate the energy width for all channels. For those energy channels that we have been able to measure, the results are shown in table 9

The inelastic energy widths in table 9 are following the trend from the elastic energy widths in section 10.2, where they are roughly consistent for the lower energy channels and quite inconsistent for the high energy channels. For the AR 4.0 meV channel, the energy width from experiment is almost 3.5 times the width we simulated it to be. It should be noted that we are using a different type of sample in the experiment compared to the very simple, dispersionless

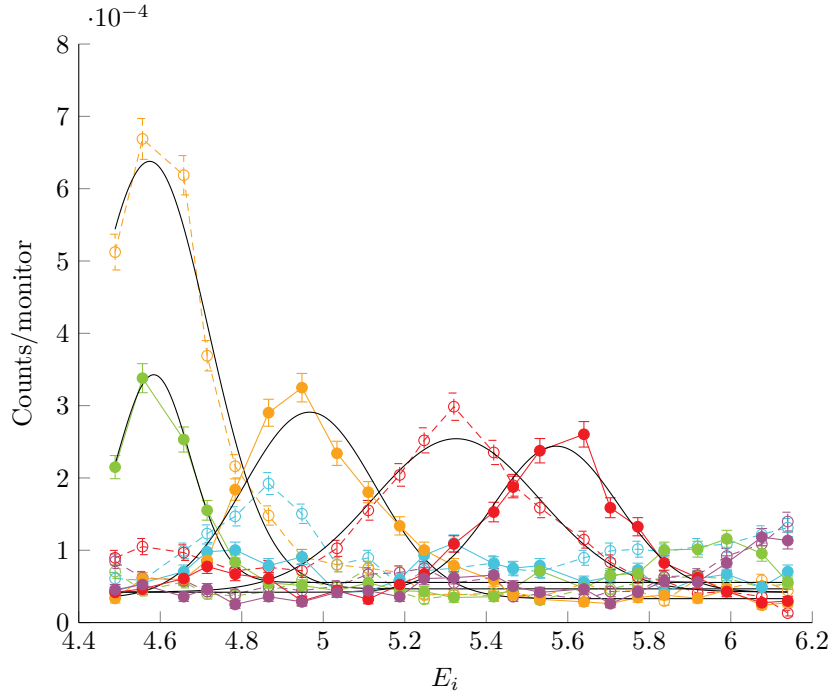


Figure 35: The raw data from an E -scan from $E_i = 4.49$ meV to $E_i = 6.14$ meV. Five peaks are identified, and a Gaussian fit (black) are made to these peaks, from which we can determine the energy width. Due to their slightly different positions in \mathbf{Q} -space, the curved and AR analysers are not measuring at the same energy transfer due to the phonon dispersion that we are measuring. Data from the curved (AR) analysers are labeled by solid (open) symbols and connected by solid (dashed) lines. The 2.5, 3.0, 3.5, 4.0, 4.5 meV channels are colour coded by \color{cyan} , \color{green} , \color{orange} , \color{red} , and \color{purple} , respectively.

Channel	3.0 meV	3.5 meV	4.0 meV
Cur. $\hbar\omega$ [meV]	1.6	1.4	1.6
Exp. curved width [μeV]	210(15)	379(15)	357(19)
Sim. curved width [μeV]	105.3(2)	122.4(3)	141.3(3)
AR $\hbar\omega$ [meV]	 	1.1	1.3
Exp. AR width [μeV]	 	340(17)	481(22)
Sim. AR width [μeV]	103.0(3)	120.1(3)	141.2(3)

Table 9: The inelastic energy widths as found from the Gaussian fits to the peaks in figure 35, compared with the results from the inelastic resolution simulations. The crossed spaces means that no energy widths were measured for this energy channel.

incoherently scattering sample that we used for simulations. This sample did not take into effect focusing and de-focusing effects as those described in section 6.1.1, which is what we might see from the broadenings in table 9.

The energy widths should generally become broader as we increase the energy transfer and as we increase the E_f we measure at. Both of these effects can be attributed to the increase in uncertainty for larger energies from Braggs Law as described in section 3.4.1, and for larger energy transfers the monochromator is set for high-energy neutrons with less well-defined energies. In our case, the energy transfer for the different energy channels are quite similar, which means that the primary effect causing broadening should be the E_f we measure at. However, there is not a large variation on E_f in our case as well.

It is hard to make conclusions from the limited number of energy widths we have measured, but the difference between the AR and the curved 4.0 meV channels, where the AR has a much wider energy resolution even for slightly lower energy transfer goes against our predictions. Ideally, we should have performed two E -scans, one for each q -channel in the same A4, instead of one E -scan which compared energy widths at different \mathbf{Q} -points.

10.3.3 \mathbf{Q} scan

To change the point we measure at in \mathbf{Q} for all 10 energy channels, we can rotate the sample angle A3 while keeping $E_i = 4.62$ meV and A4 fixed. In terms of the scattering triangle figure 4, this corresponds to keeping \mathbf{q} fixed and rotating the coordinate system and we expect to measure along 10 paths through \mathbf{q} . In figure 36, we have performed A3 scans at three different A4 angles with 1° difference between them, changing \mathbf{q} and with them where we measure. The result for these three scans are hence measurement points along 30 different paths. The scans were performed such that one endpoint of the curved 4.0 meV channel path hit the $\mathbf{Q} = (0.9\ 0.9\ 1.2)$ point for the initial A4 angle, before performing the same scan at two other A4 angles.

For one of the three \mathbf{q} -scans, the raw data can be seen in figure 37 along with the Gaussian fits that we use to determine the \mathbf{q} -width. Since we are interested in the \mathbf{q} -widths in [r.l.u.], we need to convert the width of the Gaussians in terms of angle to the distance covered in \mathbf{q} due to this change in angle. To do this, we can correlate the distance between two measurement points in figure 36 taken by the same energy channel to the change in angle from the first to the second setting. A different conversion rate is needed for all 30 measurement paths shown.

The measured \mathbf{Q} -widths are shown in table 10. For the three different scans, we observed peaks in the same energy channels as we did for our energy scan. However, the 4.0 meV channels have peaks as can be seen in figure 37 that are visible but not entirely within the scan range. Since we cannot see the centre of the peaks, fits to these are very inaccurate, and we have omitted them.

It is only the 3.5 meV energy channel that has usable peaks to determine the \mathbf{Q} -widths for both the AR and the curved analyser. For these energy channels, we find that the \mathbf{Q} -widths are roughly consistent amongst the three scans, with the curved analyser having a slightly smaller width. The curved 3.0 meV channel in turn has a slightly smaller width than was the case for the curved 3.5 meV channel. This could be because the k_f length is smaller, and an energy uncertainty is hence translated to a smaller \mathbf{Q} -width, or it could be differences

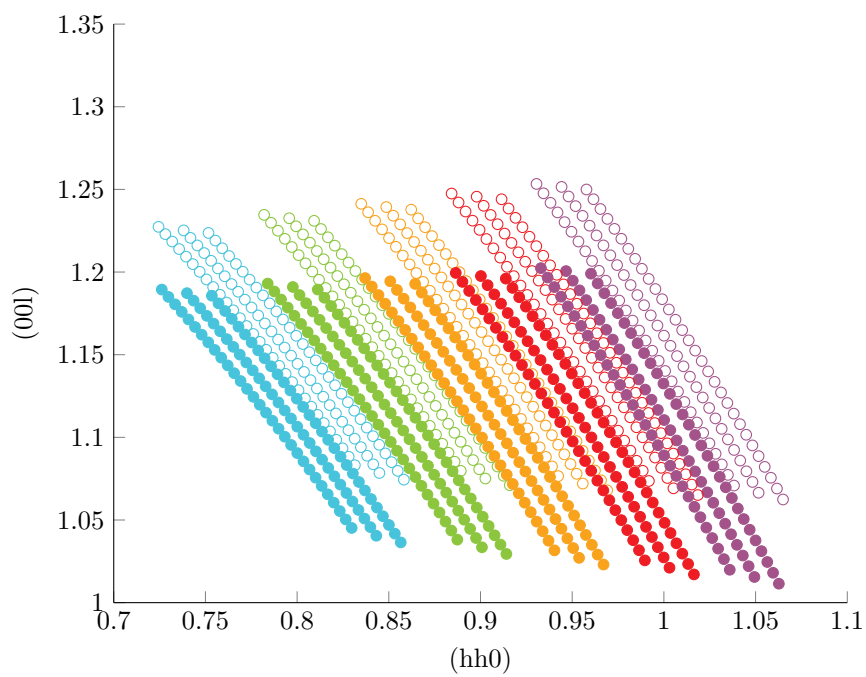


Figure 36: Measurement points in \mathbf{Q} for an A3 scan. Each energy channel measures along its own line in the $(hh0)$ - $(00l)$ plane. Data from the curved (AR) analysers are labeled by solid (open) symbols. The 2.5, 3.0, 3.5, 4.0, 4.5 meV channels are colour coded by \bullet , \bullet , \bullet , \bullet , and \bullet , respectively.

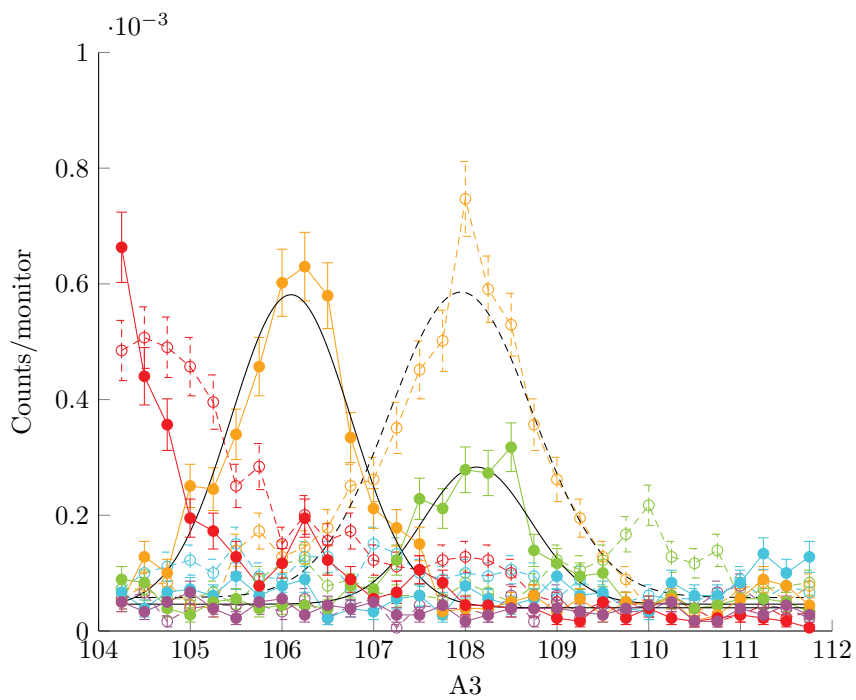


Figure 37: The raw data from the **Q**-scan at $A_4 = 102.0^\circ$. Although there is evidence of five peaks, only three are fully included in the scan and can have a Gaussian fits (black) made to them. Data from the curved (AR) analysers are labeled by solid (open) symbols and connected by solid (dashed) lines. The 2.5, 3.0, 3.5, 4.0, 4.5 meV channels are colour coded by \bullet , \bullet , \bullet , \bullet , and \bullet , respectively.

in the resolution function, as discussed in section 6.1.1.

Channel	3.0 meV	3.5 meV
A4 = 101.0°		
$\hbar\omega$ [meV]	1.62	1.12
Curved width [r.l.u.]	0.037(3)	0.040(2)
AR width [r.l.u.]	 	0.043(2)
A4 = 102.0°		
Curved width [r.l.u.]	0.034(3)	0.040(2)
AR width [r.l.u.]	 	0.048(2)
A4 = 103.0°		
Curved width [r.l.u.]	0.030(5)	0.043(2)
AR width [r.l.u.]	 	0.045(2)

Table 10: The \mathbf{Q} -widths as found from the Gaussian fits to the peaks in figure 35. The crossed spaces means that no \mathbf{Q} -widths were successfully measured for this energy channel.

10.3.4 Phonon mapping

Mapping experiments will be the primary task for MultiFLEXX, so we have attempted to put the limited amount of data we gathered in the inelastic setting together to create the mapping plots. For this, we have calculated the distance from the measuring points shown in figures 34 and 36 to the (1 1 1) Bragg point. Data points are given by circles coloured according to the detector intensity at this measurement point. Since we have different performances for the different energy channels, the data points have all been normalised to the curved 2.5 meV by their peak height \times peak width. The mapping data for the E -scan is given in figure 38. Here, we find that there is an increase in intensity around $\hbar\omega = 1.5$ meV, sloping slightly downwards to the right. We can also see that the two 2.5 meV energy channels are measuring at a high intensity for all $\hbar\omega$. This can be attributed to the high levels of background that was continually seen in these channels. Meanwhile, the AR 3.0 meV channel also shows a high intensity at all $\hbar\omega$, which is the effect of this analyser having a poor performance, and hence the few counts it sees are boosted in the normalisation process.

For the \mathbf{Q} -scan, we find the phonon mapping result looking as in 39 for the measurement at A4 = 102°. Here, we again find a feature of high intensity going downwards to the right. The difference in slope can be attributed to the different x -axis scalings, but this has not been investigated further. There are still very high intensities in the 2.5 meV energy channels and in the 3.0 meV, which do not seem to match the feature, and can probably be attributed to background.

There seems to be a problem with the phonon mapping, since we expect the dispersion relation that we measure to slope towards the Bragg point, as seen in figure 32. The fact that we are sloping in the opposite direction suggests that there is an error in the data treatment, as the feature is definitely not a statistical error. It has been suggested that the PANDA definition of positive

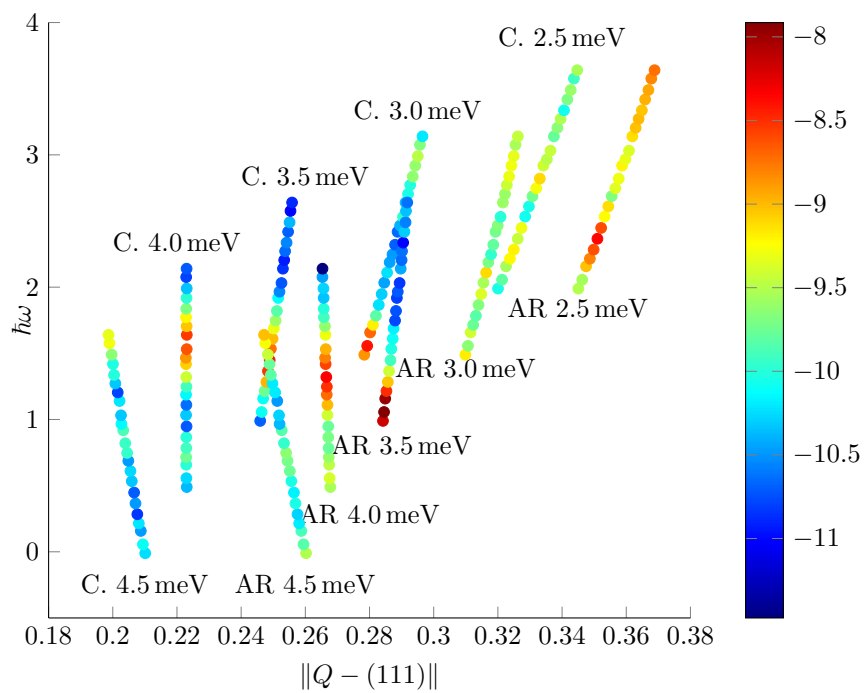


Figure 38: Distance from Bragg point (111) to \mathbf{Q} vs. energy for the E -scan. The logarithm of the detector intensity is given by the color of the data points, and all intensities are normalised to the curved 2.5 meV channel. A feature is seen going from top left to bottom right.

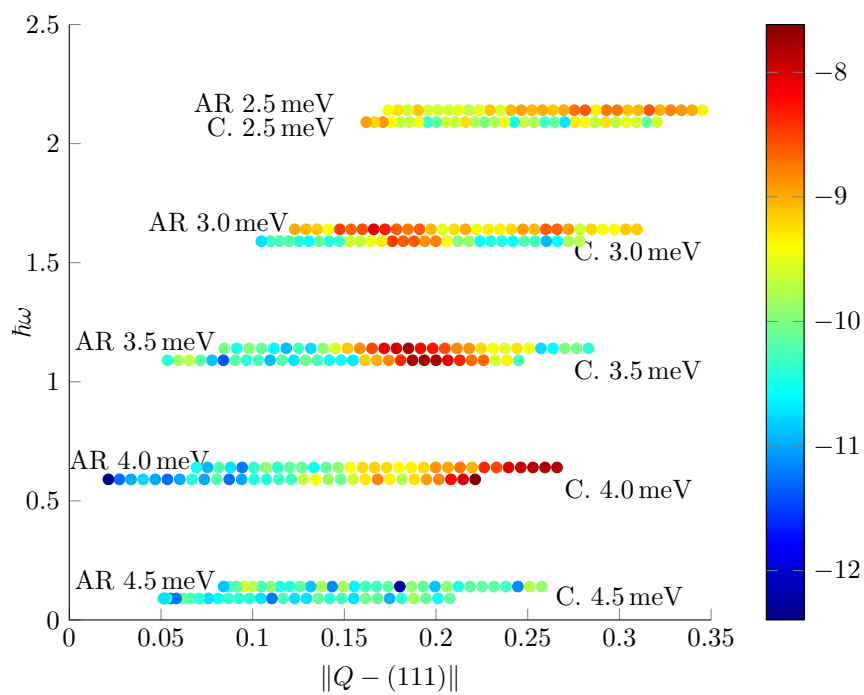


Figure 39: Distance from Bragg point (1 1 1) to \mathbf{Q} vs. energy for the A3-scan at $A4 = 102^\circ$. The logarithm of the detector intensity is given by the color of the data points, and all intensities are normalised to the curved 2.5 meV channel. A feature is seen going from top left to bottom right.

rotation for A3 and A4, respectively, could be reversed with respect to the data treatment. If there is an error in the data treatment, figures 34 and 36 are also affected.

Given more time, the rotations would have been investigated further, and the data from the E -scan and the three \mathbf{Q} -scans would have been collected in order to establish the slope of the feature seen in the data, for comparison with the known phonon dispersion in Pb.

10.4 Background measurements

Even the best neutron instruments in the world are useless, if their signals are drowned out in background from different sources. In fact, the best instruments are often characterised by their low and uniform background. To estimate what amount of background we can expect in the finished experiment, many experiments were performed with the vanadium sample and varying degrees of shielding and blocking, as well as measurements where crosstalk between different energy channels and q -channels were measured.

10.4.1 Crosstalk and shielding

To measure the crosstalk, we scanned the prototype A4 with the Pb sample aligned to a Bragg peak at energies $E_i = 4.5$ meV and $E_i = 5.2$ meV. The first of these scans was also shown in figure 33, but it is repeated in figure 40, this time with the detector count in a logarithmic scale, where it is easier to see the fainter signals from the crosstalk.

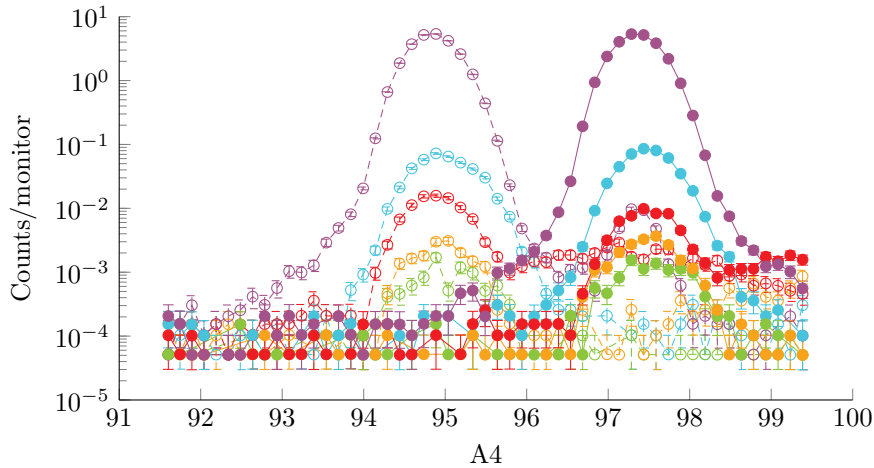


Figure 40: Logarithmic detector counts vs. A4 in a range around 2A3 with the sample in the Bragg condition for $E_i = 4.5$ meV. When the Bragg peak is detected for either the curved or the AR 4.5 meV energy channels, all other energy channels of the same type see a peak as well. Data from the curved (AR) analysers are labeled by solid (open) symbols and connected by solid (dashed) lines. The 2.5, 3.0, 3.5, 4.0, 4.5 meV channels are colour coded by $\color{blue}\bullet$, $\color{green}\bullet$, $\color{orange}\bullet$, $\color{red}\bullet$, and $\color{purple}\bullet$, respectively.

From figure 40, we see that a Bragg peak in the 4.5 meV energy channel in one q -channel gives a signal for all energy channels along that q -channel. Giving the Bragg peak an intensity of 10 on an arbitrary scale, we have the 3.0 meV energy channel at 2, followed by the 3.5 meV energy channel at 2.5, the 4.0 meV energy channel at 5 and finally the 2.5 meV energy channel at 6. Thus, the closer spatially the energy channel is to the Bragg energy channel, the higher the intensity in this channel, a result that is hardly surprising. The odd one out is the 2.5 meV energy channel, where the intensity is the highest, even though this energy channel is spatially the farthest removed from the Bragg energy channel. This can probably be attributed to the fact that, as we see from figure 7, the detector for this channel has the least amount of shielding on the front, towards the outside environment. However, since there is a peak in intensity at the Bragg angle, this peak is not attributable to general background radiation in the experimental area, but must come from Bragg scattered neutrons out of the plane.

The hopes before the prototype tests were that a Bragg peak in one q -channel would only affect the energy channels in that q -channel, such that this single q -channel could simply be excluded from the data. However, we find that the Bragg peak in the curved 4.5 meV energy channel creates a peak in the AR 4.5 meV energy channel, but not the other way around. This goes against intuition, as the shielding between the the two channel should be equally permeable from both sides.

Another strange feature from this scan is the signal from the 4.0 meV energy channel for both analyser types. Here, we have a background similar to that of the other energy channels on one side of the crosstalk peak for their channel, but a significantly higher background on the other side. The scan was performed from small to large A4, meaning that the higher background came after the q -channel had been exposed to the Bragg peak.

A similar scan is performed for $E_i = 5.2$ meV in figure 41. Assigning an intensity of 10 on an arbitrary scale to the 4.5 meV energy channel, we have approximately 10 in the 2.5 meV channel as well, while the 3.0 meV energy channel that had the least amount of crosstalk before now has approximately 8. This might be an effect of the neutrons that gave the peak in the 2.5 meV energy channel now penetrating through the thicker shielding to the 3.0 meV energy channel. The 3.5 meV channel and the 4.0 meV have approximately the same signal at 6-7.

Concerning the strange tails on the right side of the peaks in figure 40, we find them here for both the 4.0 meV and the 4.5 meV energy channels. The right-most scan points are added at a later time to resolve when and if the AR 4.5 meV energy channel tail disappears, and the signal in this channel finally begins to decrease at approximately $A4 = 90^\circ$, some 3° after the constant signal began. Interestingly, the tail from the 4.0 meV channel does not disappear within our scan. The fact that the right-most points are scanned at a later time rules out that anything in the MultiFLEXX could have been activated by the neutrons.

It is also worth considering higher order scattering, since the PANDA TAS front-end is not equipped with a velocity selector as the one described in 3.4.2. 2nd or higher order scattered neutrons from the monochromator can also be higher-order scattered from the analysers. A short table on these critical values is given in 11. Here, we see that the combination of 2nd order scattering from

the monochromator and 3rd order scattering from the analyser has an energy close to the 2.5 meV channel. There is also a combination of 3rd and 4th order scattering that may give problems in the 3.0 meV channel. This is, however, less likely as there are much fewer neutrons incoming at this energy. Comparing figures 40 and 41, we see that there is actually a decrease in counts in the 2.5 meV channel, so this seems to be less of a problem.

E_i	Scattered from monochromator			
	5.2 meV	20.8 meV	46.8 meV	83.2 meV
	Will N order scatter from analyser			
2 nd	1.3 meV	5.2 meV	11.7 meV	20.8 meV
3 rd	0.6 meV	2.3 meV	5.2 meV	9.2 meV
4 th	0.3 meV	1.3 meV	2.9 meV	5.2 meV

Table 11: A diagram showing where we can expect higher background due to higher order scattering from both monochromator and analyser.

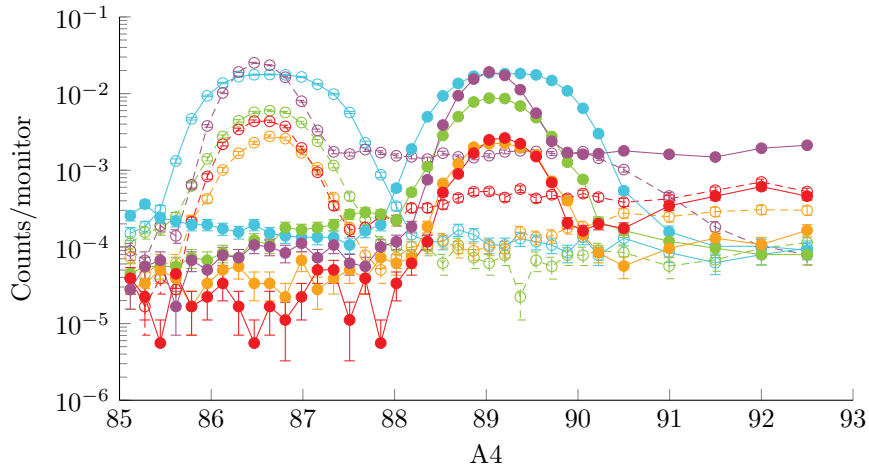


Figure 41: Logarithmic detector counts vs. A4 in a range around 2A3 with the sample in the Bragg condition for $E_i = 5.2$ meV. Data from the curved (AR) analysers are labeled by solid (open) symbols and connected by solid (dashed) lines. The 2.5, 3.0, 3.5, 4.0, 4.5 meV channels are colour coded by \bullet , \bullet , \bullet , \bullet , and \bullet , respectively.

The results in figure 40 and 41 seems to suggest that crosstalk will be a problem, since we found that a Bragg peak in one q -channel will give a signal in all energy channels for that q -channel. There is some ambiguity as to whether a Bragg peak in a single energy channel will leak into the same energy channels for neighbouring q -channels, since the experiment seems to suggest that the crosstalk is not symmetric, as we expect it to be. The $E_i = 5.2$ meV Bragg peak does not seem to leak from one q -channel to the next, bar the strange tails observed for the 4.0 meV and the 4.5 meV energy channels.

Further experiments should be made where the A4 is scanned in the opposite direction to see the effect on these tails. Furthermore, experiments at higher E_i 's

might provide an argument for the Be-filter suggested in section 4.1.2 if they show more crosstalk from a Bragg peak than we have seen at $E_i = 4.5$ meV and $E_i = 5.2$ meV.

11 Conclusion

In this masters thesis, I have given a short introduction to inelastic neutron scattering and the two kinds of spectrometer, the TAS and the ToF, that are currently being used to perform inelastic neutron scattering. I have then presented the MultiFLEXX, a new back-end option for the FLEXX TAS, and described how this multiplexing back-end can make it possible to perform measurements, namely mapping with parameterisation, that are impractical with the current spectrometer technology.

Below, I conclude on the two parts of the MultiFLEXX work where I have participated: Monte Carlo simulations and prototype experiments.

11.1 Simulations

We found that the analyser holders that had been designed and built for the MultiFLEXX were not of the Rowland geometry that they were supposed to be, due to a coordinate transformation error, but were rather anti-Rowland. The resulting analyser had a smaller than possible effective area, due to the individual analyser crystals it was made from having a region of overlap. Also, due to the proportions of the MultiFLEXX setup, it was not possible to use the Rowland geometry for the analysers. To test the effect of the overlapping analyser crystals, I created the MultiFLEXX in McStas and simulated the performance of the analyser by measuring the height and width of the peak on the detector when changing the incoming energy of neutrons onto an incoherent elastically scattering sample.

For comparison, I also simulated a simpler curved analyser geometry and optimised the curvature ρ for the MultiFLEXX. For the optimally curved analyser, I found that an improvement of between 7% and 15% for the fitted peak height was possible, depending on the final energy that the analysers should detect. The increase in peak height came with little to no effect on the width of the peak, thus keeping the resolution.

To investigate the situation in inelastic scattering, I simulated energy transfers from the neutron to the sample and measured the peak height and width for a fixed incoming neutron energy instead of a varying incoming energy. I found that the optimal curvature in this situation was close to that found for elastic scattering, and that using the optimally curved analyser geometries would result in an improvement of between 8% and 16% for the fitted peak height.

Since neutron scattering is limited by the amount of neutrons that we can measure, based on my simulations it was decided to change the analyser holders to the curved geometry, using the optimal curvature that I found.

11.2 Experiments

We performed a prototype test with the MultiFLEXX using the PANDA TAS front-end in order to test if the simulated improvements could be recreated in an experimental setting. To do this, we took two out of 31 q -channels of the finished MultiFLEXX and fitted one with the curved geometry analysers and the other with the AR geometry analysers. We measured in an elastic setup by using an incoherent elastically scattering V sample and changing the incoming energy. Due to misalignments and other experimental errors, only three out of

the five final detection energies could be directly compared, but they showed improvements between 9% and 20% for the peak height of a Gaussian fit to the data. The peak widths measured were similar to the simulated values for the 2.5 meV and the 3.0 meV channels, while the higher energy channels saw broadenings of between 25% and 56% compared to the simulations. For the two different analyser geometries, the widths were comparable, as we also saw from the simulations.

We also attempted to measure the a signal in an inelastic setting by measuring a phonon dispersion in a Pb sample. Here, we have not made comparisons between the peak heights of the two different analyser geometries, but we have measured the widths. These are found to be broadened by a large amount compared to what we found in the simulations, but in line with the result we got from the elastic measurements.

Furthermore, we performed different tests on background and crosstalk. In this thesis, we have given examples of the crosstalk we measure when a Bragg peak is directed into one of the two q -channels. We find that the Bragg peak will give a signal at all detector energies in the q -channel, and that a Bragg peak of the same energy as a detector energy can be detected at the corresponding detector energy in the other q -channel. We also report on an unexplained tail occurring only on the right side of several peaks.

The result of our mapping experiment is as of yet unresolved, since the phonon dispersion we measure seems to slope away from the Bragg point, rather than towards it. More work will be put into this problem to verify that we have indeed measured a phonon dispersion in Pb.

11.3 Outlook

The MultiFLEXX will be assembled in December 2014 and January 2015 and should be ready for tests with all 31 q -channels in early 2015. After that, it will be possible for users at the FLEXX instrument to opt for the MultiFLEXX back-end over the ordinary FLEXX back-end, which will add to the tool-box of the neutron scattering society and hopefully lead to exciting new findings.

References

- [1] ILL - key dates, December 2014. URL: <http://www.ill.eu/about/what-is-the-ill/history/ill-key-dates/> [cited November 2014].
- [2] Kim Lefmann, Bente Lebech, and Andrew Wildes. *Neutron Scattering: Theory, instrumentation, and simulation*. Unpublished Course Notes, NBI, Copenhagen, Denmark, 2013.
- [3] The Nobel Prize in physics 1935, November 2014. URL: http://www.nobelprize.org/nobel_prizes/physics/laureates/1935/ [cited November 2014].
- [4] A. T. Yue, M. S. Dewey, D. M. Gilliam, G. L. Greene, A. B. Laptev, J. S. Nico, W. M. Snow, and F. E. Wietfeldt. Improved determination of the neutron lifetime. *Phys. Rev. Lett.*, 111:222501, Nov 2013. URL: <http://link.aps.org/doi/10.1103/PhysRevLett.111.222501>, doi:10.1103/PhysRevLett.111.222501.
- [5] Albert-Jose Dianoux and Gerry Lander. *Neutron Data Booklet*. ILL, Grenoble, France, 2nd edition edition, 2003.
- [6] NIST. Neutron scattering lengths and cross sections, January 2013. URL: <http://www.ncnr.nist.gov/resources/n-lengths/> [cited November 2014].
- [7] Charles Kittel. *Introduction to Solid State Physics*. Wiley, 2005.
- [8] G.L. Squires. *Introduction to the Theory of Thermal Neutron Scattering*. Cambridge University Press, Cambridge, UK, 1978.
- [9] The Nobel Prize in physics 1994, November 2014. URL: http://www.nobelprize.org/nobel_prizes/physics/laureates/1994/ [cited November 2014].
- [10] Neutron centres, November 2014. URL: <http://neutronsources.org/neutron-centres.html> [cited November 2014].
- [11] Robert L. Kustom. Intense pulsed neutron sources. *IEEE Transactions on Nuclear Science*, NS-28, 1981.
- [12] Fujio Maekawa, Masahide Harada, Kenichi Oikawa, Makoto Teshigawara, Tetsuya Kai, Shin ichiro Meigo, Motoki Ooi, Shinichi Sakamoto, Hiroshi Takada, Masatoshi Futakawa, Takashi Kato, Yujiro Ikeda, Noboru Watanabe, Takashi Kamiyama, Syuki Torii, Ryoichi Kajimoto, and Mitsutaka Nakamura. First neutron production utilizing j-parc pulsed spallation neutron source {JSNS} and neutronic performance demonstrated. *Nucl. Instr. Meth. A*, 620(23):159 – 165, 2010. URL: <http://www.sciencedirect.com/science/article/pii/S016890021000822>, doi:<http://dx.doi.org/10.1016/j.nima.2010.04.020>.
- [13] Oak ridge national laboratory: Spallation neutron source, December 2014. URL: <http://neutrons.ornl.gov/> [cited December 2014].

- [14] European spallation source, December 2014. URL: <http://europeanspallationsource.se/> [cited November 2014].
- [15] M.D. Le, D.L. Quintero-Castro, R. Toft-Petersen, F. Groitl, M. Skoulatos, K.C. Rule, and K. Habicht. Gains from the upgrade of the cold neutron triple-axis spectrometer FLEXX at the BER-II reactor. *Nucl. Instr. Meth. A*, 729:220 – 226, 2013. URL: <http://www.sciencedirect.com/science/article/pii/S0168900213009832>, doi:<http://dx.doi.org/10.1016/j.nima.2013.07.007>.
- [16] H. Maier-Leibnitz and T. Springer. The use of neutron optical devices on beam-hole experiments on beam-hole experiments. *Journal of Nuclear Energy. Parts A/B. Reactor Science and Technology*, 17(4 5):217 – 225, 1963. URL: <http://www.sciencedirect.com/science/article/pii/0368323063900223>, doi:[http://dx.doi.org/10.1016/0368-3230\(63\)90022-3](http://dx.doi.org/10.1016/0368-3230(63)90022-3).
- [17] Kaspar Hewitt Klenø, Klaus Lieutenant, Ken H. Andersen, and Kim Lefmann. Systematic performance study of common neutron guide geometries. *Nucl. Instr. Meth. A*, 696(0):75 – 84, 2012.
- [18] Jens Als-Nielsen and Des McMorrow. *Elements of Modern X-Ray Physics*. Wiley, Chichester, UK, 2001.
- [19] B. Dorner and A. Kollmar. Is pyrolytic graphite an ideal mosaic crystal? *Journal of Applied Crystallography*, 7(1):38–41, Feb 1974. URL: <http://dx.doi.org/10.1107/S0021889874008661>, doi:10.1107/S0021889874008661.
- [20] H. Schober, E. Farhi, F. Mezei, P. Allenspach, K. Andersen, P.M. Bentley, P. Christiansen, B. Cubitt, R.K. Heenan, J. Kulda, P. Langan, K. Lefmann, K. Lieutenant, M. Monkenbusch, P. Willendrup, J. Šaroun, P. Tindemans, and G. Zsigmond. Tailored instrumentation for long-pulse neutron spallation sources. *Nucl. Instr. Meth. A*, 589(1):34 – 46, 2008. URL: <http://www.sciencedirect.com/science/article/pii/S0168900208001551>, doi:<http://dx.doi.org/10.1016/j.nima.2008.01.102>.
- [21] K.N. Clausen, D.F. McMorrow, K. Lefmann, G. Aeppli, T.E. Mason, A. Schröder, M. Issikii, M. Nohara, and H. Takagi. The RITA spectrometer at Risø – design considerations and recent results. *Physica B*, 241–243:50 – 55, 1997.
- [22] C.R.H. Bahl, P. Andersen, S.N. Klausen, and K. Lefmann. The monochromatic imaging mode of a RITA-type neutron spectrometer. *Nucl. Instr. Meth. B*, 226(4):667 – 681, 2004. URL: <http://www.sciencedirect.com/science/article/pii/S0168583X04008791>, doi:<http://dx.doi.org/10.1016/j.nimb.2004.07.005>.
- [23] R. Born and D. Hohlwein. Simultaneous energy analysis in a large angular range: A novel neutron spectrometer, its resolution and applications. *Zeitschrift für Physik B Condensed Matter*, 74(4):547–555, 1989.

- [24] M. Kempa, B. Janousova, J. Saroun, P. Flores, M. Boehm, F. Demmel, and J. Kulda. The FlatCone multianalyzer setup for ILL's three-axis spectrometers. *Physica B: Condensed Matter*, 385-386:1080–1082, 2006. doi:10.1016/j.physb.2006.05.371.
- [25] Jonas O. Birk, Márton Markó, Paul G. Freeman, Johan Jacobsen, Rasmus L. Hansen, Niels B. Christensen, Christof Niedermayer, Martin Månsson, Henrik M. Rønnow, and Kim Lefmann. Prismatic analyser concept for neutron spectrometers. *Review of Scientific Instruments*, 85(11):-, 2014. URL: <http://scitation.aip.org/content/aip/journal/rsi/85/11/10.1063/1.4901160>, doi:<http://dx.doi.org/10.1063/1.4901160>.
- [26] P. G. Freeman, J. O. Birk, M. Marko, N. B. Christensen, J. Larsen, C. Niedermayer, J. Fanni, A. L. R. Hansen, K. Lefmann, and H. Rønnow. Ask Jonas. *EPJ Web of Conferences, QENS/WINS 2014 Proceedings*, 2014. *In preparation*.
- [27] Jakob Larsen. Pyrolytic graphite experimental results. Internal report, 2013. Experimental Report for the ESS CAMEA.
- [28] Paul Freeman. Benching Mark CAMEA Against Present Inelastic Neutron Spectrometers. Technical report, ESS, 2014. This work is carried out as part of the CAMEA work project. Members of this project are: Paul G. Freeman, Henrik M. Ronnow (EPFL), Christof Niedermayer, Fanni Jurányi, Márton Markó (PSI) Kim Lefmann, Jonas Okkels Birk, Mads Bertelsen (University of Copenhagen) Niels Bech Christensen, Jacob Larsen (Technical University of Denmark).
- [29] J A Rodriguez, D M Adler, P C Brand, C Broholm, J C Cook, C Brocker, R Hammond, Z Huang, P Hundertmark, J W Lynn, N C Maliszewskyj, J Moyer, J Orndorff, D Pierce, T D Pike, G Scharfstein, S A Smee, and R Vilaseca. MACS – a new high intensity cold neutron spectrometer at NIST. *Measurement Science and Technology*, 19(3):034023, 2008. URL: <http://stacks.iop.org/0957-0233/19/i=3/a=034023>.
- [30] Klaus Habicht, Diana Lucía Quintero-Castro, Rasmus Toft-Petersen, Mathias Kure, Lucas Mäde, Felix Groitl, and Manh Duc Le. The upgraded cold neutron triple-axis spectrometer FLEXX - enhanced capabilities by new instrumental options. *EPJ Web of Conferences, QENS/WINS 2014 Proceedings*, 2014. *In preparation*.
- [31] J. O. Birk. *Personal communication*.
- [32] Mathias Kure. Measuring the mosaicity of PG crystals for a new instrument. Report in the neutron scattering course, 2014.
- [33] Gen Shirane, Stephen M. Shapiro, and John M. Tranquada. *Neutron scattering with a Triple-Axis Spectrometer*. Cambridge University Press, Cambridge, UK, 2002.
- [34] K. Habicht and M. Skoulatos. Phase-space tailoring using the virtual source concept part I: Geometrical model. *Not published*, 2010.

- [35] M. Skoulatos, K. Habicht, and K. Lieutenant. Improving energy resolution on neutron monochromator arrays. *Journal of Physics: Conference Series*, 340, 2012.
- [36] M. J. Cooper and R. Nathans. The resolution function in neutron diffraction. i. the resolution function of a neutron diffractometer and its application to phonon measurements. *Acta Crystallographica*, 23(3):357–367, 1967. URL: <http://dx.doi.org/10.1107/S0365110X67002816>, doi: 10.1107/S0365110X67002816.
- [37] M. Popovici. On the resolution of slow-neutron spectrometers. iv. the triple-axis spectrometer resolution function, spatial effects included. *Acta Crystallographica Section A*, 31(4):507–513, 1975. URL: <http://dx.doi.org/10.1107/S0567739475001088>, doi:10.1107/S0567739475001088.
- [38] G. E. Peckham, D. H. Saunderson, and R. I. Sharp. Focusing conditions for a triple-axis neutron spectrometer. *British Journal of Applied Physics*, 18(4):473, 1967. URL: <http://stacks.iop.org/0508-3443/18/i=4/a=310>.
- [39] K. Lefmann, U. Filges, F. Treue, J.J.K. Kirkensgård, B. Plesner, K.S. Hansen, and K.H. Klenø. Optimal shape of a cold-neutron triple-axis spectrometer. *Nucl. Instr. Meth. A*, 634(1, Supplement):1–6, 2011. Proceedings of the International Workshop on Neutron Optics {NOP2010}. URL: <http://www.sciencedirect.com/science/article/pii/S0168900210014634>, doi:<http://dx.doi.org/10.1016/j.nima.2010.06.273>.
- [40] Mads Bertelsen. Optimizing neutron guides using the minimalist principle and guide_bot. Master’s thesis, University of Copenhagen, 2014.
- [41] Kim Lefmann and Kristian Nielsen. Mcstas, a general software package for neutron ray-tracing simulations. *Neutron News*, 10(3):20–23, 1999. URL: <http://dx.doi.org/10.1080/10448639908233684>, arXiv:<http://dx.doi.org/10.1080/10448639908233684>, doi: 10.1080/10448639908233684.
- [42] Peter Willendrup, E.B Knudsen, Esben Klinkby, Thomas Nørskov Nielsen, Emmanuel Farhi, U Filges, and Kim Lefmann. New developments in the mcstas neutron instrument simulation package. *Journal of Physics: Conference Series (Online)*, 528(1):012035, 2014. doi:10.1088/1742-6596/528/1/012035.
- [43] McStas - a neutron ray-trace simulation package, November 2014. URL: <http://www.mcstas.org/> [cited November 2014].
- [44] VITESS: Virtual Instrumentation Tool for Neutron Scattering at Pulsed and Continuous Sources, November 2014. URL: http://www.helmholtz-berlin.de/forschung/oe/em/transport-phenomena/projekte/vitess/index_en.html [cited November 2014].
- [45] RESTRAX:Monte Carlo simulations and data analysis for three-axis neutron spectrometers, November 2014. URL: <http://neutron.ujf.cas.cz/restrax/> [cited November 2014].

- [46] Wikipedia: The monte carlo method, November 2014. URL: http://en.wikipedia.org/wiki/Monte_Carlo_method#History [cited November 2014].
- [47] P. Willendrup, E. Farhi, E. Knudsen, and K. Lefmann. *Component Manual for the Neutron Ray-Tracing Package McStas*. DTU Department of Physics, Kongens Lyngby, Denmark, 1.12 edition, 2012.
- [48] P. Willendrup, E. Farhi, E. Knudsen, U. Filges, and K. Lefmann. *User and programmers guide to the neutron ray-tracing package McStas*. DTU Department of Physics, Kongens Lyngby, Denmark, 2.0 edition, 2012.
- [49] M Loewenhaupt and N.M Pyka. Design of the triple-axis spectrometer PANDA at the high-flux reactor FRM-II of Garching. *Physica B: Condensed Matter*, 267–268(0):336 – 340, 1999. URL: <http://www.sciencedirect.com/science/article/pii/S0921452699000241>, doi:[http://dx.doi.org/10.1016/S0921-4526\(99\)00024-1](http://dx.doi.org/10.1016/S0921-4526(99)00024-1).
- [50] K. Lefmann, P.K. Willendrup, L. Udby, B. Lebech, K. Mortensen, J.O. Birk, K.H. Klenø, E. Knudsen, P. Christiansen, J. Saroun, J. Kulda, U. Filges, M. Konnecke, P. Tregenna-Piggott, J. Peters, K. Lieutenant, G. Zsigmond, P. Bentley, and E. Farhi. Virtual experiments: The ultimate aim of neutron ray-tracing simulations. *Journal of Neutron Research*, 16(3-4):97–111, 2008.
- [51] B. Brockhouse, T. Arase, G. Caglioti, K. Rao, and A. Woods. Crystal dynamics of lead. i. dispersion curves at 100 k. *Phys. Rev.*, 128:1099–1111, Nov 1962. URL: <http://link.aps.org/doi/10.1103/PhysRev.128.1099>, doi:10.1103/PhysRev.128.1099.
- [52] R. Stedman, L. Almqvist, G. Nilsson, and G. Raunio. Dispersion relations for phonons in lead at 80 and 300 k. *Phys. Rev.*, 162:545–548, Oct 1967. URL: <http://link.aps.org/doi/10.1103/PhysRev.162.545>, doi:10.1103/PhysRev.162.545.

A Elastic scans over curvature

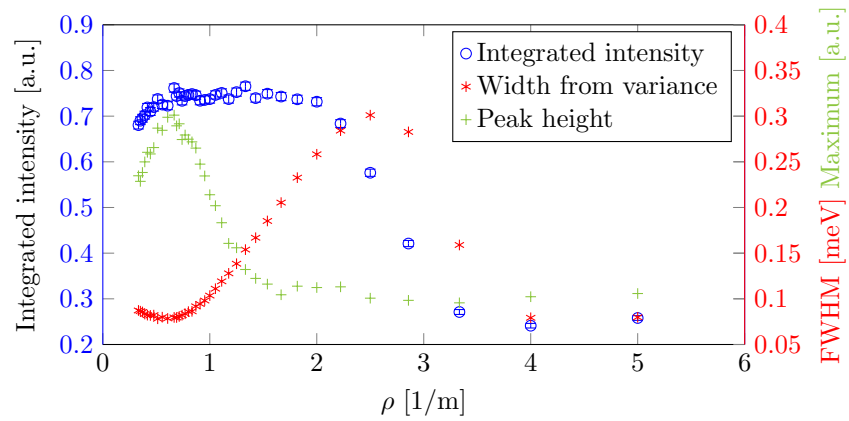


Figure 42: A range of simulations of the type in figure 17 that shows the effect of changing the curvature for the curved 3.0 meV energy channel. Peak intensity (green plus) normalised to the right axis, width (FWHM) (red asterisks), and integrated intensity (blue circles).

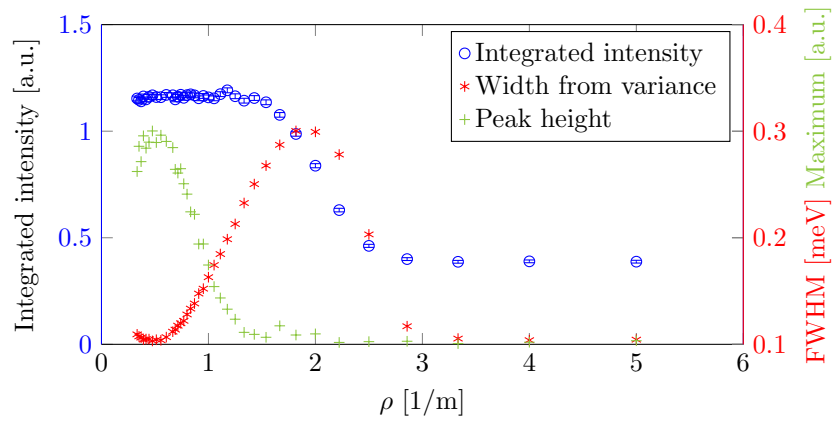


Figure 43: A range of simulations of the type in figure 17 that shows the effect of changing the curvature for the curved 3.5 meV energy channel. Peak intensity (green plus) normalised to the right axis, width (FWHM) (red asterisks), and integrated intensity (blue circles).

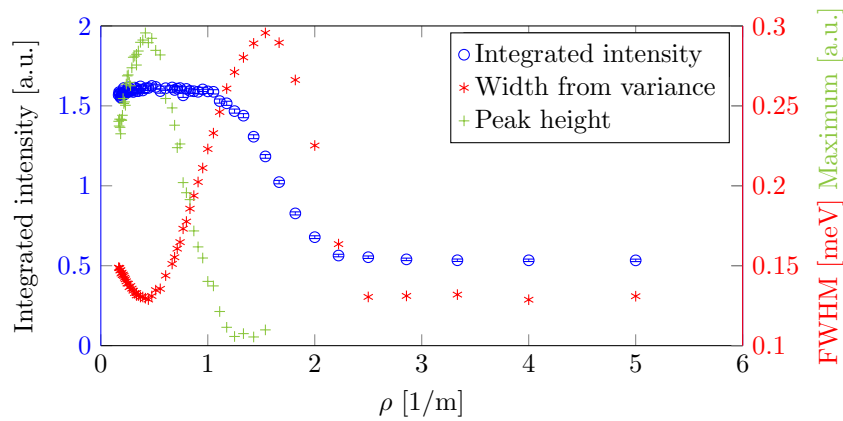


Figure 44: A range of simulations of the type in figure 17 that shows the effect of changing the curvature for the curved 4.0 meV energy channel. Peak intensity (green plus) normalised to the right axis, width (FWHM) (red asterisks), and integrated intensity (blue circles).

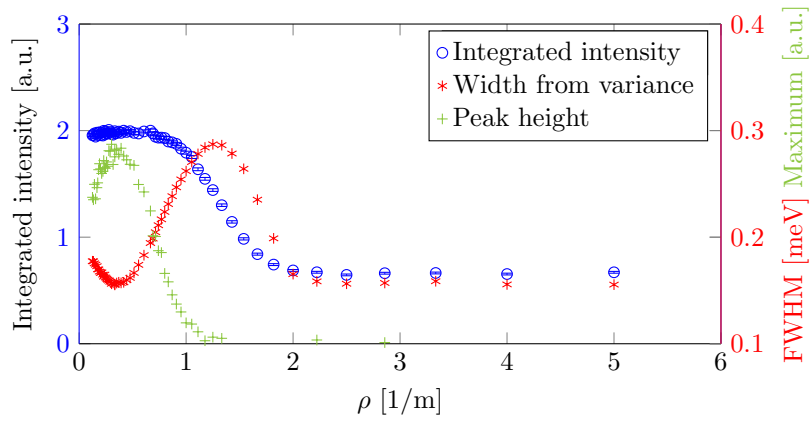


Figure 45: A range of simulations of the type in figure 17 that shows the effect of changing the curvature for the curved 4.5 meV energy channel. Peak intensity (green plus) normalised to the right axis, width (FWHM) (red asterisks), and integrated intensity (blue circles).

B Elastic comparisons between curved and AR

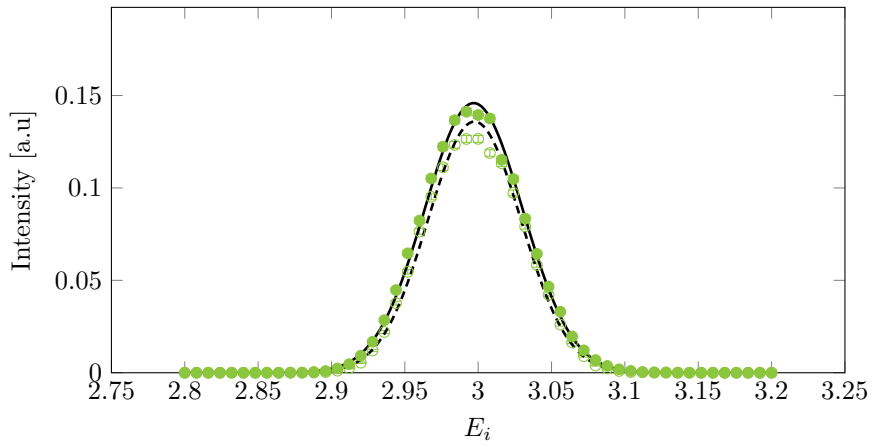


Figure 46: Simulations in the elastic setting comparing the curved (filled circles, solid lines) with the AR (open circles, dashed lines) for $E_i = 3.0$ meV

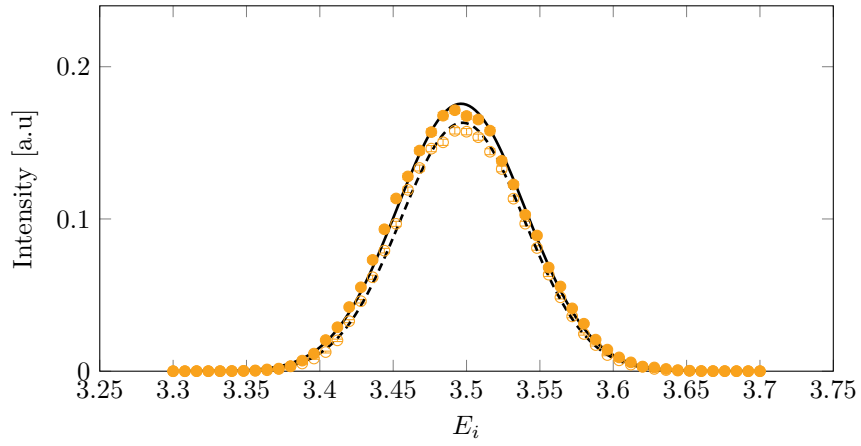


Figure 47: Simulations in the elastic setting comparing the curved (filled circles, solid lines) with the AR (open circles, dashed lines) for $E_i = 3.5$ meV

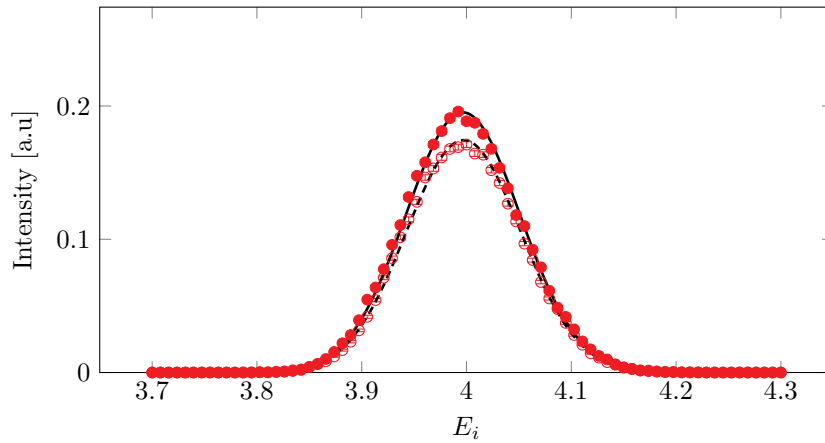


Figure 48: Simulations in the elastic setting comparing the curved (filled circles, solid lines) with the AR (open circles, dashed lines) for $E_i = 4.0$ meV

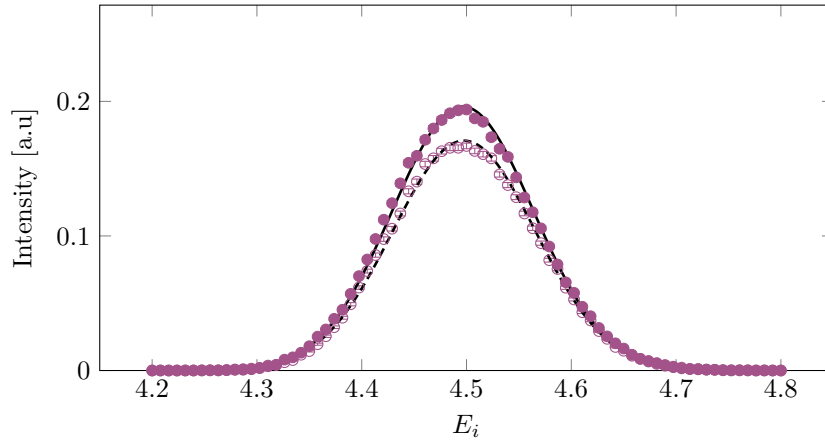


Figure 49: Simulations in the elastic setting comparing the curved (filled circles, solid lines) with the AR (open circles, dashed lines) for $E_i = 4.5$ meV

C Inelastic scans over curvature

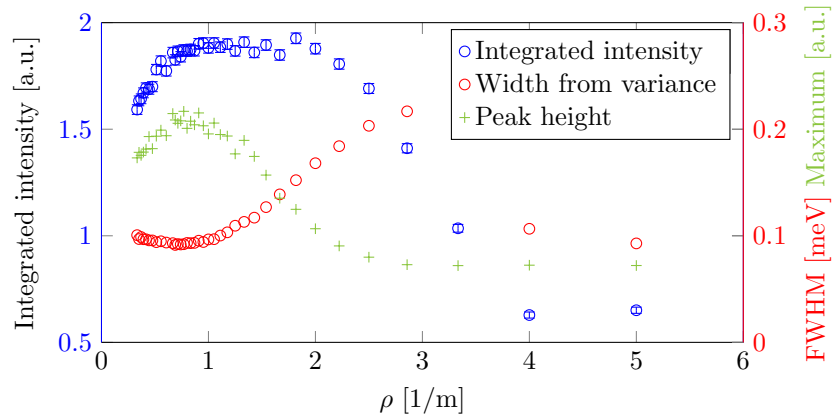


Figure 50: A range of simulations of the type in figure 20 that shows the effect of changing the curvature for the curved 2.5 meV energy channel in the inelastic setting. Peak intensity (green plus) normalised to the right axis, width (FWHM) (red asterisks), and integrated intensity (blue circles).

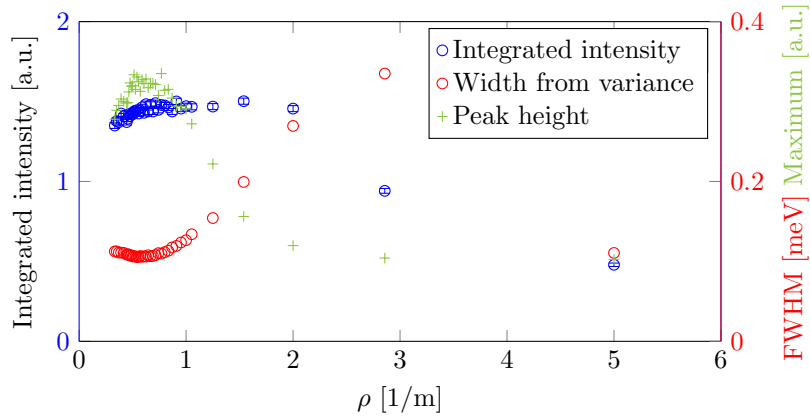


Figure 51: A range of simulations of the type in figure 20 that shows the effect of changing the curvature for the curved 3.0 meV energy channel in the inelastic setting. Peak intensity (green plus) normalised to the right axis, width (FWHM) (red asterisks), and integrated intensity (blue circles).

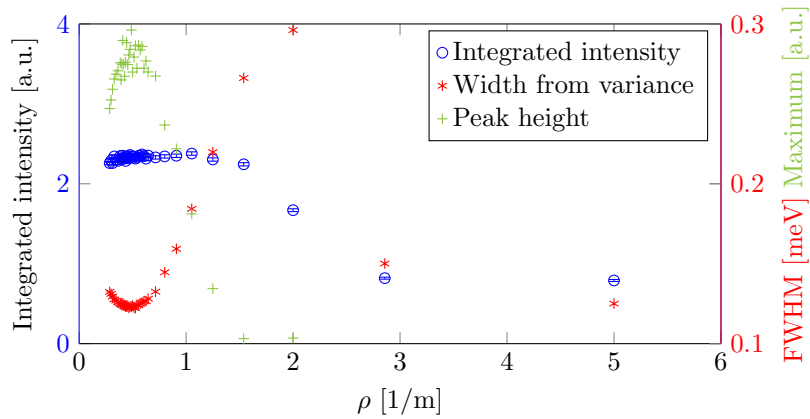


Figure 52: A range of simulations of the type in figure 20 that shows the effect of changing the curvature for the curved 3.5 meV energy channel in the inelastic setting. Peak intensity (green plus) normalised to the right axis, width (FWHM) (red asterisks), and integrated intensity (blue circles).

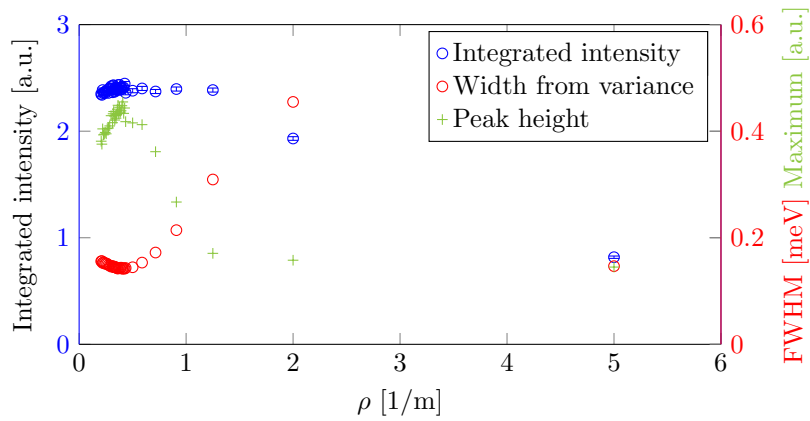


Figure 53: A range of simulations of the type in figure 20 that shows the effect of changing the curvature for the curved 4.0 meV energy channel in the inelastic setting. Peak intensity (green plus) normalised to the right axis, width (FWHM) (red asterisks), and integrated intensity (blue circles).

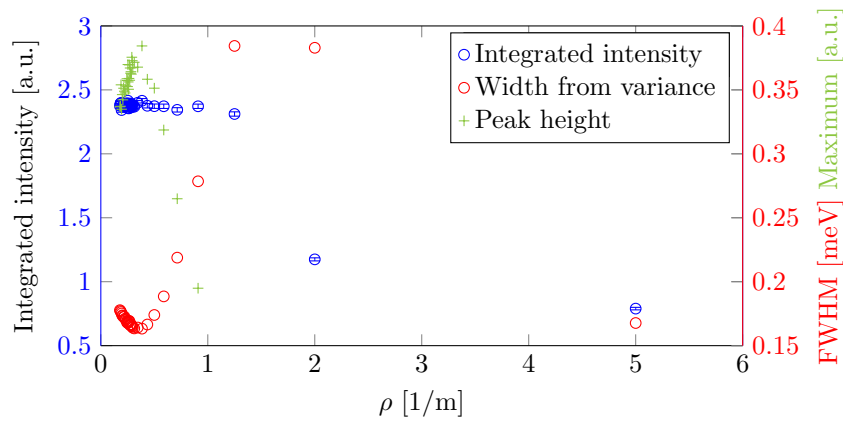


Figure 54: A range of simulations of the type in figure 20 that shows the effect of changing the curvature for the curved 4.5 meV energy channel in the inelastic setting. Peak intensity (green plus) normalised to the right axis, width (FWHM) (red asterisks), and integrated intensity (blue circles).

D Inelastic comparisons between curved and AR

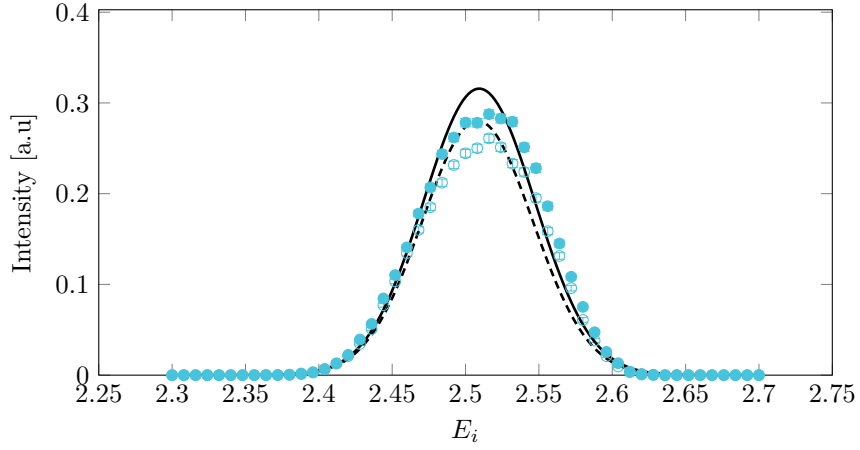


Figure 55: Simulations in the elastic setting comparing the curved (filled circles, solid lines) with the AR (open circles, dashed lines) for $E_i = 2.5$ meV

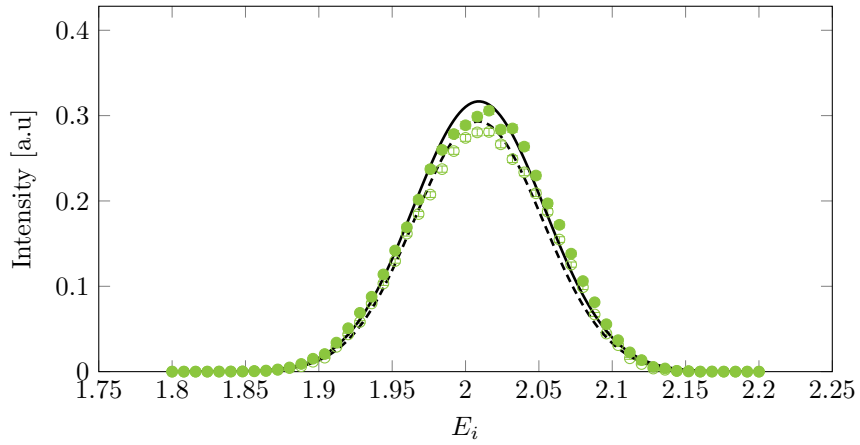


Figure 56: Simulations in the elastic setting comparing the curved (filled circles, solid lines) with the AR (open circles, dashed lines) for $E_i = 3.0$ meV

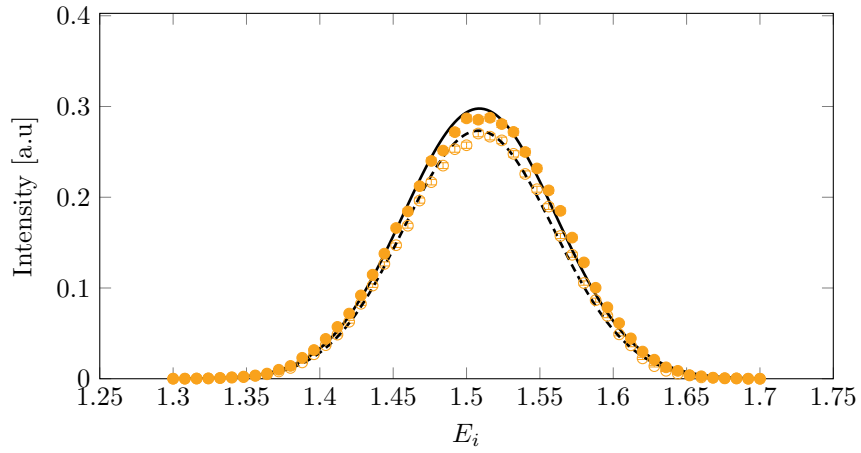


Figure 57: Simulations in the elastic setting comparing the curved (filled circles, solid lines) with the AR (open circles, dashed lines) for $E_i = 3.5$ meV

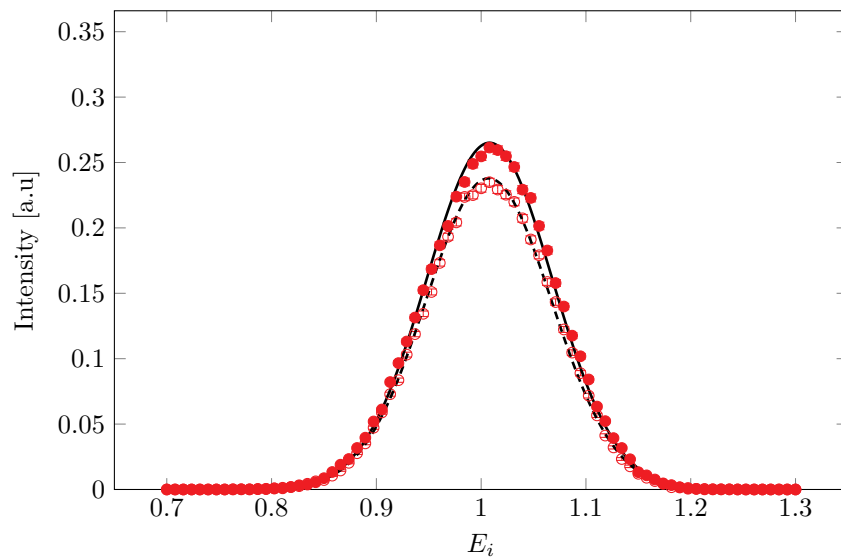


Figure 58: Simulations in the elastic setting comparing the curved (filled circles, solid lines) with the AR (open circles, dashed lines) for $E_i = 4.0$ meV

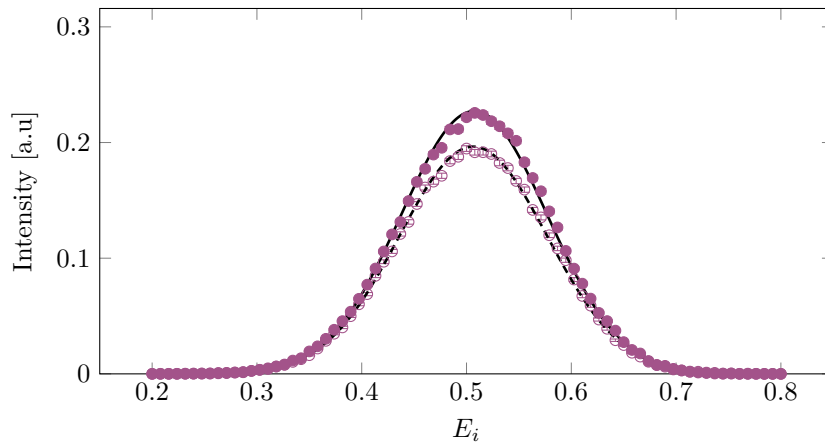


Figure 59: Simulations in the elastic setting comparing the curved (filled circles, solid lines) with the AR (open circles, dashed lines) for $E_i = 4.5$ meV